Title
Development of a Compact Neutron Generator to be Used For Associated Particle Imaging Utilizing a RF-Driven Ion Source

Author
Wu, Ying

Publication Date
2009

Peer reviewed|Thesis/dissertation

Development of a Compact Neutron Generator to be Used For Associated Particle Imaging Utilizing a RF-Driven Ion Source

by

Ying Wu

A dissertation submitted in partial satisfaction of the

requirements for the degree of

Doctor of Philosophy

in

Engineering-Nuclear Engineering

in the

Graduate Division

of the

University of California, Berkeley

Committee in charge:

Professor Ka-Ngo Leung, Chair
Professor Edward Morse
Professor Michael Lieberman
Dr. Qing Ji

Fall 2009

The dissertation of Ying Wu, titled Development of a Compact Neutron Generator to be Used For Associated Particle Imaging Utilizing a RF-Driven Ion Source is approved:

Chair Date

Date

Date

Date

University of California, Berkeley

Development of a Compact Neutron Generator to be Used For Associated Particle Imaging Utilizing a RF-Driven Ion Source

by

Ying Wu

Abstract

Development of a Compact Neutron Generator to be Used For Associated Particle Imaging Utilizing a RF-Driven Ion Source

by

Ying Wu

Doctor of Philosophy in Nuclear Engineering

University of California, Berkeley

Professor Ka-Ngo Leung, Chair

Ion source development plays an important role for improving and advancing the neutron generator technology used for active interrogation techniques employed by the Department of Homeland Security. Active neutron interrogation using compact neutron generators has been around since the late 1950's for use in oil well logging. However, since the September 11th, 2001 terrorists attack, much attention has been paid to the field of active neutron interrogation for detecting hidden explosives and special nuclear materials (SNM) in cargo and luggage containers through the development of effective and efficient radioactive sources and detectors. In particular, the Associated Particle Imaging (API) method for detecting and imaging explosives is of great interest New compact neutron generators will help to enhance the capabilities of existing threat detection systems and promote the development of cutting-edge detection technologies.

The work performed in this thesis includes the testing of various ion source configurations and the development and characterization of an inductively coupled radio frequency (RF) ion source for use in compact neutron generators. These ion source designs have been investigated for the purpose of D-T neutron generation for explosive detection via the Associated Particle Imaging (API) technique. API makes use of the 3.5 MeV alpha particles that are produced simultaneously with the 14 MeV neutrons in the deuterium-tritium ($^2D(^3T, n)^4\alpha$) fusion reaction to determine the direction of the neutrons and to reduce background noise. The Associated Particle Imaging neutron generator required a beam spot of 1-mm or less in diameter at the target in order to achieve the necessary spatial image resolution. For portable neutron generators used in API, the ion source and target cannot be water-cooled and the power deposited on the target must be low. By increasing the atomic ion fraction, the ion beam can be used more efficiently to generate neutrons, resulting in a lower beam power requirement and an increased lifetime of the alpha detector inside the acceleration column. Various source configurations, antenna design, and permanent magnet placement

have been investigated so as to develop an ion source which could provide high monatomic deuterium species and high current density at relatively low RF powers (less than 200 W).

In this work, an RF ion source was developed that uses an external, planar, spiral antenna at 13.56 MHz with a quartz source body and side multi-cusp magnets to generate hydrogen isotope plasmas with high mono-atomic ion species ($> 80\%$) while consuming only 150 watts of power and operating under 10 mTorr of gas pressure. A single acceleration gap with a secondary electron suppression electrode are used in the tube. Experimental measurements of the ion source plasma parameters including ion current density, atomic ion fraction, ignition and operating pressures, electron temperature, and electron density are presented along with a discussion on the ion optics and engineering challenges. It is shown that the measured neutron yield for the developed D-D neutron generator was 2 x 10^5 n/s, which scales to 8 x 10^7 n/s for D-T operation. In addition, initial measurements of the neutron generator performance including the beam spot size, associated particle detection, and neutron tube (without pumping) operation will be discussed. Some suggestions for future improvement are also presented in this dissertation.

Acknowledgements

First and foremost I would like to thank Professor Ka-Ngo Leung for giving me the opportunity to come to UC Berkeley and conduct research in the Plasma and Ion Source Technology Group at LBNL. It was a great learning experience for me and I am thankful for all of his advice throughout the years. I want to thank Professor Edward Morse and Professor Michael Lieberman for being on my dissertation committee and sharing their guidance, advice, and knowledge in the classroom. I also want to express my gratitude to Dr. David Ruzic at the University of Illinois who gave me an opportunity to work in his research lab and sparked my interest in plasma and ion sources.

I will always be grateful to the the members of the Ion Beam Technology Group: Dr. Qing Ji, Dr. Joe Kwan, Dr. Bernhard Ludewigt, Dr. Thomas Schenkel, Stephen Wilde, Thomas McVeigh, Paul Wong, Mark Regis, and Will Waldron for their technical and scientific assistance, without which this work would not have been possible. I would also like to express my appreciation for my fellow colleagues who not only assisted me on experiments but also enhanced my knowledge through fruitful discussions including Dr. Ximan Jiang, Dr. Lili Ji, Dr. Michael King, Dr. Arun Persaud, and Amy Sy.

I would like to thank the faculty, staff, and my fellow students of the Department of Nuclear Engineering at UC Berkeley, especially Lisa Zemelman for always having the right answers to my questions.

A special thanks goes out to John P. Hurley, who was responsible for the funding of the project, and for him sharing his vast knowledge of active neutron interrogation with me.

I would like to thank all of my friends, especially my best friend Andrea Kritcher. She has been an amazing influence and blessing to me and is always there for me. There are no words to describe how thankful I am for her friendship.

Finally I am forever thankful for my family, especially my parents and grandparents as they have stood by me through all my endeavors and have always been there to show their love and support for me.

To my entire family, for their infinite love, support, and encouragement.

Contents

List of Figures **v**

List of Figures **v**

1 Introduction **1**
1.1 Explosives and Nuclear Material Detection 1
1.2 Fast Neutron Interrogation Techniques For Explosives 4
1.3 Associated Particle Imaging 6
1.4 Compact Neutron Generators 8
1.5 Thesis Outline 9

2 Ion Source Development For Compact Neutron Generators **15**
2.1 Background of Ion Source Development 15
2.2 Requirements of the API Ion Source 21
2.3 Ion source configurations and experimental setup 23
2.4 Effects of Different Frequencies on the Ion Source 43
2.5 Conclusion 50

3 Ion Extraction and Target Design **53**
3.1 Ion Extraction Fundamentals 53
3.2 Ion Optics for API Neutron Generator 57
3.3 Beam Spot Measurement 63
3.4 Conclusion 74

4 Sealed Neutron Generator Design and Results **79**
4.1 Prototype Sealed Neutron Generator for API 79
4.2 Neutron Generator Set-up 81
4.3 Associated Particle Measurements 85
4.4 Neutron yield measurements 95
4.5 Conclusion 102

5 Conclusion **103**
5.1 Conclusions and Suggestions for Future Work 103

Bibliography **105**

List of Figures

1.1 Photograph of the Science Applications International Corporation's (SAIC) Vehicle And Cargo Inspection System (VACIS) portal system [4]. 3
1.2 Ratios of the elements H, C, N and O, for a selection of explosives, illegal drugs, and miscellaneous everyday materials [6]. 5
1.3 A spectrum of the measured gamma rays from inelastic scattering collisions of neutrons with different atoms in an object. Here, the oxygen and carbon peaks can be seen [7]. 11
1.4 Schematic of Associated Particle Imaging showing the neutron generator with the projected trajectories of the neutrons and alpha particles which are used to image the interrogated object [2]. 12
1.5 A picture showing how the neutron trajectories are predicted from the position sensitive alpha detector. The trajectories are predicted to go through the center of the beam spot at the target, which fits well for a small beam spot, but worsens as the beam spot size increases. 13
1.6 Schematic of a generic neutron generator developed at LBNL utilizing a RF driven ion source. This neutron generator is not meant to be sealed [19]. . . 14

2.1 First ionization energies of different elements [21]. 16
2.2 Diagram of an inductively coupled plasma using a planar antenna. The varying magnetic and electric fields can be seen. 17
2.3 Diagram of an inductively coupled plasma using a solenoidal antenna. The plasma chamber usually has a high aspect ratio compared to the planar source. 18
2.4 Schematic of the matching network used that uses a ferrite transformer to drive a series resonant circuit in the secondary that includes the antenna. The 50 Ohm output impedance of the RF power supply is matched to the antenna by adjusting the transformer turn ratio and adjusting the capacitor. 19
2.5 Photograph of the matching network with the back panel removed. The ferrite transformer, tuning capacitor, and the inductor L_1 can be seen. 20

2.6 A comparison between the RF ion source to be used in the new RF-driven API neutron generator and the Penning ion source used in commercially available neutron generators. The requirements for the ion beam current and energy are less for the RF source as compared to the Penning source due to the greatly increased atomic ion fraction in the plasma. 21
2.7 The basic plasma source and extraction set-up for testing of various ion source parameters. 24
2.8 Operating pressure vs. power for different sized plasma chambers, the operating pressure drops as the plasma chamber size is increased due to a higher mean free path of the electrons. 25
2.9 The different antenna configurations and their effects on the extracted ion current can be seen here. The biggest jump in ion current was when multi-cusp magnets were used, thus increasing the electron confinement. 27
2.10 The different antenna configuration effects on the operating pressure as a function of power. As the power was increased, the operating pressure is lowered, and the magnetic confinement also helped in lowering the operating pressure as less electrons are lost to the walls. 28
2.11 Ion current extracted vs. operating pressure for the plasma when it is capacitively coupled and inductively coupled. The inductively coupled plasma is more efficient as it produces better ionization rates at lower pressures. 29
2.12 RF current in the antenna as a function of pressure for different powers for when the plasma is on. As the pressure decreases, the current increases for all powers. 30
2.13 RF current in the antenna as a function of power for when the plasma is on and off. For both cases, increasing the power increases the RF current, but the current drops dramatically when the plasma is lit and in the inductively coupled mode. 31
2.14 A plot of the different ion species in the plasma vs. pressure. It can be seen that an increase in the pressure causes a decrease in the atomic ion fraction and an increase in the tri-atomic species. 32
2.15 A plot of the different ion species in the plasma vs. RF power. The atomic ion fraction increases with increasing RF power. 33
2.16 Magnetic field strength contours in a 20 magnet cusp field. The field free region here covers about 50% of the plasma in the center. 35
2.17 Pandira simulation of a 14 magnet cusp field showing the magnetic cusp lines . 36
2.18 Schematic of the quartz body ion source with a 4-turn planar 1/8 inch diameter copper tubing antenna with 20 Nd-B-Fe multi-cusp magnets. 37

2.19 A photograph of the ion source as it sits on the test stand during operation at a power of 150 watts and a source pressure of 12 mTorr of hydrogen gas, and the aluminum plate is positively biased up to 12 kV during current density and mass spectrometry measurements. The cusp field lines formed by the magnets can be easily seen. 37
2.20 A photograph of the ion source as it sits on the test stand, the major components can be seen, such as the copper antenna, cusp magnets, and the quartz ion source. 38
2.21 The current density of the quartz body ion source scales linearly with the input RF power, as expected. The pressure was kept constant at 12.5 mTorr and the RF frequency used was 13.56 MHz. For all powers, the plasma was sustained in the inductively coupled mode. 40
2.22 Comparison of the atomic hydrogen ion species in which the ion source wall material is made from quartz , alumina (Al_2O_3), and aluminum. Previous studies have shown that atomic ion production in hydrogen plasma sources have favored walls made from an insulating material over metal walls. However, the quartz source exceeded all expectations for its atomic ion production as over 85% of the total hydrogen ions were atomic, even at powers as low as 100 watts. 41
2.23 Mass spectrum of the hydrogen plasma at 100 watts of RF power and 12.5 mTorr of gas pressure. The RF frequency was 13.56 MHz. The first peak is the H^+ peak, followed by the H_2^+, H_3^+, and impurities (mostly water) peaks. The fraction of atomic hydrogen ions to other hydrogen ions is 86%. The current density extracted from this plasma was roughly 2.5 mA/cm^2 42
2.24 Some operating conditions of the 27.12 MHz and 13.56 MHz ion source at 100 watts. 43
2.25 A plot of the atomic ion fraction vs. power for hydrogen and deuterium at both 13.56 and 27.12 MHz. It can be seen that the 13.56 MHz RF produces 10-15% higher atomic fraction than 27.12 MHz at low powers, but at higher powers the difference becomes roughly 5%. The difference in atomic fraction between hydrogen and deuterium also decreases from about 7% at 100 watts to 3% at 300 watts. 44
2.26 The electron temperature as a function of input RF power for deuterium and hydrogen. The electron temperature decreases with increasing pressure and is fairly constant with increasing power. The difference in electron temperature between deuterium and hydrogen is negligible. 45
2.27 The electron density as a function of input RF power for deuterium and hydrogen. It can be seen that the electron density increases with both the power and pressure. 46

2.28 Mass spectrum of the deuterium plasma at 100 watts of RF power and 8.5 mTorr of gas pressure. The RF frequency was 13.56 MHz. The first peak is the D^+ peak, followed by the D_2^+ and D_3^+ peaks. 47
2.29 A table of the different reactions which produces the different hydrogen and deuterium ion species [44]. 48
2.30 A mass spectrum of a 50/50 hydrogen-deuterium mix plasma at a pressure of 12.5 mT and 100 watts of input rf power. The plasma is dominated by mass 1 and 2, which are the atomic ion species of hydrogen and deuterium. The other 7 possible species account for approximately 10% of the total ions. . . 49
2.31 A plot of the different deuterium and impurity ion species percentage present in the plasma as a function of power. The impurities species in the plasma were mostly comprised of masses 16-18, namely oxygen, water, and D-O molecular ions. In a fully sealed and clean chamber, there should be no water present and the atomic ion fraction of deuterium should increase by about 8%. . . . 50
2.32 A plot of the atomic deuterium ion fraction in the plasma (including impurities) for 13.56 and 27.12 MHz RF as a function of power. It can be seen that as power is increased, the 27.12 MHz ion source increases its atomic ion fraction at a greater rate than the 13.56 MHz source, but due to its poor performance at lower powers, 13.56 MHz was chosen as the operating frequency. 51

3.1 a) Example of an under-dense plasma and ion extraction simulation in IGUN, the meniscus can be seen bowed inward. b) Example of an over-dense plasma and ion extraction simulation in IGUN, the meniscus can be seen bowed outward. c) Example of a well matched plasma density and ion extraction simulation in IGUN, the meniscus is fairly flat and the resultant beam is relatively parallel. 55
3.2 The different emittance ellipse orientations for converging, diverging, parallel, and focused ion beams. 56
3.3 IGUN simulation of the hydrogen ion beam trajectories. The simulation was done assuming a 60 kV bias on the plasma electrode, a -500 volt on the shroud/electron suppression electrode, and the target at ground. The extraction aperture opening was 0.8-mm in diameter and the current that reached the target was 36 μA. The target is at a distance 12 cm away from the extraction aperture. 58
3.4 IGUN simulation of the beam profile at the Ti target 12-cm away from the extraction aperture. The profile was obtained with the same conditions in the ion beam trajectory simulation. The overall ion beam diameter at the target is around 1.2-mm. 59

3.5 An enhanced look at the plasma meniscus for the API neutron generator shows that the meniscus is flat near the extraction aperture. This also shows the beam being focused as it travels down towards the target. 60
3.6 Up close photograph of the electron suppression electrode and target outside of the neutron generator chamber body. The end of the target can be seen sticking out, the beam facing side is inside the electron suppression electrode. The insulator is an inch thick PVC with grooves machined in. 61
3.7 A photograph of the electron suppression electron as it sits in the neutron generator body. The view of the electrode is from the front flange opening where the ion source is attached. 62
3.8 Photograph of the Zener diodes. Each diode is capable of providing 200 volts and can dissipate 10 W of power. A 200 MΩ resistor is connected to ground to ensure there is always current flowing through the diodes. 64
3.9 Circuit diagram of the biasing of the shroud electrode and target. The Zener diodes provides a 1400 volt drop between the shroud and the target. The 200 MΩ resistor ensures that there is always some current flowing whether or not there is an ion beam hitting the target. 65
3.10 Photograph of the electron suppression electrode with the slit cut out to expose the target. A camera was placed just outside the vacuum window to take photographs of the beam spot on the target. A charged particle detector was placed on that same flange in subsequent experiments to measure the associated particles from the D-D reaction. 66
3.11 Photographs of the the beam spot size decreasing as the acceleration voltage is increased. As the voltage increases the beam spot becomes smaller due to better matching of the electric field to the plasma meniscus and the beam becomes more parallel. 67
3.12 A 3-D reconstruction of the beam profile from the photograph of the beam spot taken using the extraction electrode with no ion collimation channel at 60 kV and 120 W of RF power. 68
3.13 The reconstructed 2-D profile of the beam spot at 60 kV using an extraction electrode with an 1-mm diameter extraction aperture with a very small thickness. 69
3.14 A plot of the experimental ion spot size as a function of extraction voltage for a constant source pressure of 12 mTorr of hydrogen and a RF power of 120 W. The major and minor axis are shown because the beam spot is elliptical in shape due to the target being at 45 degrees with respect to the ion beam. 70
3.15 Examples of the different extraction electrodes that were machined and tested with varying channel depths. The extraction diameter remained constant at 1-mm for all cases, while the channel depth varied between 0 to 8 mm (8-mm channel not shown in figure). 72

3.16 Diagram of the extraction electrode shape. The electrode is made from aluminum, and the plasma facing side is flat and smooth with a 1-mm hole drilled through, this diameter is labeled as a. The ion collimation/extraction channel length d can be varied, but the angle of the extraction opening remains constant at 67.5 degrees, the Pierce angle 73
3.17 The photographs of the silicon dies after they have been sputtered by the hydrogen beam, a small spot can be seen where the beam was incident on the silicon. 74
3.18 The inverted profile from the ASIQ profilometer scan of the silicon die sputtered using the 4-mm deep channel extraction aperture. The profile is roughly 0.5 mm in diameter. 75
3.19 The inverted profile from the ASIQ profilometer scan of the silicon die sputtered using the very thin "0-mm" thick channel extraction aperture. The profile is roughly 2 mm in diameter. 76
3.20 The photographs of the silicon dies after they have been sputtered by the hydrogen beam, a small spot can be seen where the beam was incident on the silicon. 77

4.1 Engineering drawing of the API neutron generator. The plasma is produced by a planar RF-driven antenna at 13.56 MHz and the ion beam is extracted from the plasma electrode at ground potential and accelerated through the shroud electrode biased at -80 kV and to a titanium target biased at -78 kV. There is a hole on the side of the shroud electrode for the alpha particles to pass through and reach the alpha detector, and the blue cone opposite the alpha detector is the region of space which can be used for neutron scanning and imaging. 80
4.2 Schematic of the prototype neutron generator. The generator is attached to a pumping unit and vacuum chamber. For sealed mode operation, a valve is used to block the vacuum and the needle valve turned down to stop the gas inlet. 82
4.3 Photograph of the prototype neutron generator with the ion source running. The high voltage is attached at the via a couple of anti-corona donuts and spheres. The alpha detector and ion gauge can also be seen in the picture. . 83
4.4 A photograph of the target up close, the beam spot is the white colored spot on the target in the photograph, some darkened circles can be seen around it from the heat being dissipated on the target. 84
4.5 Electron current measured as a function of electric field between the shroud electrode and chamber wall, the distance between the two concentric cylinders is 8 cm and the applied voltage on the shroud is adjusted between 0 to 80 kV. 86

4.6 Schematic of the scintillator and photo-multiplier tube set up in the neutron generator. 87
4.7 Photograph of the gold and aluminum coated scintillators used for alpha particle detection after a spark in the main chamber during sealed operation. . . 88
4.8 Photograph of the backside of the aluminum coated scintillator and a non-metal coated scintillator showing the discoloration of the plastic due to the electrical breakdown. 89
4.9 A photograph of the charged particle detector. 91
4.10 CASINO simulation of 50 keV electron distribution in aluminum, the different colors lines reflect the percent of electrons that are outside the lines. 92
4.11 CASINO simulation of 70 keV electron distribution in aluminum, the different colors lines reflect the percent of electrons that are outside the lines 92
4.12 A photograph of the charged particle detector with a thin foil in front of it. . 93
4.13 A plot of the spectrum collected on the multi-channel analyzer from the charged particle detector. 94
4.14 The fusion cross sections of D-T, and D-D reactions as a function of energy on a log-log plot. The energies of interest is highlighted on the plot [58]. . . . 97
4.15 The predicted D-D neutron yield curve as a function of ion energy for an ion current of 25 μA, this also assumes that the target is loaded at a hydrogen to titanium ratio of 2:1 and that all of the ions are atomic. 98
4.16 The drawing of the neutron and x-ray shielding for the API neutron generator. A gamma detector was mounted outside the high voltage cage to monitor the x-ray dose and a He-3 neutron detector embedded in a sphere of polyethylene was used to monitor the neutron dose [59]. 99
4.17 A comparison of the relative neutron yield between titanium and molybdenum targets. It takes about 3 to 4 hours to fully load the target, and the molybdenum target can reach about 45% of the neutron yield of the titanium target. 100
4.18 The target loading times for molybdenum after waiting 24 hours after the targets has been loaded. It takes about 15 minutes to reach 85% of the neutron yield of the previous day, and about an hour to be fully loaded. The same trend was also observed for titanium. 101
4.19 The theoretical and measured neutron yield of the API neutron generator for D-D operation and the theoretical and predicted neutron yield of the API neutron generator for D-T operation. 102

Chapter 1

Introduction

The ability to determine the elemental composition of materials in an unidentified object, such as hidden explosives and contraband, is an essential mission in the non-proliferation and homeland security of this country. Since the 1983 bombing of the U.S. Embassy in Beirut, suicide bombings have killed more than 21,000 people and injured 50,000. More than four-fifths of the suicide bombings have occurred in the past eight years. Since September 11th, 2001, there has been a large number of suicide bombing attacks in dozens of countries spread over five continents [1]. Many of these attacks have taken place in Iraq and Afghanistan, countries which the U.S. has significant numbers of soldiers present. Although there has not been a major bombing in the U.S., there is always the threat of someone transporting an explosive onto a vehicle and driving it into a populated area. The Department of Homeland Security has put much work into deterring these attacks, and the development of explosive detection systems based on active neutron interrogation techniques to deter these attacks have been a major part of the deterrence plans.

1.1 Explosives and Nuclear Material Detection

The current technique for inspection at the ports, borders, and other sensitive locations in the U.S. are passive portal monitors. However, these systems are limited to the detection of only those hazardous radioactive materials that emit detectable radiation. Because of this issue, hazardous materials that are not radioactive, including all conventional explosives will be able to pass through the portals with ease. Thus, it is very important to develop techniques which can quickly detect, image, and identify any explosives and contraband which do not emit any ionizing radiation [2]. Associated Particle Imaging (API), a specific type of active neutron interrogation which is designed for inspection of small vehicles and similar sized crates meets those requirements by providing detection, imaging, and identification of hidden explosives. A summary of the current detection systems, as well as API are given in the

following sections.

1.1.1 Passive Detection Systems

Gamma and neutron scintillator detectors have been built into radiation portal monitors at ports all around the United States. These detection systems do not have an active source of radiation to probe the cargo for inspection, instead they simply rely on the gamma and neutron counts on the detector to look for special nuclear material that might be smuggled on cargo containers. The first generation of these systems were installed in 2002, and the systems were only sensitive to the radiation intensity, not the energy. This caused a large number of false alarms due to trace amounts of K-40 in bananas and other common items with small amounts of radioisotopes. Because of this shortcoming, a second generation of radiation portals was installed in 2006 with the ability to measure radiation energy spectra. The new portals can compare the scanned spectra to a library of known spectra, and reduce the number of false alarms in inspection [3]. However, even though this system is reliable for detecting unshielded special nuclear materials, it is ineffective for detecting shielded materials, or conventional explosives with no radioactive isotopes present. Therefore, in light of these shortcomings, a new generation of detection systems which utilize accelerator-based neutron and gamma sources for active interrogation is being developed. These systems show great potential for the ability to detect shielded special nuclear materials and conventional explosives and drugs in cargo containers.

1.1.2 Detection Systems Based on Isotope Sources

Detection systems utilizing gamma rays from radioactive sources have been used for years at ports for inspection of cargo containers for stolen vehicles and drugs. These systems use Co-60 and Cs-137 to produce gamma rays to scan for high density material in the containers. These materials are of interest because nuclear materials and shielding materials, such as lead, are very dense [4]. A disadvantage of using radioisotopes as a radiation source for inspection is that the source itself must always be shielded to prevent nearby workers from being irradiated. The source also must be properly secured from being stolen and used in an airborne explosive which could spread radioactive ash all over a city. A photograph of such a portal with a truck passing through can be seen in Fig. 1.1 [4].

1.1.3 Small Scale Conventional Explosives Detection

Despite the threat of a small scale nuclear or dirty bomb attack in recent years, attacks with conventional explosives are still the most prevalent threat, especially in the airline industry [5]. The reason being that nuclear materials are difficult to obtain and handle, while explosive materials such as ammonium nitrate, a common oxidizing agent for explosives, can

Figure 1.1: Photograph of the Science Applications International Corporation's (SAIC) Vehicle And Cargo Inspection System (VACIS) portal system [4].

be obtained easily as it is found in certain kinds of fertilizer. The security check points at airports use x-ray computed tomography machines to reconstruct three-dimensional density images of the luggage. The luggage is scanned from a rotating fan beam of x-rays and each slice of the luggage image is used to reconstruct the final image. This method looks for effective material densities and effective atomic numbers which resemble that of explosives. Unfortunately, there are certain harmless materials which are mistaken for explosives, causing hold ups during scanning.

Vapor and swipe methods are techniques used on luggage which have been deemed to potentially contain explosives. The swipe technique is a simple swipe of the luggage surface with a swab which is then analyzed for trace amounts of chemicals used in explosives. Vapor detection looks for high vapor pressure explosives by placing the suspected luggage in a chamber, and blowing air downwards towards an analysis chamber to look for trace amounts of chemical vapors which might have been pushed down with the air. These methods are usually much more accurate, but also take much more time, making it impossible to screen all luggage this way.

1.1.4 Detection Systems Using Active Interrogation

Active neutron interrogation is defined as the use of an external source of neutrons to induce a stimulated radiation signature from the interrogated object. Active interrogation is good for detecting shielding nuclear materials as the high energy neutrons can penetrate the shielding and induce radiation emission from the material of interest. Explosive detection is also improved by using active neutron interrogation, as X-ray tomography machines cannot resolve differences between two materials that are closely related in average atomic numbers and density. Fast neutron based explosive detection can provide identification of different ratios of nitrogen and oxygen to other elements present to differentiate explosives from regular material.

1.2 Fast Neutron Interrogation Techniques For Explosives

Neutron generators are used in a variety of ways to detect conventional explosives. The main methods are Fast Neutron Analysis (FNA), Pulsed Fast Neutron Transmission Spectroscopy (PFNTS), and Pulsed Fast Neutron Analysis (PFNA). In conventional explosives, the main elements present are nitrogen, oxygen, hydrogen, and carbon. All of these methods involve examining the ratios of nitrogen, carbon, and hydrogen to oxygen present in the inspected object. By comparing explosives to illegal drugs and everyday materials, it can be shown that the material composition of explosives can be differentiated from other materials [6]. Fig. 1.2 shows a stacked bar graph for the fraction of H, C, O, and N in various materials. Fast neutron inspection techniques can determine the elemental ratios and from that the presence of explosive materials can be confirmed. However, this technique requires high neutron penetration into the object and a large array of gamma ray detectors which can provide two or three dimensional imaging of the object.

1.2.1 Fast Neutron Analysis

Fast neutron analysis (FNA) utilizes the (n,n'γ) reaction to produce gamma rays from the interrogated object from inelastic scattering of the neutrons with the nuclei of the elements inside the object. The nuclei are excited to a higher state from the collision with the neutron and release de-excitation gamma rays upon returning to the ground state. Different elements will emit different characteristic gamma rays and their energies and intensities can be measured, as shown in Fig. 1.3 [7]. This method uses a continuous flux of monoenergetic fast neutrons and an array of gamma detectors which are shielded from the neutrons and surround the object.

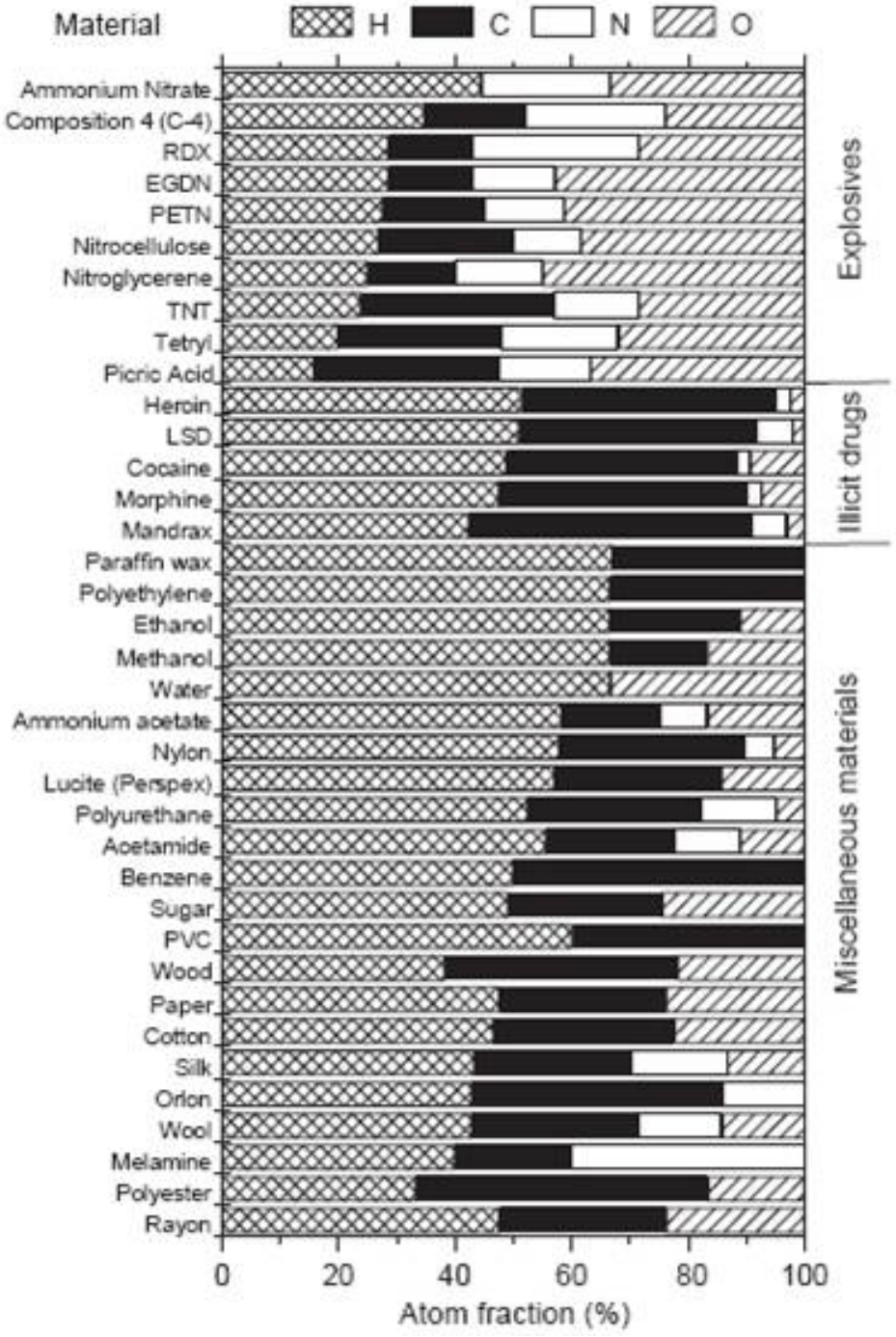

Figure 1.2: Ratios of the elements H, C, N and O, for a selection of explosives, illegal drugs, and miscellaneous everyday materials [6].

1.2.2 Pulsed Fast Neutron Analysis

Pulsed fast neutron analysis (PFNA) also uses the gamma rays produced from inelastic scattering of the interrogating neutrons with the elements inside the object. However, the neutrons are pulsed from the generator with a specific frequency and pulse width. Time of flight measurements of the neutrons which pass through the object are taken by a fast neutron detector. This allows the system to provide a time correlation between the detection of the neutron pulse and the detection of the resultant characteristic gamma-ray which can be used to determine where the neutron inelastic collision occurred. This method also reduces the neutron background [8].

1.2.3 Pulsed Fast Neutron Transmission Spectroscopy

Pulsed Fast Neutron Transmission Spectroscopy (PFNTS) is different from the other methods in that it does not look for the characteristic gamma rays produced in the inelastic neutron scattering events. Instead, it uses plastic scintillators to look at the transmitted neutron intensity and energy to determine the composition of the interrogated object. As neutrons pass through the object, they lose energy and slow down. Each element has a specific neutron attenuation factor, so the resultant spectra can be compared to known neutron attenuation spectra for specific elements to determine the material inside. The difficulty in this method is the neutron generator must be able to produce a range of neutron energies which covers the full range of attenuation cross sections and have a neutron pulse width of around 10 ns to achieve good energy resolution [9].

1.3 Associated Particle Imaging

Associated Particle Imaging, or API is a specific kind of fast neutron analysis which utilizes the D-T fusion reaction and uses the associated alpha particles from the reaction. In contrast to other fast neutron interrogation techniques, API is a self-collimating method where the alpha particles are used to determine the position and direction of the neutrons emitted [10, 11, 12]. Since neutrons are emitted isotropically from the source, the alpha particles limit the background noise by selecting events that are caused by neutrons that are only emitted in the direction of the interrogated object. The tagged neutrons typically make up about 4 to 10% of the total neutrons produced.

The object or cargo is interrogated with 14-MeV neutrons and the neutron interaction sites within the material are imaged via the detection of associated alpha particles. The D-T reaction creates a neutron and an associated alpha particle (see Eqn. 1.2) that travel in opposite directions along the same vector at velocities of 5.2 cm/ns and 1.3 cm/ns, respectively. Therefore, detection of the alpha particle trajectory, using a position sensitive alpha detector, enables determination of the neutron direction [13]. When the neutron interacts with the

unidentified object nuclei via inelastic scattering, the nuclei emit characteristic gamma rays. Detection of these characteristic gamma rays provides determination that reaction events have occurred, and measurement of their energy spectra determines the elemental composition of the probing region. Then, the distance the neutron has traveled within the material can be determined through simultaneous time of flight measurements of the gamma emission and associated alpha particles, via the conservation of linear momentum. The simultaneous detection of gamma rays with accompanied alpha particles aids in the reduction of background noise, where unassociated gamma rays emitted from the surrounding un-interrogated region are disregarded. Thus, this is an effective electronic collimation method, designed to improve the signal to noise ratio. See Fig. 1.4 [2] for a schematic of the API and compact neutron generator geometry.

The beam spot size is a very important aspect for API. The smaller the beam spot, the more accurate the imaging will be. Fig. 1.5 shows the effect of the spot size on the projected image. The projected neutron trajectory for the system goes through the center of the beam spot, and as that spot gets bigger, the accuracy of the trajectory estimation is worsened. Therefore the beam spot must be kept small (around 1-mm or so).

Most neutron generators do not care about the ion beam spot size on the target; in fact, a larger beam spot on target usually means higher neutron yield due to the larger surface area of interaction. Fortunately for API, a high neutron yield is not necessary due to accidental coincidence rates. It is very important to keep the beam power density on the target low because if the target is not properly cooled, then the target will increase in temperature, the implanted deuterium or tritium ions will diffuse out and the neutron yield will drop.

1.3.1 API Neutron Yield Requirements

Typically the output of the generator is higher than API can handle. The reason that the output is limited to under 10^8 n/s is because the technique employs coincidences between the alpha particle and the detected gamma ray and the accidental coincidence rate competes with the true rate when the output gets too high, i.e. approaching 10^8. When the data comprise too many accidental events, the quality of the data is reduced to the point where the imaging quality and, hence, the signal-to-background ratio, is reduced. This, then, frustrates the reason for recording coincidences.

The alpha particle detector used in previous API systems has a sensor consisting of a scintillator, a micro channel plate (MCP), and a thin 1 μm aluminum coating to restrict light and scattered ions from reaching the detector [14]. The MCP is a small device that is a disk comprising many channels, each of which is an electron amplifier. When light hits the front surface of each channel, it generates an electron that is accelerated down its channel because of a voltage difference between the front surface and the collector at the back (output) side of the disk. As the electron hits the side of its channel, it produces more electrons so that at the collector it has a pulse that is large enough to be useful. The device produces 5 pulses

for each event: 1 is for timing, 2 is + X, 3 is for - X, 4 is for + Y and 5 is for - Y. In the electronics provided, the time difference between + X and - X is converted into a signal for the X position while the same process produces a signal for the Y position. The result is the position information for the alpha particle which is then used to define the direction of the neutron and its production time. The MCP is very fast; it operates in the ps range so that it is not the limiting factor for either position or timing. The limiting factor is the coincidence resolving time. This time needs to be at 1 ns or lower, which is difficult to attain. This is important not only because the accidental coincidence rate is determined by the resolving time, but 14 MeV neutrons move at 5.1 cm/ns and the faster the resolving time, the better the Z direction resolution. $LaBr_3$:Ce scintillators are fast enough to achieve this resolving time requirement and also provide very good energy resolution, but they are very expensive.

The main focus of API is on the inspection of small vehicles, as they are a serious source of explosive transport. Checkpoints must be set up in and around structures and people to be protected to inspect the incoming vehicles. The time-on-station (TOS) or inspection time must be around two minutes, which is approximately the same time it takes to run mirrors under vehicles and inspect interiors. Also, the IEEE has come up with some active interrogation standards that allow 2.5 min for small vehicles. This time can be decreased by the number of gamma detectors that are employed. That number is limited only by the available solid angle (as the detectors can be placed almost anywhere), and the cost of the system. This means that whenever the number of detectors is doubled, the counting rate is also doubled.

For small vehicle inspections the distance from the generator to the vehicle is about 3 m. Because the neutron flux scales as the square of the distance as do the gamma rays also (although the neutrons of interest are constrained to be in the cone specified by the alpha particle detector their number density still depends on the solid angle subtended by the vehicle), so the longer the distance between the generator, the vehicle, and the detectors, the longer the inspection time will be. The gamma detection set-up would involve a minimum of two pods, each containing eight $LaBr_3$ detectors. More pods can be used to improve time-on-station problems, but also increase the cost as one pod of eight detectors costs around $500,000 [15].

1.4 Compact Neutron Generators

Neutron generators have long been used in the oil drilling business as a tool for analyzing the geological properties deep in the earth. In the process of oil well logging, methods are applied to search for hydrocarbon zones in geological formations beneath the Earth's crust. An energy source, such as a neutron generator, is lowered into the well as it is being drilled, and neutrons are scattered from the geological formations. Detectors attached to the neutron generators measure the amount of backscattered radiation, providing the material porosity

and permeability. This can help determine the feasibility for the rock to be removed. Also, the detection of gamma ray radiation from naturally occurring shale deposits can indicate the presence of oil and gas.

1.4.1 Compact Neutron Generator Development at LBNL

Compact neutron generators using radio-frequency (RF) driven plasma discharges have been developed at Lawrence Berkeley National Laboratory [16, 17, 18] in the past 10 years. These compact neutron generators are composed of three main parts: the plasma source, the acceleration column, and the target. The source is a deuterium plasma formed by ionizing deuterium gas through RF coupling. The deuterium ions present in the plasma are then extracted from an aperture in the plasma facing electrode and accelerated up to over 100 keV onto a metal target. The target is typically either a pre-loaded metal hydride target, or a plain metal target that can adsorb deuterium and tritium atoms very efficiently and form metal hydrides. The incoming ions can then collide with the implanted deuterium through D-D or D-T fusion reactions and produce neutrons of 2.45 MeV and 14.1 MeV respectively. These neutrons can then be moderated and collimated to the necessary energies and direction by using various shielding materials such as polyethylene and used in the detection of explosives and chemical agents in recovered field munitions. An example of a typical LBNL axial RF-driven neutron generator is shown in Fig. 1.6 [19]. A deuterium plasma is formed in the ion source from RF-induction fields from the copper antenna, and is extracted through a small aperture and accelerated up to energies of 80-100 keV or higher towards a metal target which may be either pre-loaded with tritium or deuterium. Surrounding the target is an electrode which is biased at a slightly more negative potential than the target, thus suppressing secondary electrons formed at the target when the beam of deuterium ions strikes the target. The main fusion reactions that take place are the deuterium-deuterium reaction and the deuterium-tritium reaction, shown by Eqns. 1.1 and 1.2.

$$^2D + {}^2D \rightarrow {}^1n + {}^3He \ (E_n = 2.45MeV, E_{^3He} = 0.82MeV) \tag{1.1}$$

$$^2D + {}^3T \rightarrow {}^1n + {}^4He \ (E_n = 14.1MeV, E_{^4He} = 3.5MeV) \tag{1.2}$$

1.5 Thesis Outline

The goals of this project include the development, improvement, and prototyping of a compact, sealed, RF-driven neutron generator for the use of associated particle imaging for use in the detection of explosives, especially land mines. The aim of this project is to improve the current state of the art neutron generators used for API, mainly to improve the ion source in terms of having high atomic ion fraction, low RF power consumption, high life

time, producing a small 1-mm diameter beam on target, and integrating everything together in a sealed generator design without water cooling. Chapter two addresses the ion source design and the data that was gathered for the development of the ion source. Chapter three includes the design of the acceleration column, target, and shroud electrode for the API neutron generator. Chapter four presents the whole neutron generator system operation, along with neutron yields measured with gold foil activation and the feasibility of associated particle detection under sealed conditions. Finally, chapter five presents the conclusion of the work done and suggestions for future work.

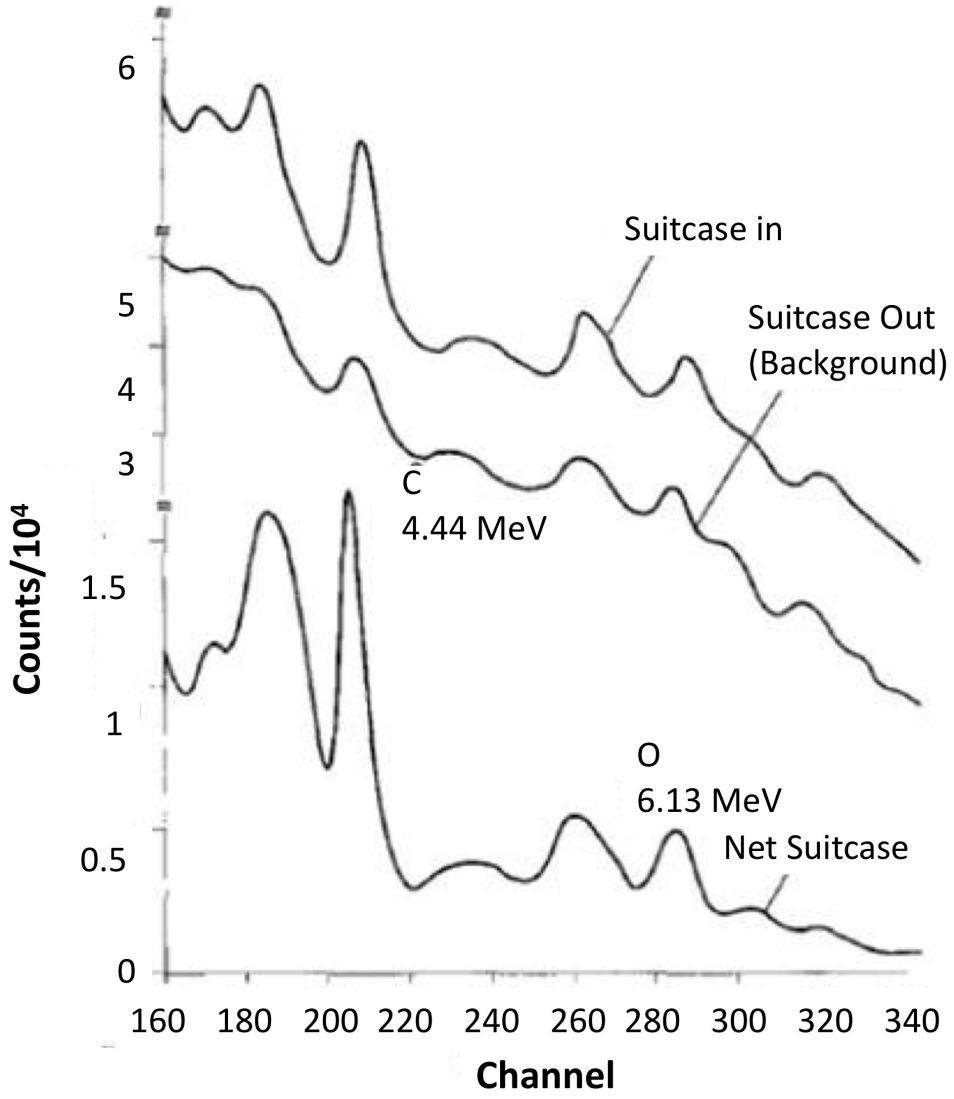

Figure 1.3: A spectrum of the measured gamma rays from inelastic scattering collisions of neutrons with different atoms in an object. Here, the oxygen and carbon peaks can be seen [7].

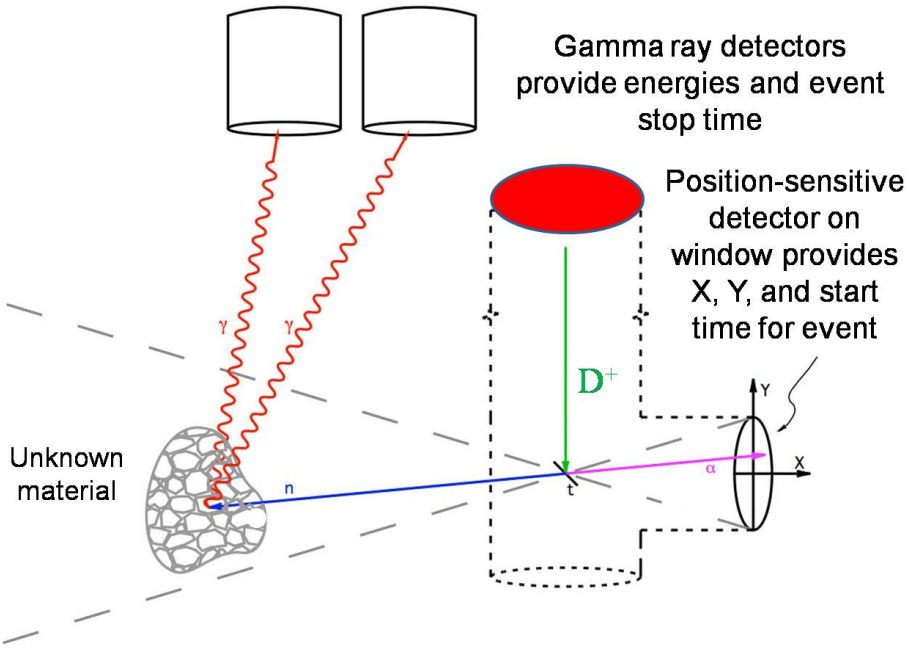

Figure 1.4: Schematic of Associated Particle Imaging showing the neutron generator with the projected trajectories of the neutrons and alpha particles which are used to image the interrogated object [2].

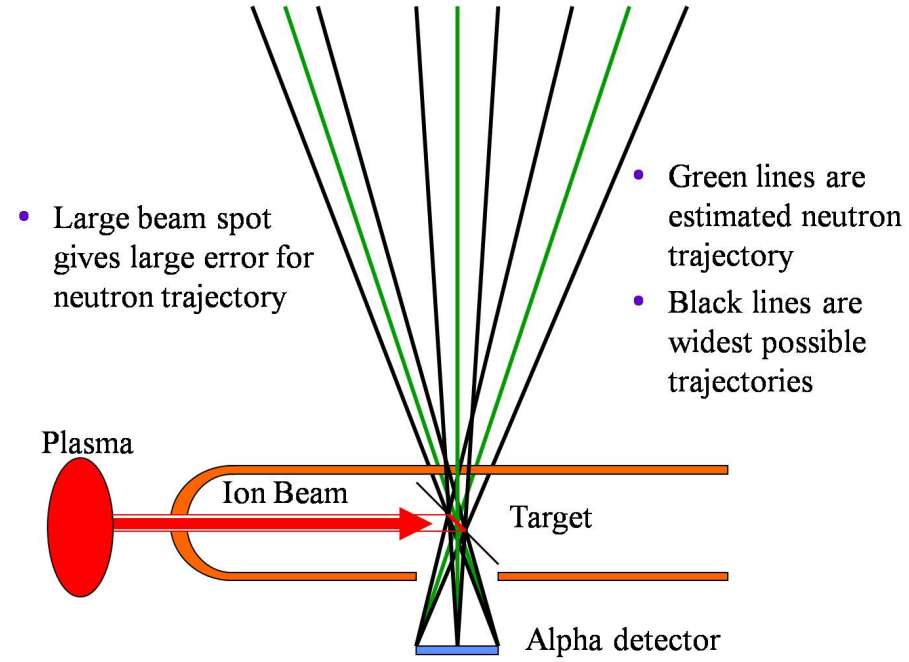

Figure 1.5: A picture showing how the neutron trajectories are predicted from the position sensitive alpha detector. The trajectories are predicted to go through the center of the beam spot at the target, which fits well for a small beam spot, but worsens as the beam spot size increases.

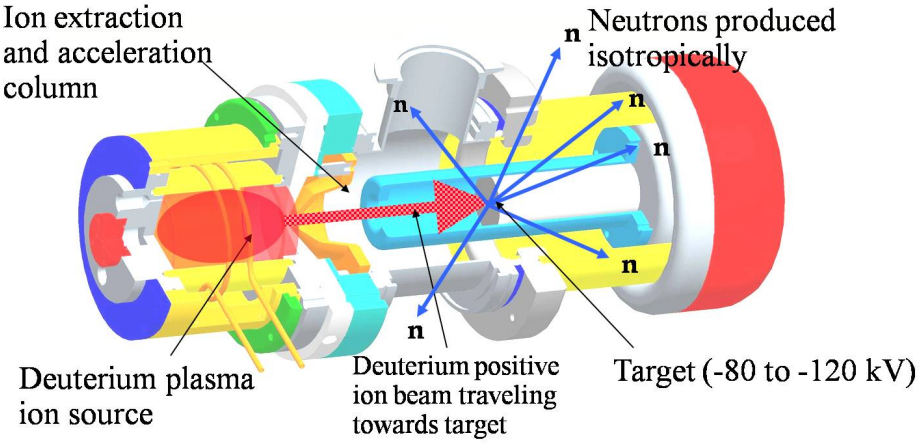

Figure 1.6: Schematic of a generic neutron generator developed at LBNL utilizing a RF driven ion source. This neutron generator is not meant to be sealed [19].

Chapter 2

Ion Source Development For Compact Neutron Generators

2.1 Background of Ion Source Development

Ion source development in the past four decades has led to significant improvements in the field of compact neutron generators, semiconductor manufacturing, and neutral beam diagnostics and heating in fusion devices. In all these applications, the ion source is very often the most important component. Traditionally, ion sources were mainly used in large particle accelerators, often acting as the limiting factor in the beam current and performance of the accelerator. However, due to the increasing number of everyday applications for ion sources, the development of a higher current density ion source was no longer enough. Different methods for positive and negative ion production were developed, as well as ion sources of various sizes, designed to operate in different environments and with appropriate ion species.

An ion source is a device that creates and confines charged particles within a chamber with an aperture or slit, from which the charged particles can then be extracted. In most cases, the ions are produced in a low density plasma, an ionized gas that is composed of both ions and electrons in quasi-neutral equilibrium. Plasma is formed when high energy electrons are created by some methods and collide with the background neutral gas atoms or molecules, i.e. electron impact ionization. After the first few neutral particles are ionized, a cascade of electrons are produced and the resulting cascade creates and sustains the plasma. For different elements, different threshold ionization energies are needed to be overcome by the electron or the ionization particle; this is known as the first ionization energy [20], which is also the binding energy of the electron to the atom. Fig. 2.1 [21] shows a plot of different first ionization energies for different elements.

It can be seen that the first ionization energies of a majority of the elements range between 5 and 25 eV. The probability of ionization is dependent on the electron energy. The ionization cross section for most elements start at zero for electron energies below the

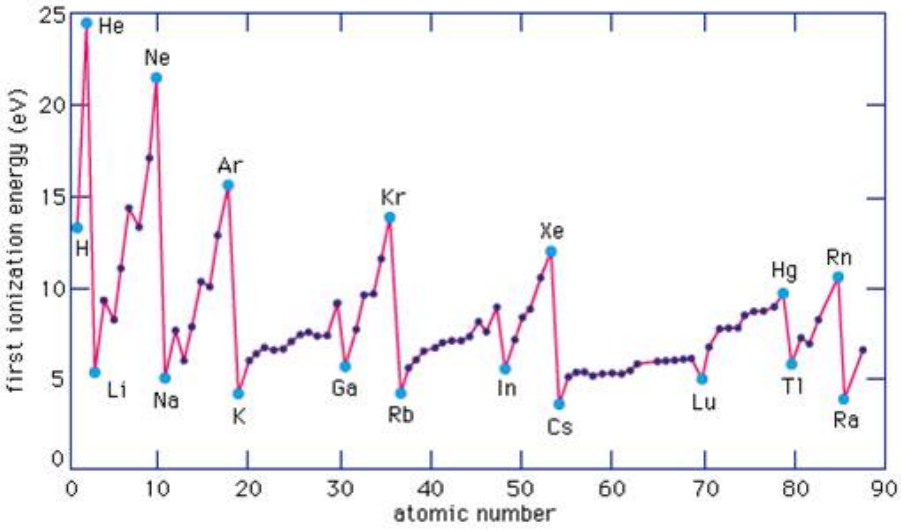

Figure 2.1: First ionization energies of different elements [21].

first ionization energy, and increases to a maximum somewhere between 40 and 100 eV. For hydrogen, the ionization cross section peaks at around 50-60 eV [22]. In most weakly ionized plasmas, the average electron temperature is between 1-10 eV [23]. But due to the Maxwellian distribution of the electrons, there is a high energy tail end which causes most of the ionizations. The work presented here mainly focuses on the method of radio-frequency (RF) ionization to ignite and sustain the plasma discharge.

2.1.1 Radio Frequency Ion Source

The use of radio-frequency electromagnetic fields to energize the cold electrons is a common way of forming the ion source plasma. The RF plasma can be sustained and operated in two distinct regimes: capacitively coupled and inductively coupled. The capacitively coupled plasma is created by a high voltage potential between the antenna and the plasma electrode which oscillates at the RF frequency. This discharge is typically characterized by a low density plasma, dim, purplish glow (for hydrogen). This is not an optimal regime as the plasma intensity is low, however, as the power is slowly increased, the plasma will typically jump to the inductive mode and stay there even when the power is decreased back to the original starting point. While inductively coupled plasmas are more ionized than capacitively coupled plasmas, they are still considered weakly ionized plasmas. The color of the plasma is due to the radiative recombination of charged particles. The ion-electron recombination produces photons in the process, and the photon energy can be used to determine ionization efficiency. The visible spectrum of light from the ionization

of hydrogen displays four wavelengths, 410 nm, 434 nm, 486 nm, and 656 nm, where the 656 nm is the H-α line, the dominant visible line which makes hydrogen plasma reddish in color [24].

Inductively coupled plasmas are driven by the varying RF current in the antenna which in turn produces a varying magnetic field in the plasma. This then induces an electric field that accelerates and energizes the cold electrons in the neutral gas to start the plasma discharge. The inductive discharge is characterized by a high density plasma, with a bright glow and red color (for hydrogen). Inductively coupled plasmas are the preferred regime for operation as it provides much higher current density and higher atomic fraction which will be further elaborated on in this chapter. For typical plasma sources used in laboratory applications, the plasma discharge is formed through the subsequent collision of the energetic electrons with neutral atoms to further ionize a cascade of electrons. The electrons that are ionized from the atomic orbitals also can become excited, if there is a method of exciting them, and contribute to the ionizing process [25]. The varying RF field is produced by driving a RF current through a conductive antenna coil, which can either be immersed inside or outside the plasma chamber separated by a dielectric. Figs. 2.2 and 2.3 show diagrams of two inductively coupled plasma sources, with a planar spiral antenna and a cylindrical antenna, respectively.

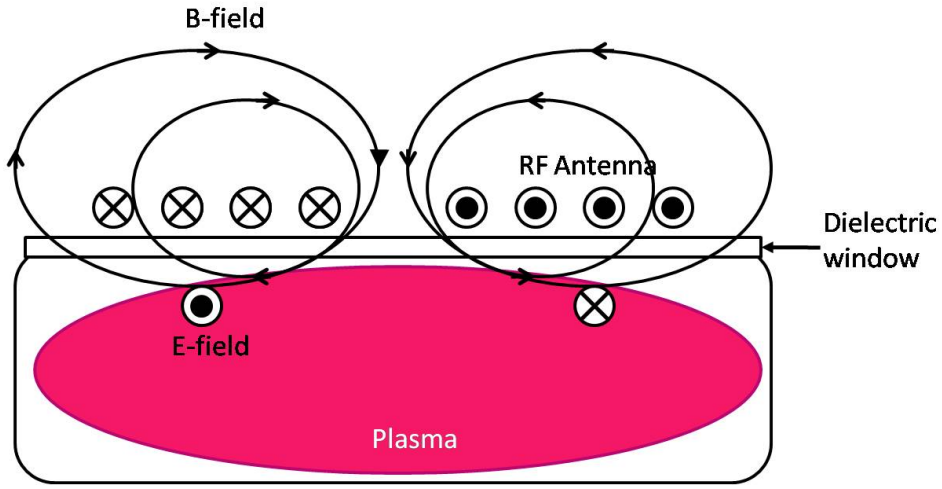

Figure 2.2: Diagram of an inductively coupled plasma using a planar antenna. The varying magnetic and electric fields can be seen.

An RF generator is used to drive the RF currents through the antenna coil to heat the plasma with the RF fields, and a matching network is needed to match the impedance of the antenna and plasma to the 50 Ohm impedance of the RF generator in order to maximize the power deposited in the plasma. Figs. 2.4 and 2.5 show a schematic and photograph of

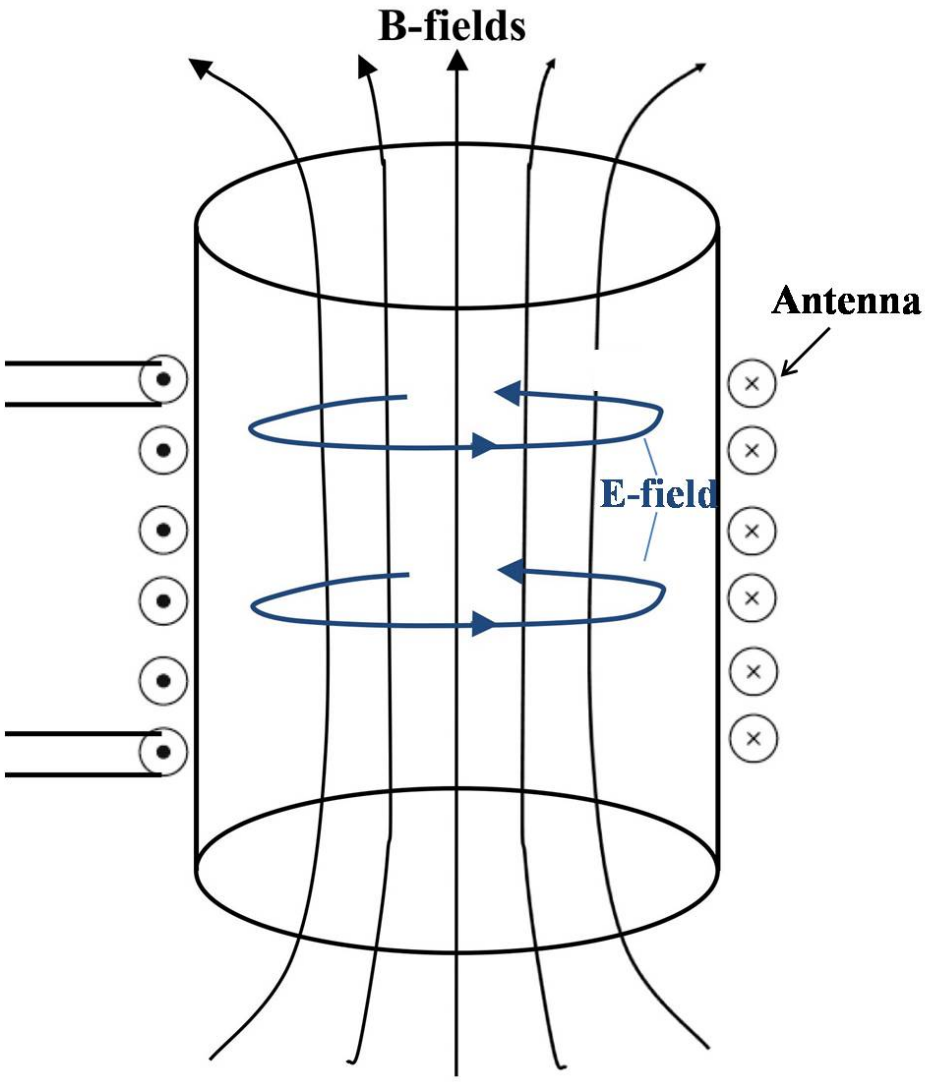

Figure 2.3: Diagram of an inductively coupled plasma using a solenoidal antenna. The plasma chamber usually has a high aspect ratio compared to the planar source.

the matching network used, respectively.

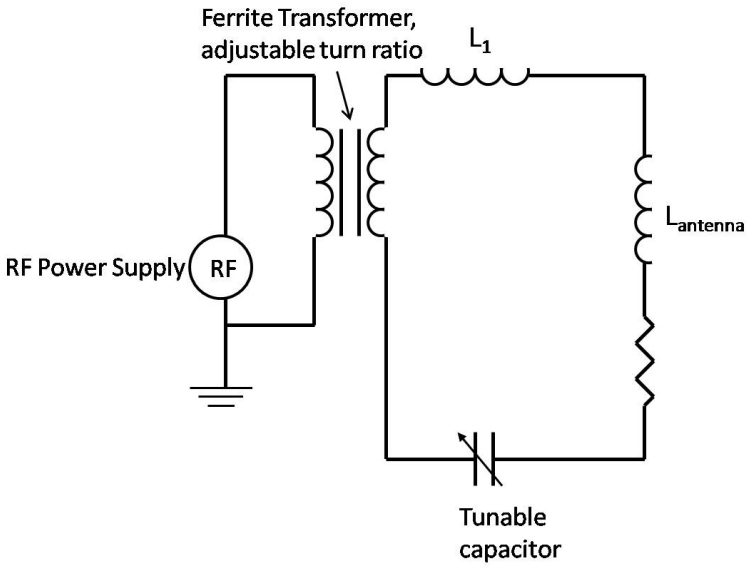

Figure 2.4: Schematic of the matching network used that uses a ferrite transformer to drive a series resonant circuit in the secondary that includes the antenna. The 50 Ohm output impedance of the RF power supply is matched to the antenna by adjusting the transformer turn ratio and adjusting the capacitor.

2.1.2 Advantages of RF to Penning Ion Sources

*Current commercial API neutron generators utilize Penning ion sources [26] that have a very poor atomic ion fraction, <10%, making it necessary to have high ion beam current and energy to achieve the necessary neutron yield. For these Penning ion sources, the lifetime of the extraction aperture is also an issue. These sources have high cathode voltages which accelerate the ions towards the plasma electrode, causing sputtering of the extraction aperture and produce an increasingly larger beam spot as time goes on. Having a small ion beam diameter is an important parameter in API because it determines the resolution of the resultant image. Current API neutron generators can only achieve an initial beam diameter of about 2-mm, which will continue to increase as the operation of the source progresses. Recently development of ion sources for use in neutron generators has been investigated by the Plasma and Ion Source Technology (PIST) Group at the Lawrence Berkeley National

*Reprinted with permission from Y. Wu, *et. al*, IEEE Transactions on Nuclear Science, Vol. **56**, No. 3, pp. 1306-1311, June 2009. Copyright 2009, Institute of Electrical and Electronics Engineers.

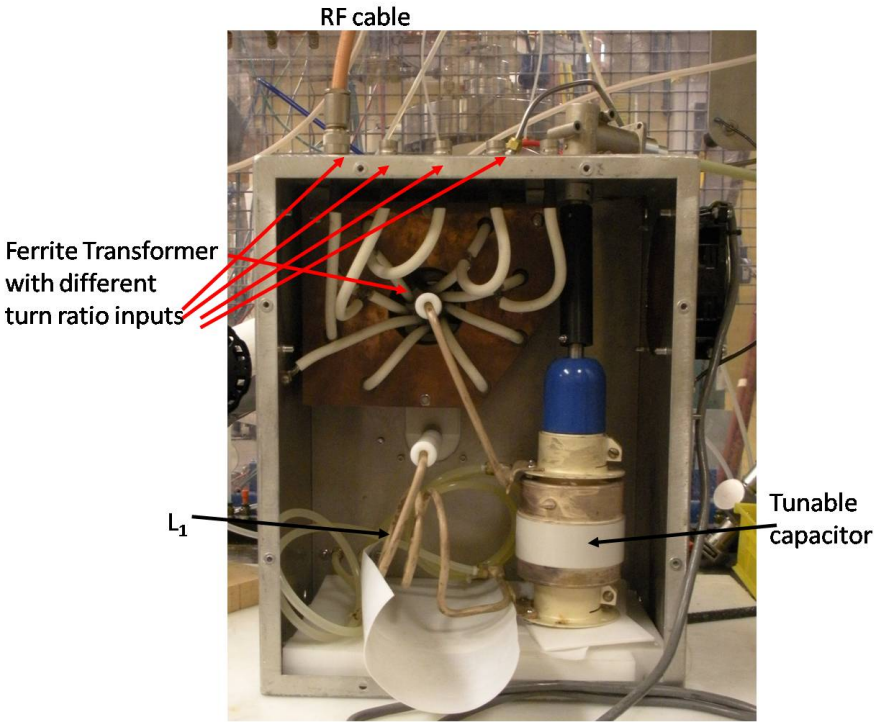

Figure 2.5: Photograph of the matching network with the back panel removed. The ferrite transformer, tuning capacitor, and the inductor L_1 can be seen.

Laboratory (LBNL). Inductively coupled, RF-driven ion sources have been used extensively for these generators [27, 28, 29]. However, these neutron generator systems require the use of a high-powered RF-driven ion source and external water-cooling, making portability a significant issue. Therefore, the development of a portable neutron generator discussed in this article that does not require the use of a large RF power source or a water-cooling system would be advantageous. It is anticipated that this neutron generator will achieve a neutron yield of between 10^7 to 10^8 n/s with a 1-mm ion beam diameter on target. A comparison between the specifications of this RF-driven neutron generator and the current Penning ion source based neutron generators is shown in a chart below in Fig. 2.6 [30].

Comparison of RF and Penning ion sources

Ion Source:	RF	Penning
Power consumption:	100-150 W	20-40 W
Ion beam current:	20-50 μA	60 μA
Ion beam energy:	80 kV	95 kV
Ion Beam spot size:	≤1-mm	≤2 mm
Atomic ion fraction:	> 80%	< 10%
Cooling:	Air	Air
Life-time:	1000 hrs	300 hrs

Figure 2.6: A comparison between the RF ion source to be used in the new RF-driven API neutron generator and the Penning ion source used in commercially available neutron generators. The requirements for the ion beam current and energy are less for the RF source as compared to the Penning source due to the greatly increased atomic ion fraction in the plasma.

2.2 Requirements of the API Ion Source

Previously, inductively coupled RF-driven ion sources have been used to produce high current (1-10 mA of beam current on target) and high atomic ion fractions (>90%) for neutron generators. However, these sources operate at high RF powers (1 to 5 kW) [32, 33, 34] and require a great deal of water cooling. This particular neutron generator for API differs from

previous developed neutron generators in that the idea is to make it as small and as power efficient as possible. The main drive behind a compact, low power neutron generator is portability, and being a low power discharge one can use a battery or a much smaller power supply instead of a large power supply which can be rather bulky and difficult to transport. A portable neutron generator allows fast identification of the presence of explosives in tight or small spaces. Previous neutron generators have always been focused on getting as much beam power on target as possible and maximizing the neutron yield. However, it has been shown that the extractable current density is linearly proportional to the input RF power [35]. Therefore it is necessary to design a source with a high atomic ion fraction such that even at low powers, the current density will be high enough to reach the required neutron yield. The axial neutron source for API must be operated at a low enough power to be cooled by air and still provide sufficient beam current to achieve the required neutron yield with continuous-wave (CW) operation. Also, the neutron tube must be completely sealed and non-water cooled to avoid any tritium contamination and be easily portable. The atomic ion fraction must also be high ($> 80\%$) so that the beam power requirement is low [31].

2.2.1 Pressure Requirements of the Ion Source

Another parameter that must be taken into account is the pressure. Due to the sealed environment of the neutron tube, the operating pressure in the ion source is equal to the pressure in the acceleration column, and if the source pressure is too high, breakdown can occur in the acceleration column. When an ion beam passes through the accelerating column, it may ionize some of the background gas. Stray ions may also hit the electrode and create secondary electrons. Therefore, the neutral gas pressure inside the ion source must be low enough such that voltage breakdown will not occur. Breakdown is determined by the Paschen curve, as well as the electrode shape and smoothness. Typically the pressure inside the accelerating chamber is at the lower end of the Paschen curve, so the breakdown voltage can be increased by decreasing the operation pressure [36]. However, low pressures inside the ion source can also lead to a decrease in the plasma density, as well as making starting a plasma discharge very difficult. Because of this side effect, this project also looked at the viability of using higher frequencies, which makes plasma ignition easier at lower pressures. Both internal and external antennas can be used in a RF plasma source, but internal antennas face the problem of degradation in the plasma, and if a problem arises, it cannot be changed without taking the whole source apart. As a result of all this, all the plasma sources investigated utilize external RF antennas. Therefore, investigation and development of a low-power, low pressure RF-driven ion source is necessary to meet the ion source requirements for API.

2.3 Ion source configurations and experimental setup

Preliminary testing of the ion source was performed with a Faraday cup and magnetic mass spectrometer. Many different source configurations have been examined to achieve the highest atomic ion fraction as well as the lowest operating pressure using the least amount of power. Hydrogen and deuterium were the two gases used in the experiments. The first parameter to be looked at in the present work is source dimension. Originally, the plan called for a source as small as possible to be developed for portability purposes. However, it was quickly realized that unless the source was a certain size, it was impossible to operate at low pressures due to the fact that there was so much loss to the walls in small sources. The set-up was nearly the same with sources of all sizes. A typical configuration is shown in Fig. 2.7. The difference between all the source configurations was the size of the plasma chamber, the RF antenna design, the source material, and presence of magnetic fields. This was the set-up used for all but the first one of the sources that were tested. The source was a cylinder made from either copper, aluminum, alumina, or quartz with one end open and one end closed off. It was attached onto the plasma electrode by a rubber O-ring and pumped down to high vacuum. The plasma electrode encloses the plasma within the surrounding wall. The Faraday cup and secondary electrode were grounded for all the ion current extraction experiments while the plasma electrode was biased at positive 10-12 kV. Different antenna designs involving planar spiral antennas with different number of turns and different inner and outer diameters were used. Helical antennas which surrounded the side of the antenna were also tested. Magnets were also used in both cases to improve the source. Different materials were used to test their effects on the atomic ion fraction and current density of the ion source, which will be discussed later in the plasma ion mass spectrometry section. The plasma electrode was made from aluminum, due to the fact that it is easily machined and shaped, and can readily form a layer of aluminum oxide on the surface, which improves the hydrogen atomic ion fraction.

The first parameter tested was the source ignition and operating pressure. The operating pressure was affected greatly by size. As expected, the larger sources had lower operating pressures due to the fact that the source dimensions were much bigger than the mean free path of the electrons: $\lambda = \frac{1}{n\sigma}$, where λ is the mean free path length, n is the density of gas molecules in the plasma, and σ the effective electron collisional cross section. However, as the source increased in diameter and volume, the effect on minimum operating pressure gets smaller; this is because the source dimensions are effectively large enough that the only thing that affects the operating pressure is having enough electron-ion collisions such that the ionization rate is enough to maintain the plasma. The pressure then must be lowered by another method when using the larger sources, such as using higher powers or using magnetic fields to confine the electrons to increase their lifetime. Fig. 2.8 shows a plot of the source operating pressure vs. RF power for various source diameters.

The effects of different antenna configurations on the source pressure and current density

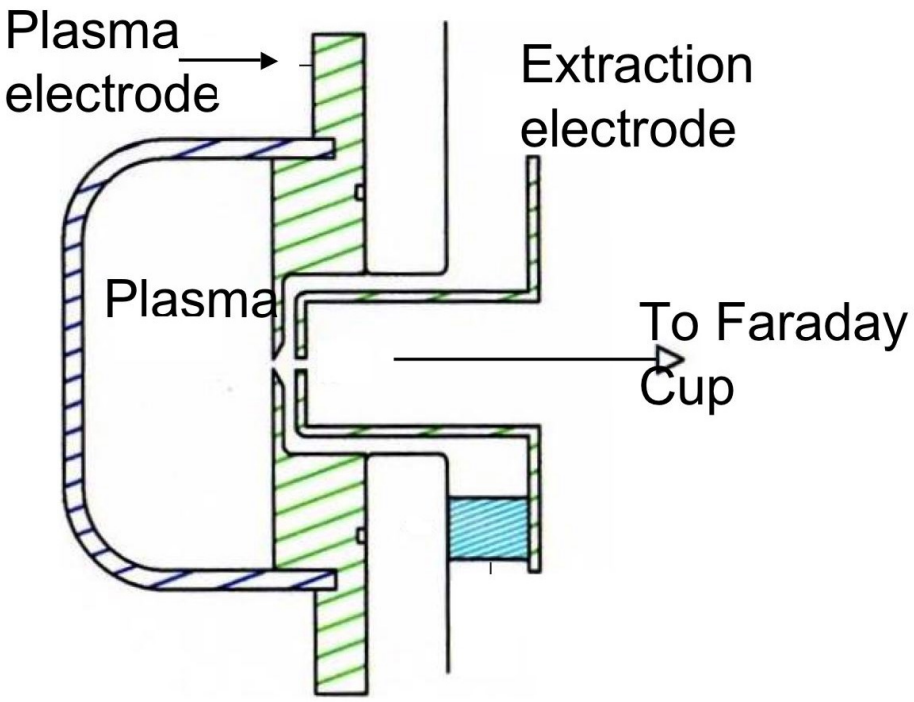

Figure 2.7: The basic plasma source and extraction set-up for testing of various ion source parameters.

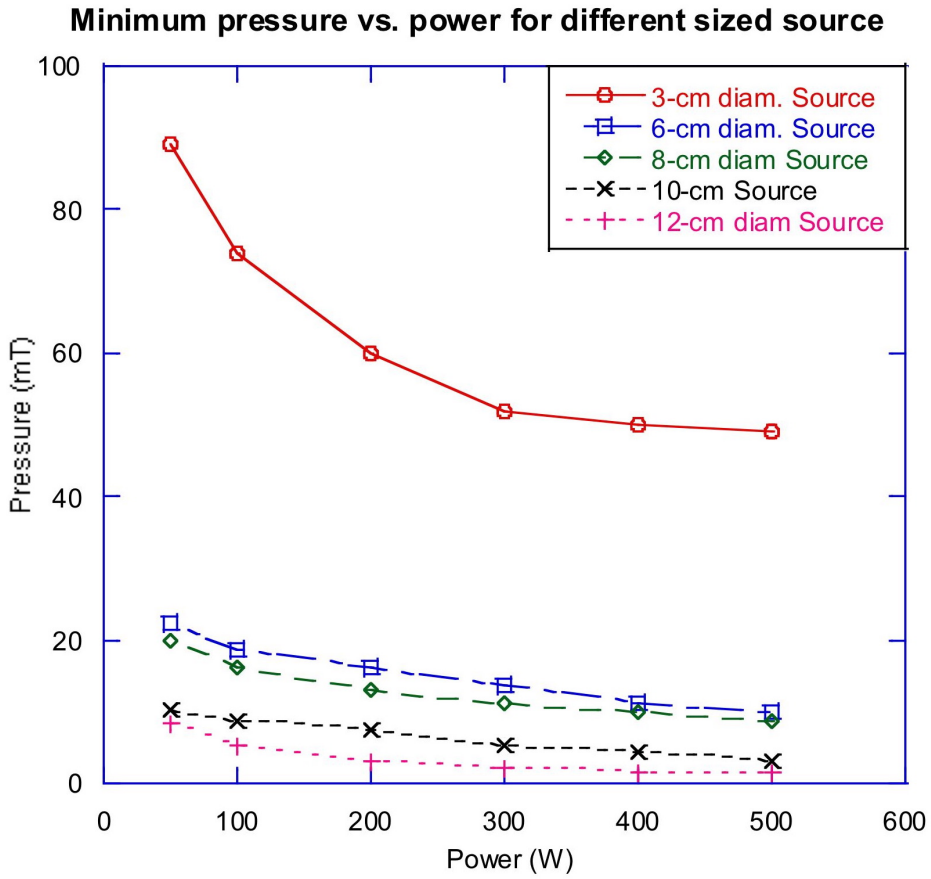

Figure 2.8: Operating pressure vs. power for different sized plasma chambers, the operating pressure drops as the plasma chamber size is increased due to a higher mean free path of the electrons.

were tested on a 8-cm diameter source, with a length of 2.5 cm. The source chamber was made from quartz. The different antenna configurations tried were spiral planar antennas, helical antennas, and spiral planar antennas with multi-cusp magnets. The first thing that was realized was that the antenna configurations did not affect the ignition pressure much at all. In fact, for all antenna configurations, it took over 100 mTorr to ignite the plasma at 100 W of RF power. However, the antenna configuration did affect the operating pressure. It was found that the planar antenna could always reach a lower operating pressure by 1-2 mTorr than the helical antenna. The reason for this is that the RF current induced in the planar antenna case is parallel to the back RF window, whereas the current induced in the helical antenna case runs parallel to the side. Due to the low aspect ratio of the source, more electrons will be lost in the axial direction than the radial direction, making the planar antenna a better choice for low pressure operation. When the cusp magnets are applied, the operating pressure drops even further. This is due to the electrons being confined by the cusp fields, and the only losses are through the cusp lines. This also increases the electron density inside which increases the ionization rate and increases the current density. Fig. 2.9 and Fig. 2.10 show the effects of different antenna configurations on current density and operating pressure.

The final two sources tested were cylindrical in shape, and had volumes of 180 cm^3 and 340 cm^3. The only antenna configuration tested was the planar coil with multi-cusp magnets on the side walls. The maximum current achieved for these two sources at a RF power of 180 W, gas pressure of 10 mTorr, and extraction voltage of 3000 kV were around 90 μA and 50 μA; respectively. One thing to note is that these sources have low aspect ratios; their height to diameter ratios are 0.47 and 0.34 for the 180 and 340 cm^3 sources, respectively. The reason why the sources are designed that way is that since the external antenna is a flat spiral antenna which sits on the bottom surface of the source, the power is coupled most efficiently into a region of a skin depth δ beneath the glass [37]. In fact, the point of maximum density in the plasma source along the z-axis would be right around the skin depth, which is usually a few cm. Therefore if the source is too long then the plasma density will be too low near the extraction aperture. Since the extraction aperture is placed at the plasma electrode, the plasma density needs to be high in the longitudinal direction near the plasma electrode. This low aspect ratio source helps to compensate for the increase in the plasma volume due to the larger radius, which reduces the overall power density in the plasma.

2.3.1 Inductively Coupled Mode Transition

Interestingly enough, in this source, when the power was increased slowly, it would first ignite, and sustain the discharge in capacitively coupled mode. The plasma looked very dim in color, and had a fairly low ion current. However, if the power passed a certain point (usually around 200 W) for this source, the current increased dramatically, and is associated

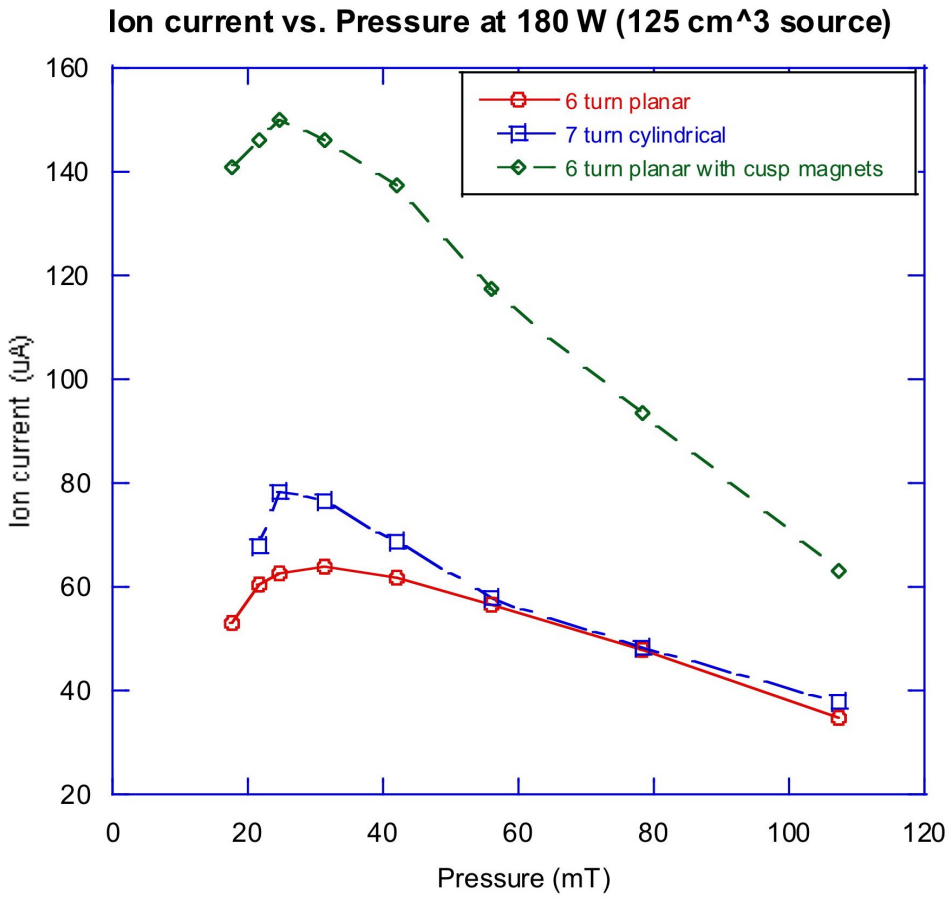

Figure 2.9: The different antenna configurations and their effects on the extracted ion current can be seen here. The biggest jump in ion current was when multi-cusp magnets were used, thus increasing the electron confinement.

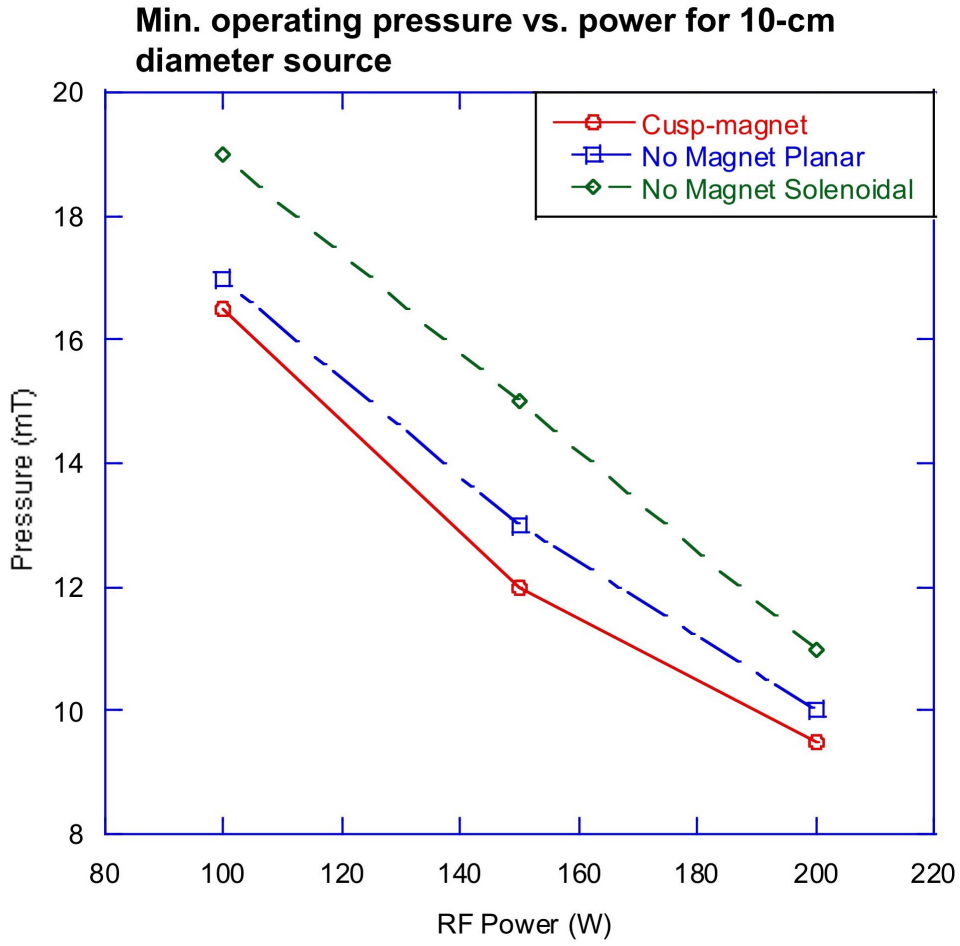

Figure 2.10: The different antenna configuration effects on the operating pressure as a function of power. As the power was increased, the operating pressure is lowered, and the magnetic confinement also helped in lowering the operating pressure as less electrons are lost to the walls.

with an increase in light emission [38]. This is where the plasma changed to inductively coupled mode. The power can then be lowered a bit (to about 160-180 W) and still remain in a stable, inductively coupled mode. One thing of interest to note was that while the plasma was capacitively coupled, the ion current was directly proportional to pressure, while in inductively coupled mode, the ion current increased as the pressure decreased (see Fig. 2.11).

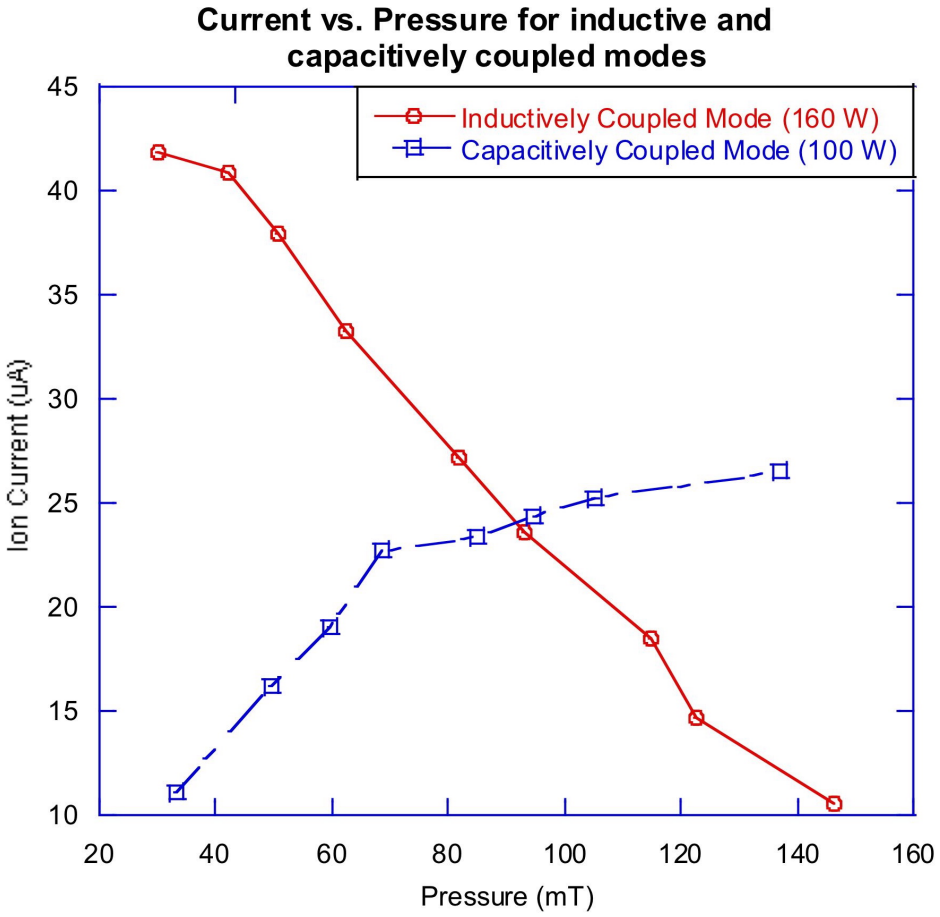

Figure 2.11: Ion current extracted vs. operating pressure for the plasma when it is capacitively coupled and inductively coupled. The inductively coupled plasma is more efficient as it produces better ionization rates at lower pressures.

The reason for this is that inductively coupled plasma (ICP) sources have much higher power efficiency, and there is a maximum density at which the power absorption is maximum in the plasma; when the density is below or above that, the plasma power absorption is lower. Effects of the capacitive to inductive mode transition have been well documented, and the

transition occurs when the RF current is above a certain minimum, which is usually associated with an increase in power and density [25]. This was also experimentally seen, when the current in the antenna increased slowly as the power was increased while in capacitively coupled mode, and increased greatly right before inductively coupled mode was achieved, and dropped to a much lower current afterwards. Fig. 2.12 and Fig. 2.13 shows the current density and I_{rf} vs. power and pressure for inductively coupled plasmas. The RF current in the antenna increases with both power and decreasing pressure. However when the plasma is not lit or when it is in capacitively coupled mode, the current is significantly higher. At a constant power of 100 W, when the plasma transitioned into inductively coupled mode the current in the antenna dropped from 11.4 amps to 8.1 amps.

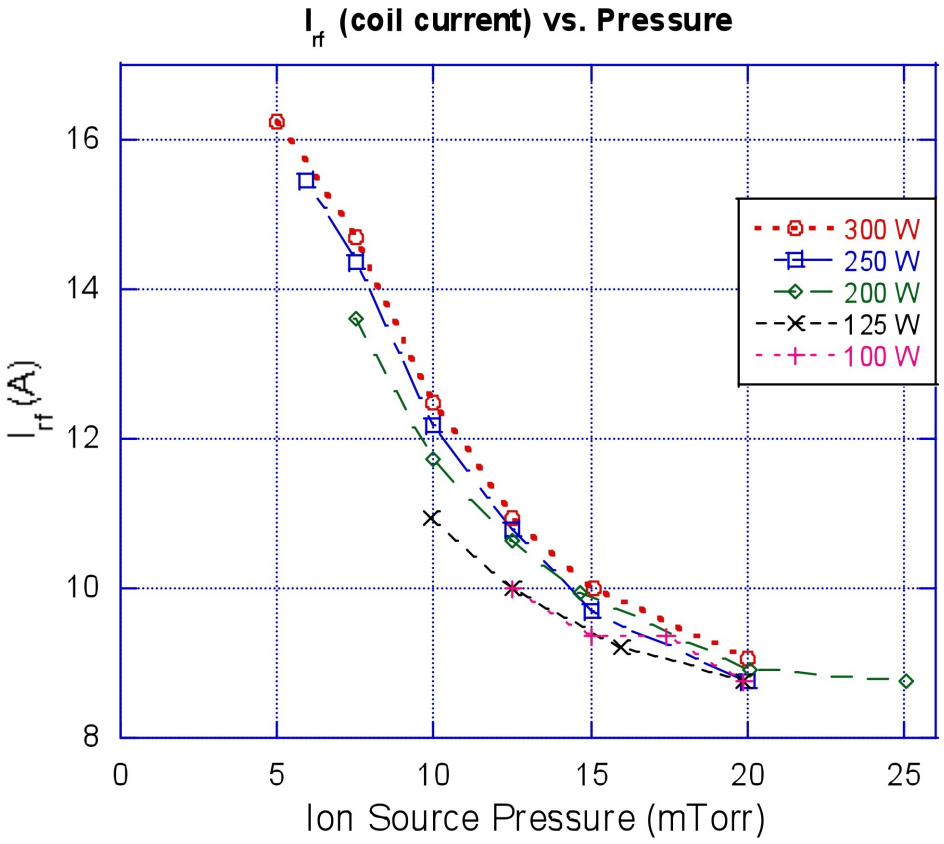

Figure 2.12: RF current in the antenna as a function of pressure for different powers for when the plasma is on. As the pressure decreases, the current increases for all powers.

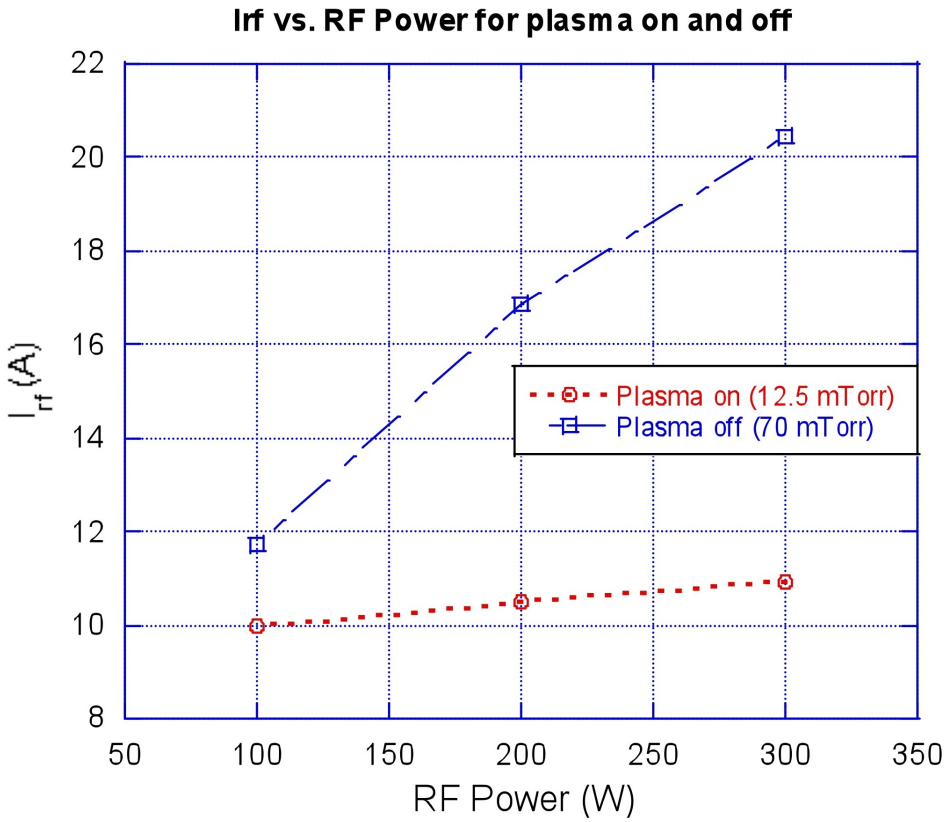

Figure 2.13: RF current in the antenna as a function of power for when the plasma is on and off. For both cases, increasing the power increases the RF current, but the current drops dramatically when the plasma is lit and in the inductively coupled mode.

2.3.2 Hydrogen Ion Species Measurement

The hydrogen species was also measured using a magnetic deflection mass spectrometer. The species was measured at different pressures for the 340 cm^3 source, and it was found that the monatomic H^+ species percentage increased with a decrease in pressure. The monatomic species also increased with an increase in power, but because of the limits on RF power, a change of 50 watts or so did not have a major impact on the H^+ species (2% difference). Figs. 2.14 and 2.15 show the atomic fraction of hydrogen vs. pressure and RF power, respectively.

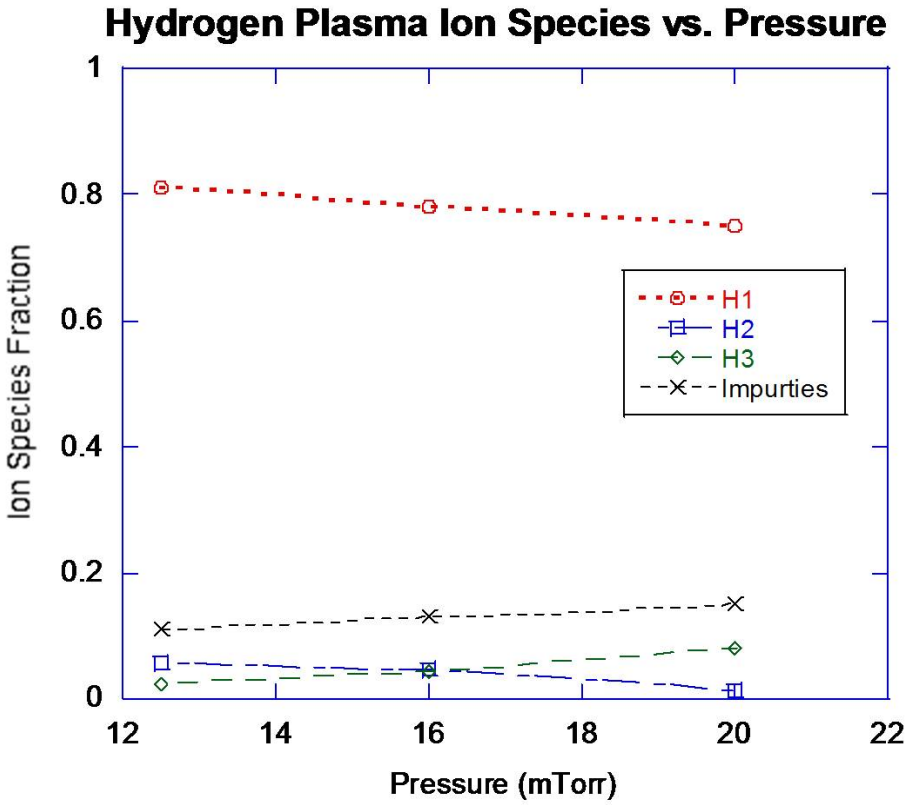

Figure 2.14: A plot of the different ion species in the plasma vs. pressure. It can be seen that an increase in the pressure causes a decrease in the atomic ion fraction and an increase in the tri-atomic species.

The reason that increased pressure lowers the H^+ concentration is that the H_3^+ species is only produced through the $H_2^+ + H_2 \rightarrow H_3^+ + H$ reaction, and an increase in pressure will increase the H_2 density, thus increasing the H_3^+ concentration, and decreasing the H^+ concentration. Similarly, due to increased ionization and particle collision from increased power

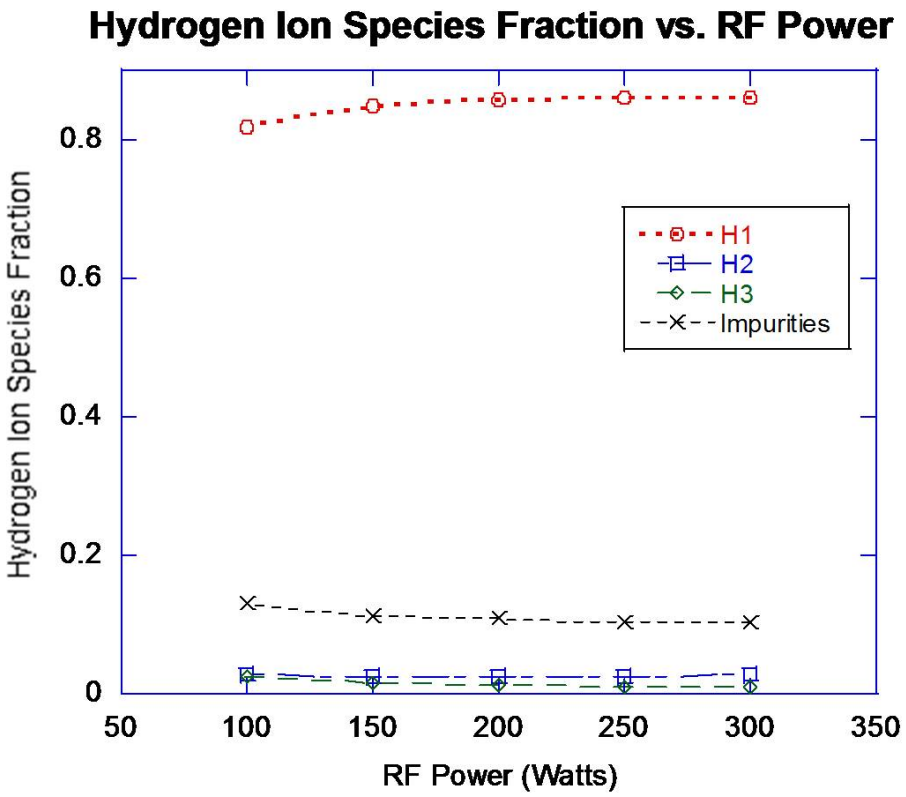

Figure 2.15: A plot of the different ion species in the plasma vs. RF power. The atomic ion fraction increases with increasing RF power.

and magnetic confinement, the H^+ concentration will be increased because all the different H^+ production reactions involve an electron-ion or electron-neutral collision. Thus increasing the life-time of the electrons and the electron density will help increase the monatomic hydrogen and deuterium species [39].

2.3.3 Multi-cusp Magnetic Field Distribution

From this study, we decided the antenna configuration for our final source must be a flat spiral antenna with multi-cusp magnets. The reason that the multi-cusp source performed so well is that the magnetic fields help to confine the primary electrons, reflecting them back into the plasma, thus increasing the mean free path and reducing the electron losses to the wall. This increases the electron density and ionization efficiency per electron in the plasma, which leads to lower gas pressure operation and higher ion current. The cusp geometry can be shown to give a good stable plasma confinement and improved plasma stability because the primary electrons have a more isotropic velocity distribution [40]. Plasma diffusion is also inhibited near the poles, and a plasma density gradient occurs mostly at the edge, where the diffusion coefficient is small. This leads to a uniform plasma distribution in the whole region, and a uniformity of about 2.5% is found in a typical multi-cusp plasma source [41]. Because ionization takes place mainly in a field-free region in the center, and since most extraction apertures are in the center, where the density is the highest, the magnetic fields do not contribute to the emittance of the extracted beam. The electron density in a low-pressure plasma could be increased by at least a factor of two or more using multi-cusp confinement. The magnetic fields produced from these poles are localized near the wall and drop off as $r^{(N/2-1)}$, where N is the total number of magnets. From the simulations below shown in Fig. 2.16 and Fig. 2.17, we can see that from the center out to roughly 50% of the total radius, the magnetic field is about 50 Gauss. This region is where the plasma is most uniform and where most of the ionization takes place [31].

2.3.4 Final Ion Source Design

Here we present the final ion source parameters constructed using a half closed quartz glass cylinder 12 cm in diameter and 3.2 cm long with an aluminum plasma electrode. The reason quartz was chosen as the source chamber material is that it has one of the lowest recombination rates of H to H_2 at the chamber surface [42]. A quartz chamber also reduces capacitive coupling between the RF antenna and the wall. Fig. 2.18 provides a schematic of the ion source, while Figs. 2.19 and 2.20 provide photographs of the ion source with the plasma on and off, respectively. The diameter of the source must be sufficiently large such that the mean free path will allow the primary electrons to gain enough energy to ionize the neutrals at pressures of less than 10 mTorr.

The antenna that drives the source is an external 4-turn, spiral antenna. We measured

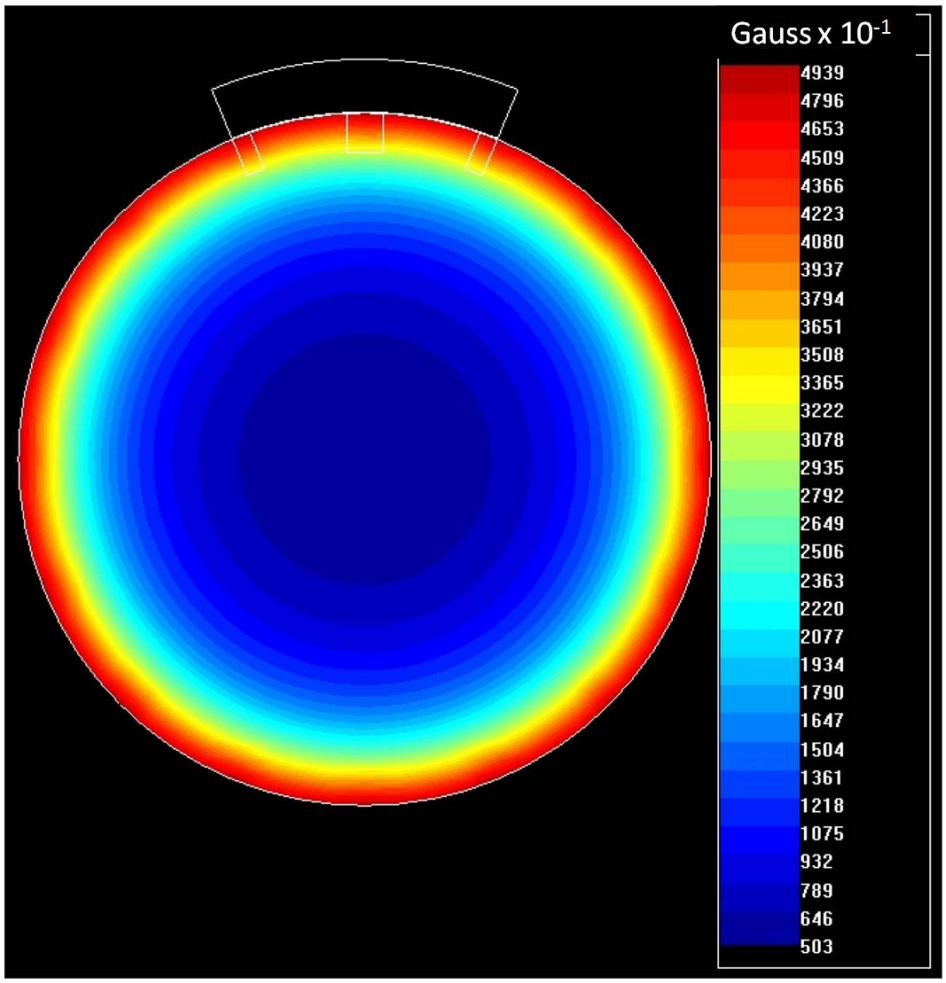

Figure 2.16: Magnetic field strength contours in a 20 magnet cusp field. The field free region here covers about 50% of the plasma in the center.

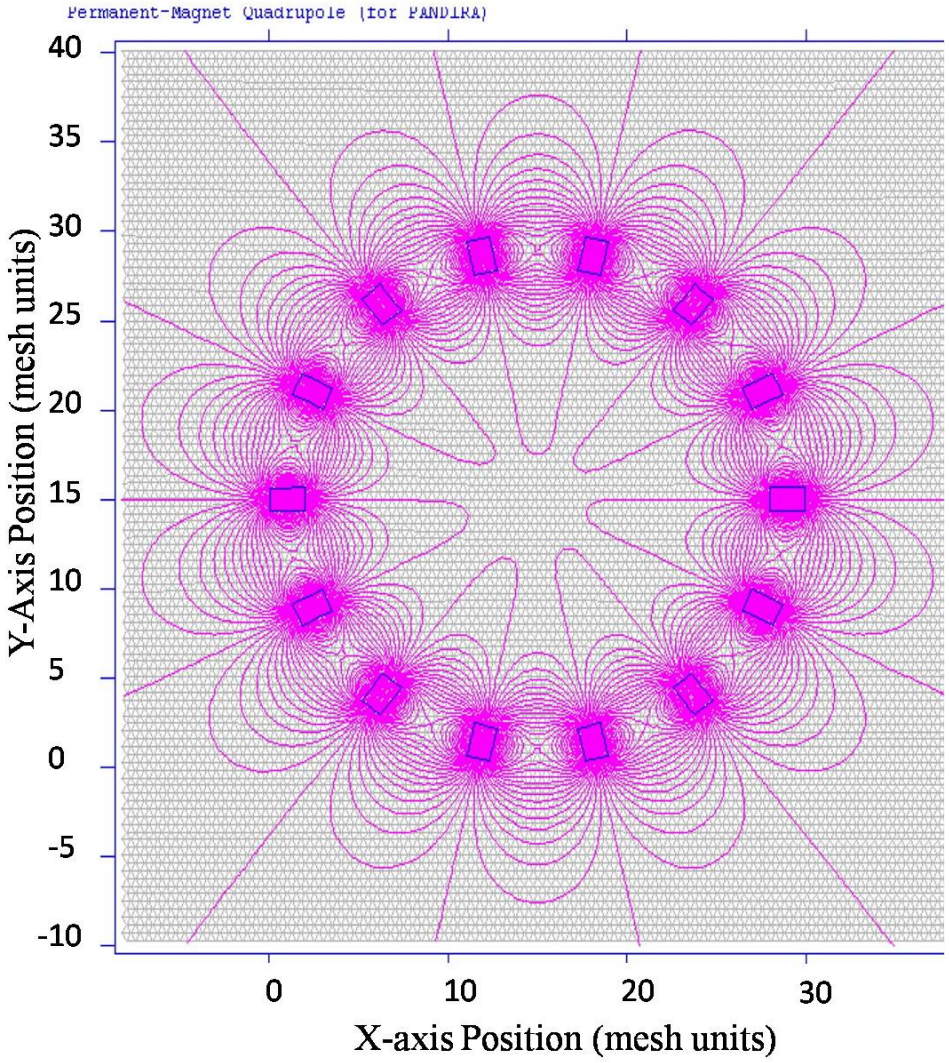

Figure 2.17: Pandira simulation of a 14 magnet cusp field showing the magnetic cusp lines .

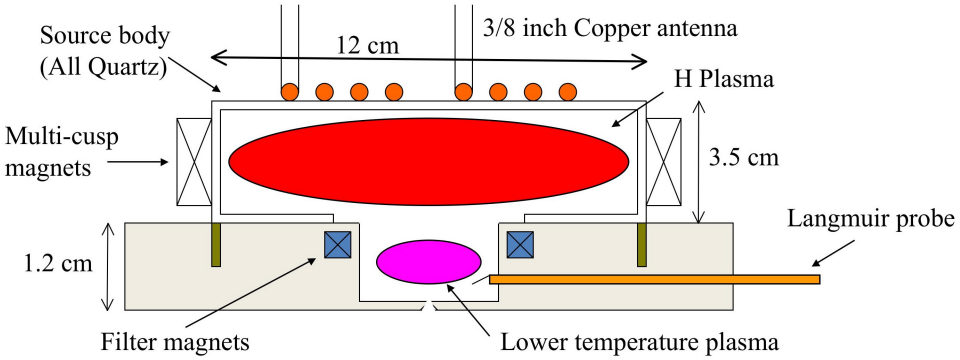

Figure 2.18: Schematic of the quartz body ion source with a 4-turn planar 1/8 inch diameter copper tubing antenna with 20 Nd-B-Fe multi-cusp magnets.

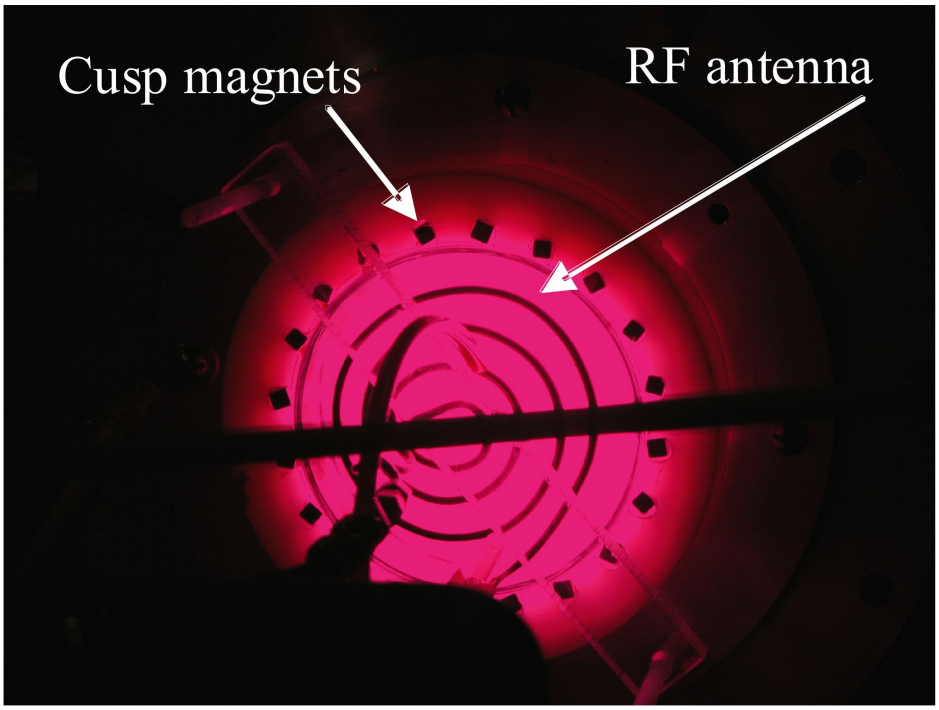

Figure 2.19: A photograph of the ion source as it sits on the test stand during operation at a power of 150 watts and a source pressure of 12 mTorr of hydrogen gas, and the aluminum plate is positively biased up to 12 kV during current density and mass spectrometry measurements. The cusp field lines formed by the magnets can be easily seen.

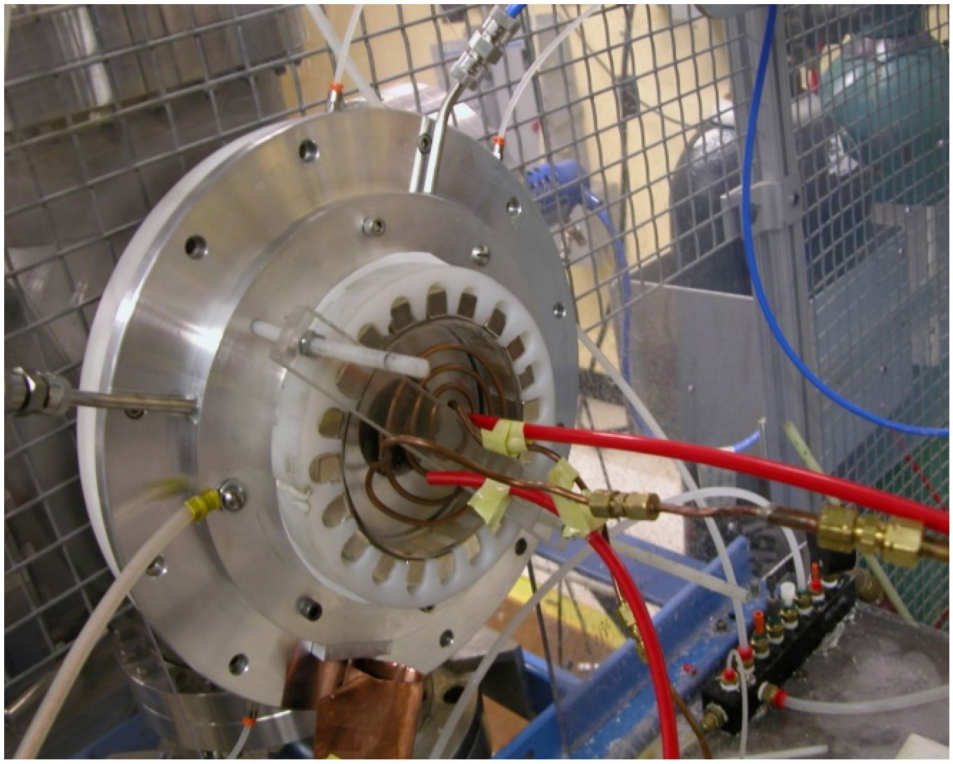

Figure 2.20: A photograph of the ion source as it sits on the test stand, the major components can be seen, such as the copper antenna, cusp magnets, and the quartz ion source.

the current density and atomic species at various operating pressures and powers for both RF frequencies of 13.56 and 27.12 MHz. It was found that with 27.12 MHz RF, the plasma can be started and sustained continuously at a pressure of 6 mTorr. The reason why the plasma can be sustained at a higher frequency is due to the electron displacement in one RF cycle. The electron equation of motion in the RF field can be expressed as:

$$m\frac{dv}{dt} = eE_0 sin(\omega t) \tag{2.1}$$

where E_0 is the RF electric field amplitude, ω is the RF frequency in rad/s, e is the charge of an electron, t is time, and m the mass of an electron. This differential equation can be solved for the velocity, which can be expressed as:

$$v(t) = v_0 - \frac{eE_0}{m\omega} cos(\omega t) \tag{2.2}$$

Integrating this one more time and assuming zero initial conditions, the electron displacement can be expressed as:

$$x(t) = v_0 t - \frac{eE_0}{m\omega^2} sin(\omega t) \tag{2.3}$$

If t is the time in 1/2 an RF cycle, one can see that the electron displacement is directly dependent on the period; as the period decreases with increasing RF frequency, so does the electron displacement. This means that for small source dimensions, a higher frequency means the electron displacement will be similar or smaller than the source diameter so that the electrons can oscillate freely without being lost to the walls and will have enough time to accelerate to high enough energies to ionize the plasma.

The plasma was capacitively coupled and the atomic ion fraction was between 50% and 60% at 100 watts. When the 13.56 MHz RF was used, the plasma needed a minimum of 80 mTorr and 120 watts to ignite, but the pressure and power could be reduced to run continuously at 12 mTorr and 100 watts, respectively, low enough to operate at less than 80 kV of extraction voltage. The plasma was inductively coupled and the atomic ion fraction was close to 85%. The transition between capacitively coupled mode to inductively coupled mode of the plasma can be seen visibly with a jump in light intensity and redness. This phenomenon has been reported in previous studies [38, 43]. The current density of the ion source ranged between 2.5-10 mA/cm^2 depending on the input power. Ultimately, we chose to use 13.56 MHz due to the high atomic ion fraction and current density, even though 27.12 MHz allowed for lower ignition and operating pressures. Fig. 2.21 show the current density as a function RF power.

From the experimental data, the measured ion current at 100 W was approximately 18 μA with an aperture of 2-mm in diameter, and the H^+ species was well over 80%. The high atomic ion species can be mostly attributed to the quartz source chamber. In the quartz

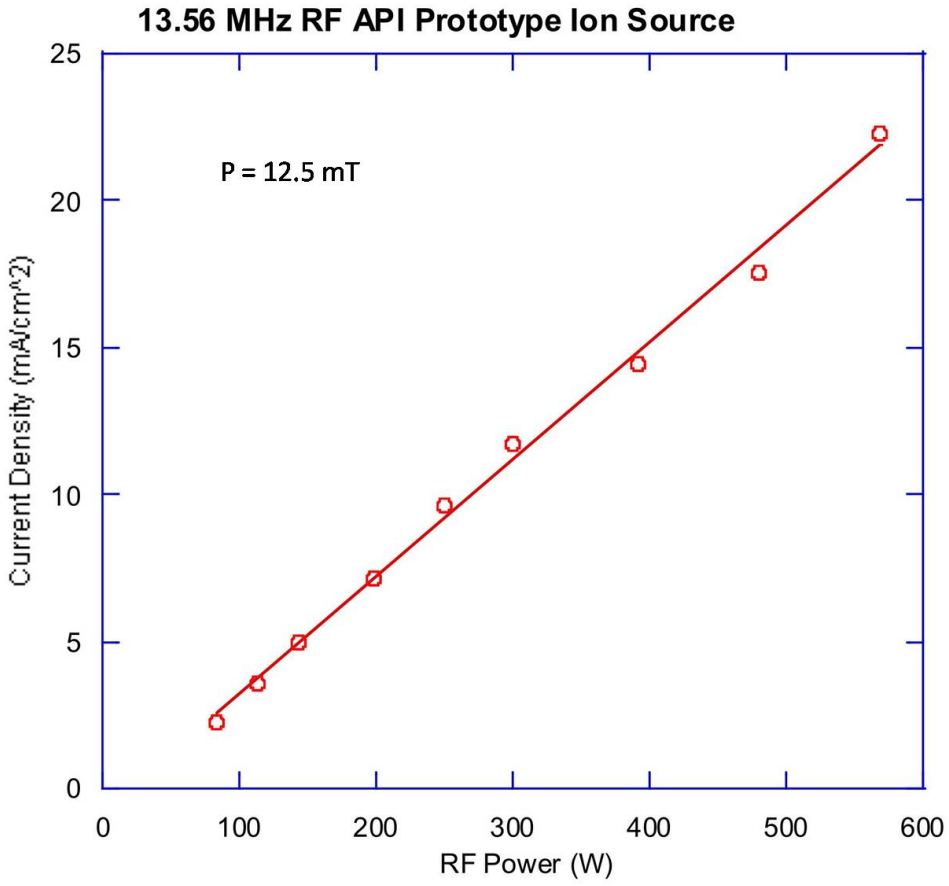

Figure 2.21: The current density of the quartz body ion source scales linearly with the input RF power, as expected. The pressure was kept constant at 12.5 mTorr and the RF frequency used was 13.56 MHz. For all powers, the plasma was sustained in the inductively coupled mode.

ion source driven at 13.56 MHz, the atomic ion fraction is 20% to 30% greater than for similar sized sources with alumina (Al_2O_3) or aluminum bodies, respectively as seen in Fig. 2.22 [32, 33].

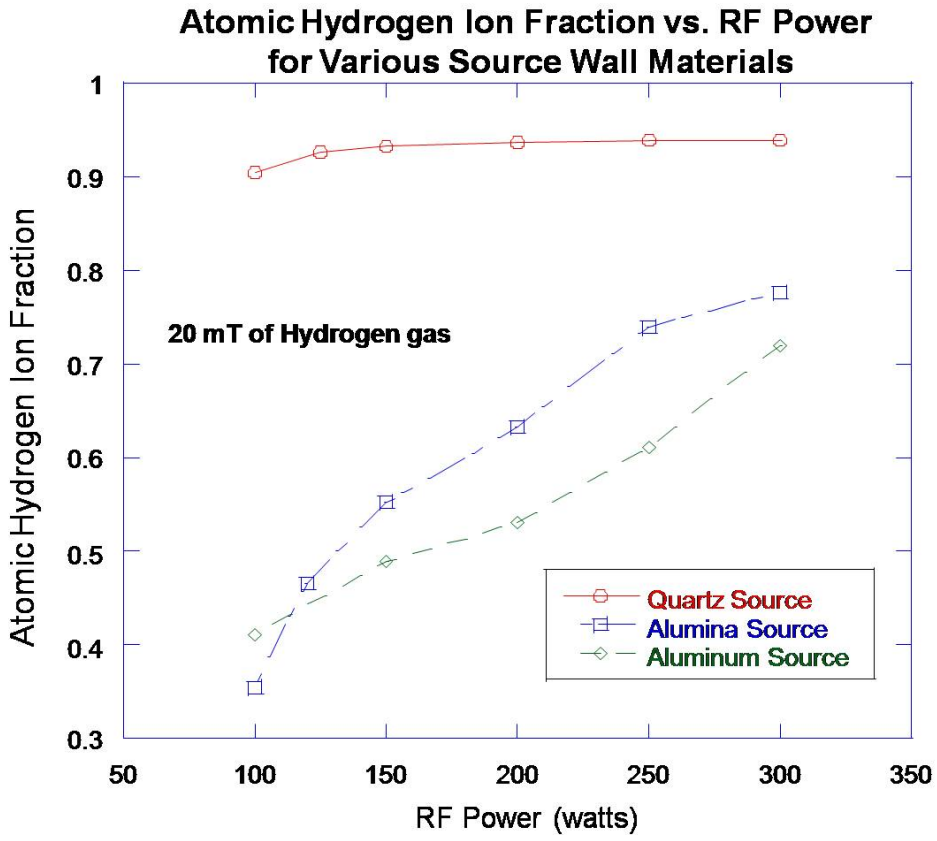

Figure 2.22: Comparison of the atomic hydrogen ion species in which the ion source wall material is made from quartz , alumina (Al_2O_3), and aluminum. Previous studies have shown that atomic ion production in hydrogen plasma sources have favored walls made from an insulating material over metal walls. However, the quartz source exceeded all expectations for its atomic ion production as over 85% of the total hydrogen ions were atomic, even at powers as low as 100 watts.

The antenna and magnet configuration were also the same for the alumina and aluminum sources. This reason for the increased atomic ion fraction with an alumina source wall is that the recombination rate of hydrogen atoms to molecules at the wall is lower for materials such as alumina and quartz compared with metals. This agrees with previous work done on the dependence of hydrogen atomic ion fraction on the ion source wall material [44,45]. At powers of 500 W or greater, however, the atomic ion fraction in the source using both aluminum and

alumina were greater than 80%. Experimental results show that at constant pressures and powers, the quartz source produces 15% to 50% more atomic ions, with maximum increases occurring at a power of 100 W. Previously, it was thought that a high power level was needed to achieve a high atomic ion fraction using RF ion sources; the current results show that 85% of the hydrogen ions are atomic with only 100 W of input RF power. Fig. 2.23 shows the mass spectrum of a hydrogen plasma at 100 W and 12.5 mTorr.

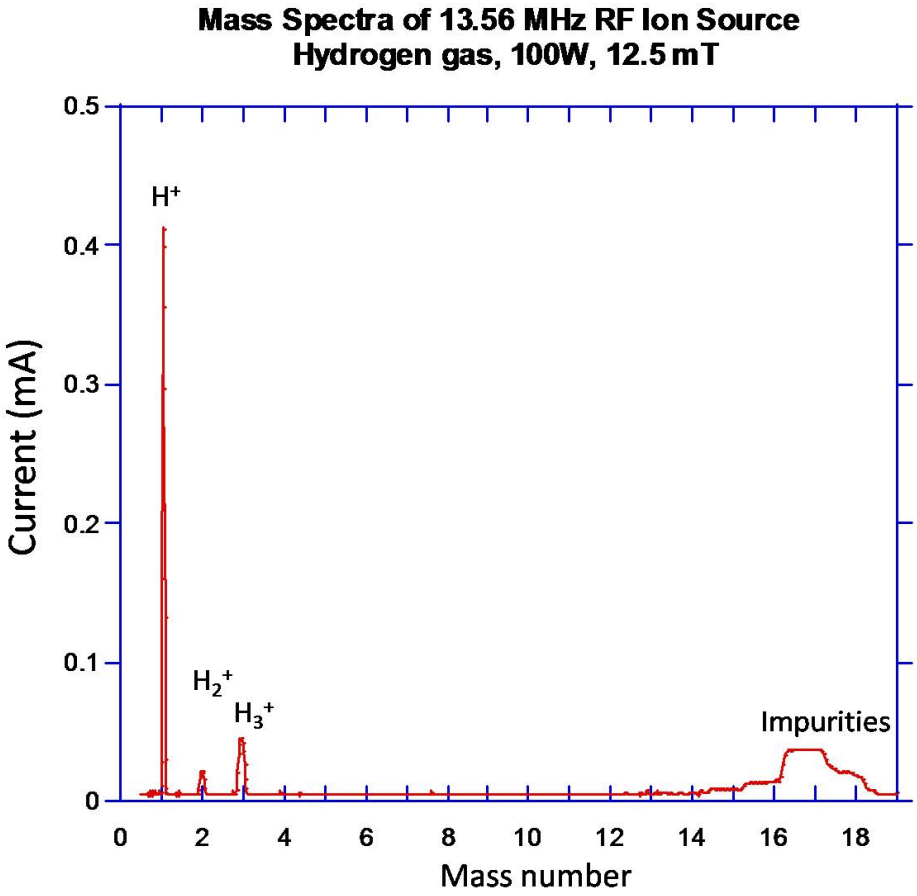

Figure 2.23: Mass spectrum of the hydrogen plasma at 100 watts of RF power and 12.5 mTorr of gas pressure. The RF frequency was 13.56 MHz. The first peak is the H^+ peak, followed by the H_2^+, H_3^+, and impurities (mostly water) peaks. The fraction of atomic hydrogen ions to other hydrogen ions is 86%. The current density extracted from this plasma was roughly 2.5 mA/cm^2

2.4 Effects of Different Frequencies on the Ion Source

*Fig. 2.24 shows the ignition and operating pressures of deuterium at both 13.56 and 27.12 MHz for a fixed RF power of 100 watts.

Comparison of 13.56 and 27.12 MHz RF

Frequency:	**13.56 MHz**	**27.12 MHz**
Ignition Pressure (for D_2)	30 mT	8 mT
Minimum Pressure (for D_2)	8.5 mT	5.1 mT
Ignition Pressure (for H_2)	50 mT	10 mT
Minimum Pressure (for H_2)	12.5 mT	7 mT
Plasma Coupling Method	Inductive	Capacitvely

Figure 2.24: Some operating conditions of the 27.12 MHz and 13.56 MHz ion source at 100 watts.

The ignition pressure is quite high for the 13.56 MHz RF frequency, and when the frequency was increased to 27.12 MHz, even though the plasma could ignite at pressures of less than 10 mTorr, the plasma was capacitively coupled, and the power must be increased to 200-300 W before the transition to the inductively coupled mode occurs and the power can then be decreased. The ignition and operating pressures are lower for deuterium than for hydrogen due to the fact that the ion confinement time is longer as a result of the larger deuterium mass. The current densities are almost the same for 13.56 and 27.12 MHz when the plasma was inductively coupled. The RF frequency used also has an effect on the atomic fraction. For a RF frequency of 13.56 MHz, the current density and the atomic ion fraction increase greatly when the plasma is in the inductively coupled mode, which is easily achieved at this frequency. In the inductively coupled mode, the plasma is denser, brighter, and has low sheath voltages, leading to lower electron energies in the plasma sheath. Capacitively coupled plasmas are dimmer, less dense (by one or two orders of magnitude), and have high sheath voltages which cause greater electron energies in the sheath [25, 43]. Therefore, the source should be operated in the inductively coupled regime because the plasma density increases by an order of magnitude and the atomic ion fraction increases by over 25% compared to the capacitively coupled mode, as seen in Fig. 2.25.

*Reprinted with permission from Y. Wu, *et. al*, AIP Conf. Proc. **1099**, pp. 614 (2009), DOI:10.1063/1.3120112. Copyright 2009, American Institute of Physics.

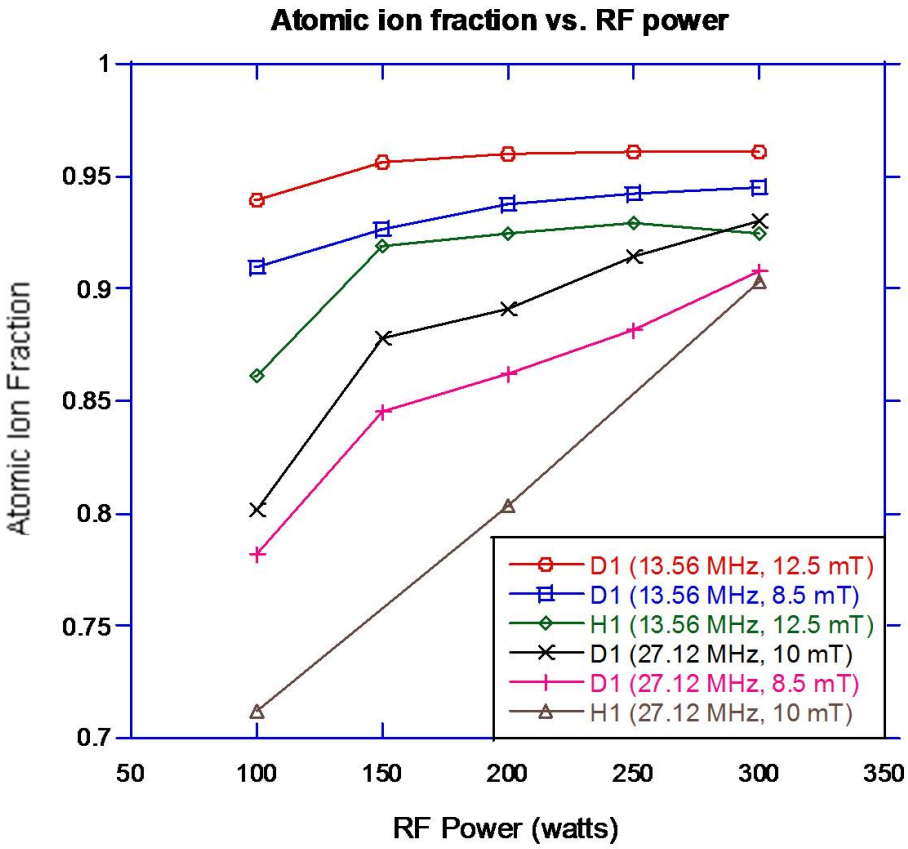

Figure 2.25: A plot of the atomic ion fraction vs. power for hydrogen and deuterium at both 13.56 and 27.12 MHz. It can be seen that the 13.56 MHz RF produces 10-15% higher atomic fraction than 27.12 MHz at low powers, but at higher powers the difference becomes roughly 5%. The difference in atomic fraction between hydrogen and deuterium also decreases from about 7% at 100 watts to 3% at 300 watts.

2.4.1 Langmuir Probe Measurements

The electron temperature and electron density have been measured with an RF-compensated Langmuir probe as a function of power for deuterium and hydrogen at 13.56 MHz, as shown in Fig. 2.26 and Fig. 2.27. The electron density increases with power due to the increased wall flux required to balance the increased power. The electron temperature decreases slightly with an increase in pressure due to the decreased ionization rate coefficient required at the higher pressure. For a deuterium plasma, the electron and ion densities are higher and the electron temperature is lower compared to hydrogen plasmas as a result of the mass difference, leading to better confinement of the heavier ion mass species [46].

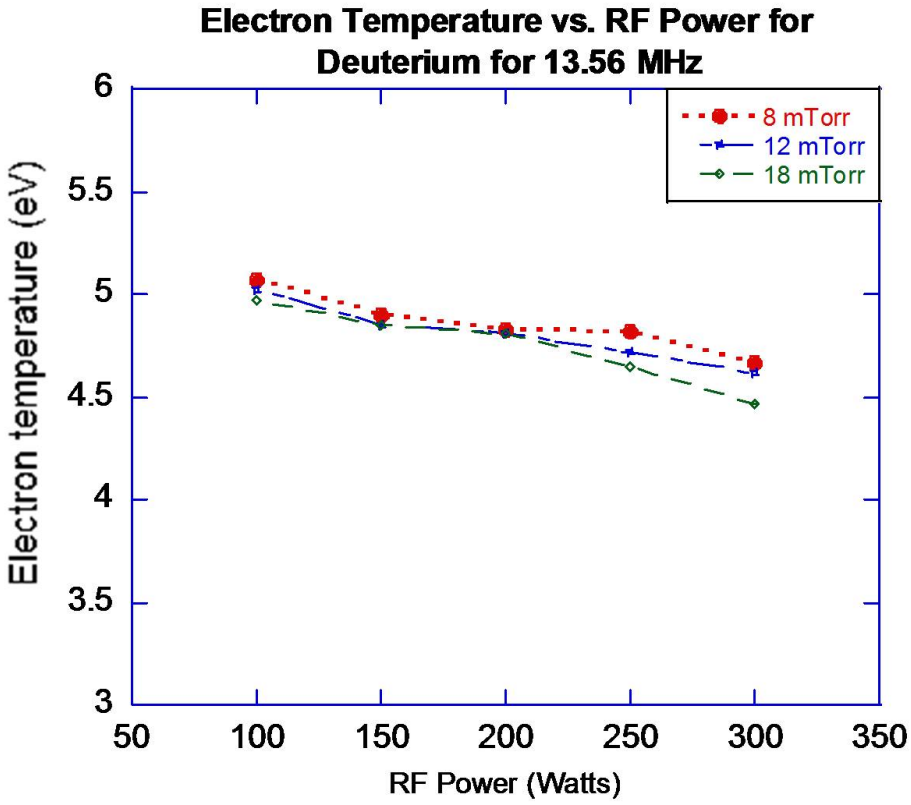

Figure 2.26: The electron temperature as a function of input RF power for deuterium and hydrogen. The electron temperature decreases with increasing pressure and is fairly constant with increasing power. The difference in electron temperature between deuterium and hydrogen is negligible.

The ion species breakdown of the deuterium plasma was also analyzed using a mass

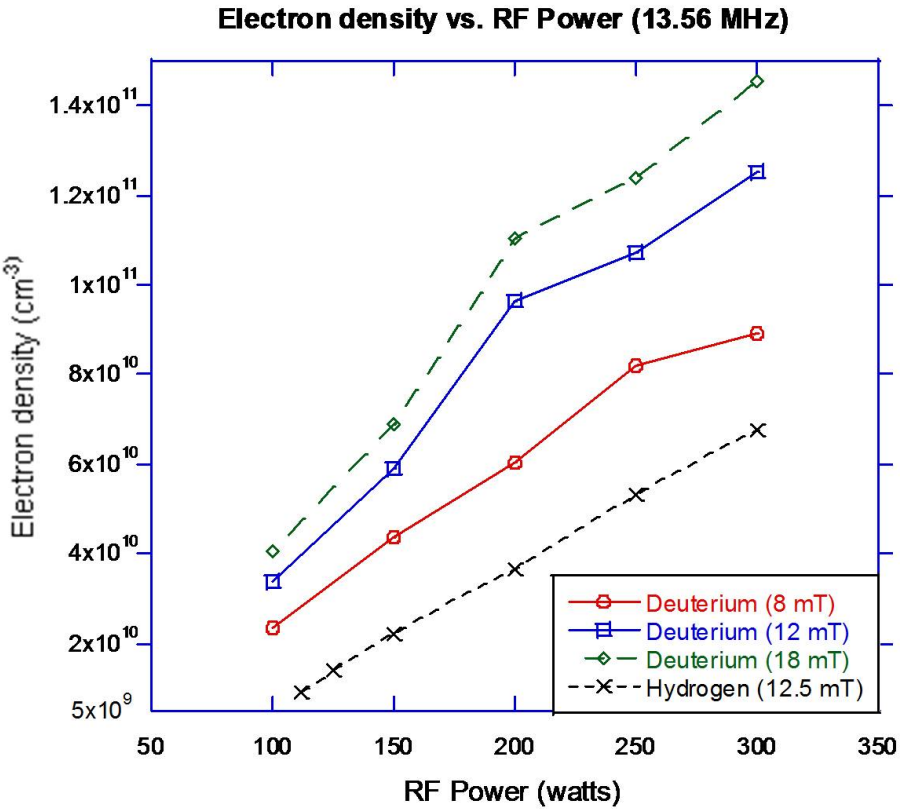

Figure 2.27: The electron density as a function of input RF power for deuterium and hydrogen. It can be seen that the electron density increases with both the power and pressure.

spectrometer. A plot of the atomic fraction vs. power and pressure for deuterium is shown in Fig. 2.28.

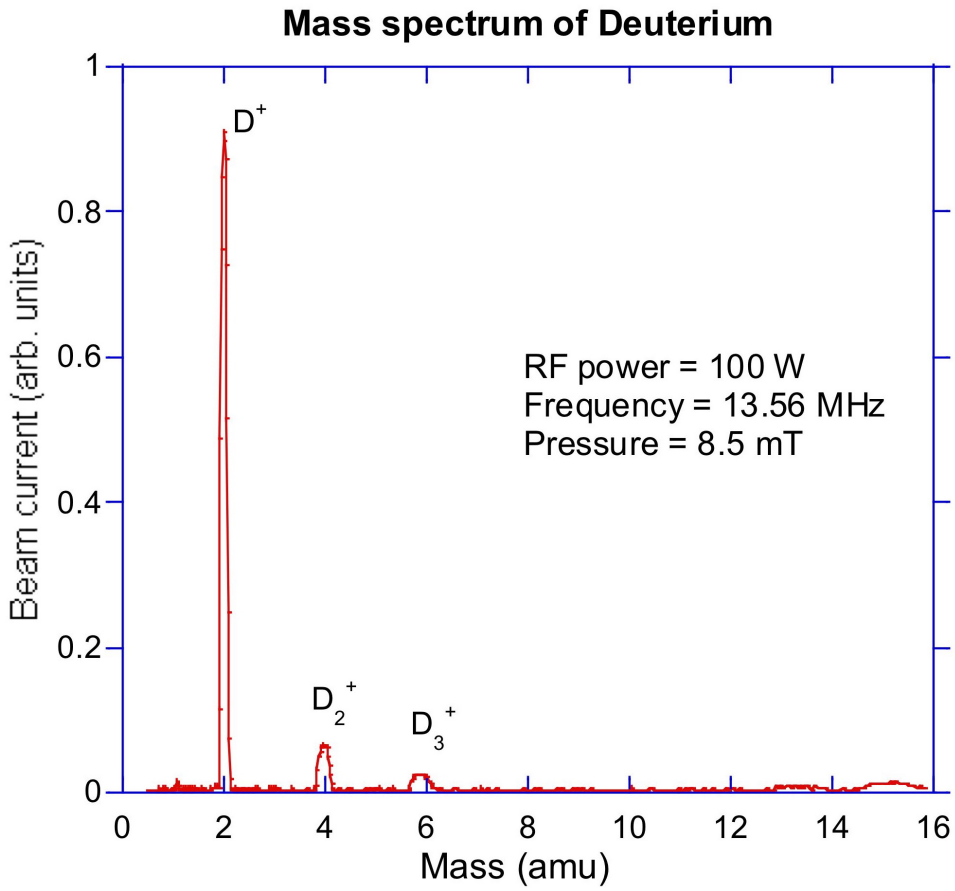

Figure 2.28: Mass spectrum of the deuterium plasma at 100 watts of RF power and 8.5 mTorr of gas pressure. The RF frequency was 13.56 MHz. The first peak is the D^+ peak, followed by the D_2^+ and D_3^+ peaks.

From this, we can see that the atomic fraction increases with increasing plasma density and decreases with electron temperature. It may seem counter-intuitive that a lower electron temperature would result in higher atomic ion fraction. However, looking at Table 3, it can be seen that the dissociation energy of H_2 is around 10 eV and the ionization energy of H is 13.6 eV, while the ionization energy of H_2 is 15.6 eV. This means that for partially ionized plasmas, an increase in the electron temperature would suppress the dissociation of H_2 to H atoms and favor H_2^+ ion formation over H^+ ion formation. Therefore, the atomic ion fraction should increase with increasing electron density and decreasing electron temperature, which

matches the global model and simulation done in [44,47]. A chart of the different ion-ion and ion-electron reactions in a hydrogen plasma can be seen in Fig. 2.29. The highest atomic ion fraction can be achieved using 13.56 MHz with a deuterium fill gas. The atomic ion fraction also increases with increased RF power and slightly with pressure up to 20 mTorr. However, due to the design of the sealed neutron generator, the pressure needs to be minimized and the atomic ion fraction is greater than 85% at pressures of less than 10 mT.

Reactions	Rate coeff.	E_r (data)	E_r (theory)
1. $H + e \rightarrow H^+ + 2e$	S_1	13.9	13.6
2. $H_2 + e \rightarrow 2H + e$	S_2	9.2	10.6
3. $H_2 + e \rightarrow H_2^+ + 2e$	S_3	16.0	15.6
4. $H_2^+ + e \rightarrow 2H$	S_4	0.33	0.0
5. $H_2^+ + e \rightarrow H^+ + H + e$	S_5	3.45	12.1
6. $H_2^+ + H_2 \rightarrow H_3^+ + H$	S_6	0.01	0.0
7. $H_3^+ + e \rightarrow H^+ + H_2 + e$	S_7	15.0	15.0
8. $H_3^+ + e \rightarrow H_2 + H$	S_8	0.38	0.0
9. $H + e \rightarrow H(2s, 2p) + e$	Q_1	10.0	10.2
10. $H_2 + e \rightarrow H_2(B, C, D) + e$	Q_2	20.0	12.0
11. $H_2 + e \rightarrow H_2(v = 1) + e$	Q_3	1.5	2.0

Figure 2.29: A table of the different reactions which produces the different hydrogen and deuterium ion species [44].

2.4.2 Mass Spectrum of a Hydrogen/Deuterium Plasma

Since the final design of the neutron generator will employ a D-T gas mixture in the ion source, hydrogen and deuterium were tested to investigate the effect of gas mixing on atomic fraction. While it is true that a mixed D/T beam will create some neutrons from the D-D and T-T reactions, the cross section for D-T is over 300 times greater, and the impact of the D-D and T-T neutrons is insignificant due to the lower cross sections and lower neutron energies. The advantages of using a mixed D/T beam and a self-loading target is that the life-time will be longer than using a pure deuterium beam with a pre-loaded tritium target. For pure hydrogen gas, there are three possible ion species, but with a deuterium and tritium mixture, there are 9 possible species with 7 different masses. With a hydrogen and deuterium mixture, there are 9 possible species and only 6 possible masses. Although this poses a difficulty in determining the exact species of all ions, the mass spectrum should

identify two large peaks at mass 1 and 2 and a very small amount for masses 3 through 6. Fig. 2.30 shows the plot of the mass spectrum of the deuterium-hydrogen gas mixture at 100 watts and 20 mT, indicating that the plasma was dominated by masses 1 (H^+) and 2(H_2^+ and D^+). Since the amount of mass 4 (D_2^+) ions is very small, one can conclude that the amount of H_2^+ ions is also minimal. Thus mass number 2 is fully dominated by D^+ ions, confirming that the high atomic fraction remains for a gas mixture.

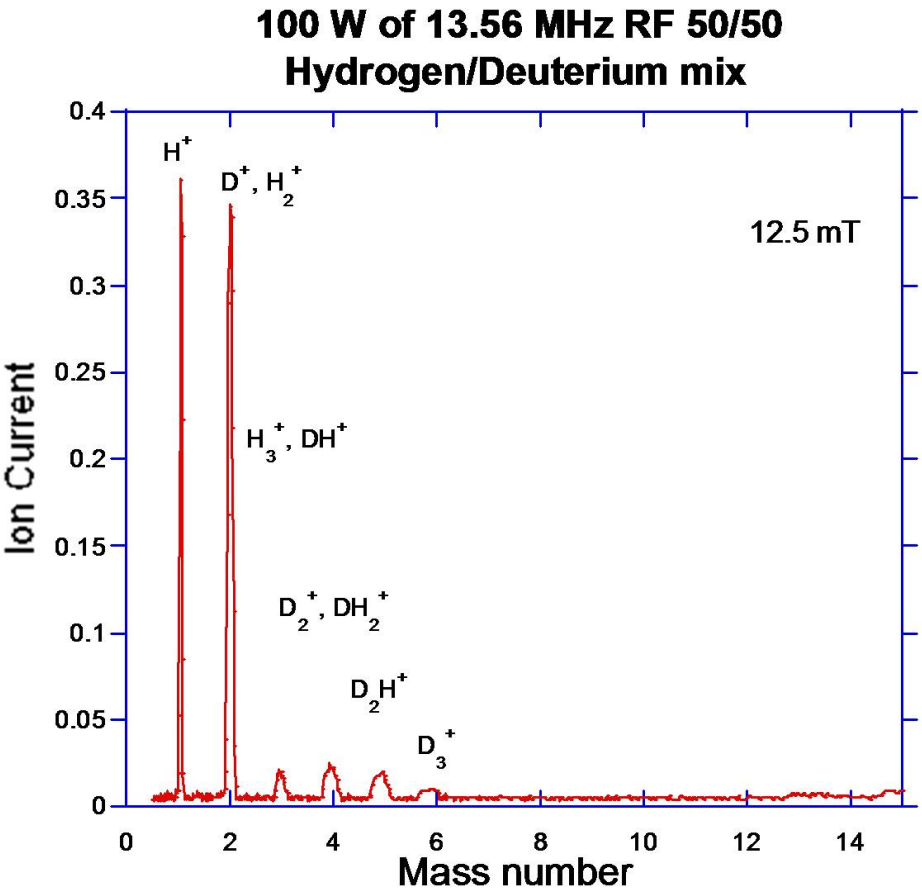

Figure 2.30: A mass spectrum of a 50/50 hydrogen-deuterium mix plasma at a pressure of 12.5 mT and 100 watts of input rf power. The plasma is dominated by mass 1 and 2, which are the atomic ion species of hydrogen and deuterium. The other 7 possible species account for approximately 10% of the total ions.

Impurities are a part of every plasma source, and in the prototype source it comprised about 10% of the plasma, over 8% of which was mass 18, or water ions. Figs. 2.31 and 2.32 show the atomic ion fractions with the impurities taken into account for both 13.56 and

27.12 MHz. In the case of the 27.12 MHz, due to the capacitive coupling that takes place at lower powers, the atomic ion fraction is simply too low at powers < 200 W. The presence of water ions is not a major concern as the final model of the neutron generator would be baked and pumped down to less than 10^{-10} torr and sealed, thus eliminating most of the impurities.

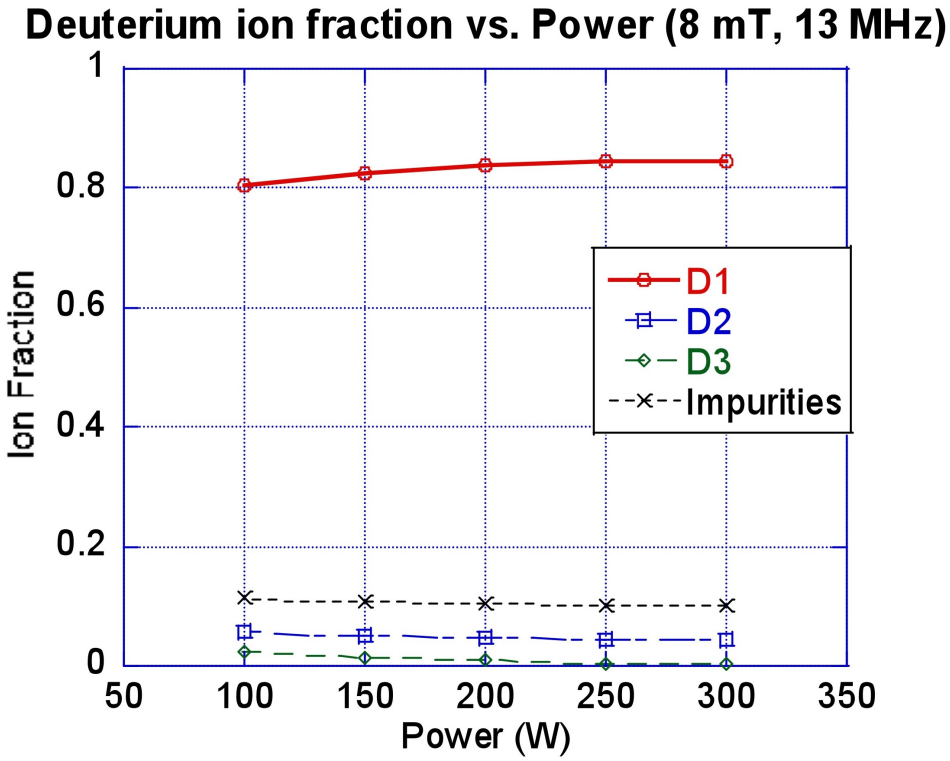

Figure 2.31: A plot of the different deuterium and impurity ion species percentage present in the plasma as a function of power. The impurities species in the plasma were mostly comprised of masses 16-18, namely oxygen, water, and D-O molecular ions. In a fully sealed and clean chamber, there should be no water present and the atomic ion fraction of deuterium should increase by about 8%.

2.5 Conclusion

A compact RF-driven ion source has been built and tested at low RF powers and the ion source parameters measured. Experiments show that the ion source using quartz as the source material with an external planar antenna and multi-cusp magnets will be able to

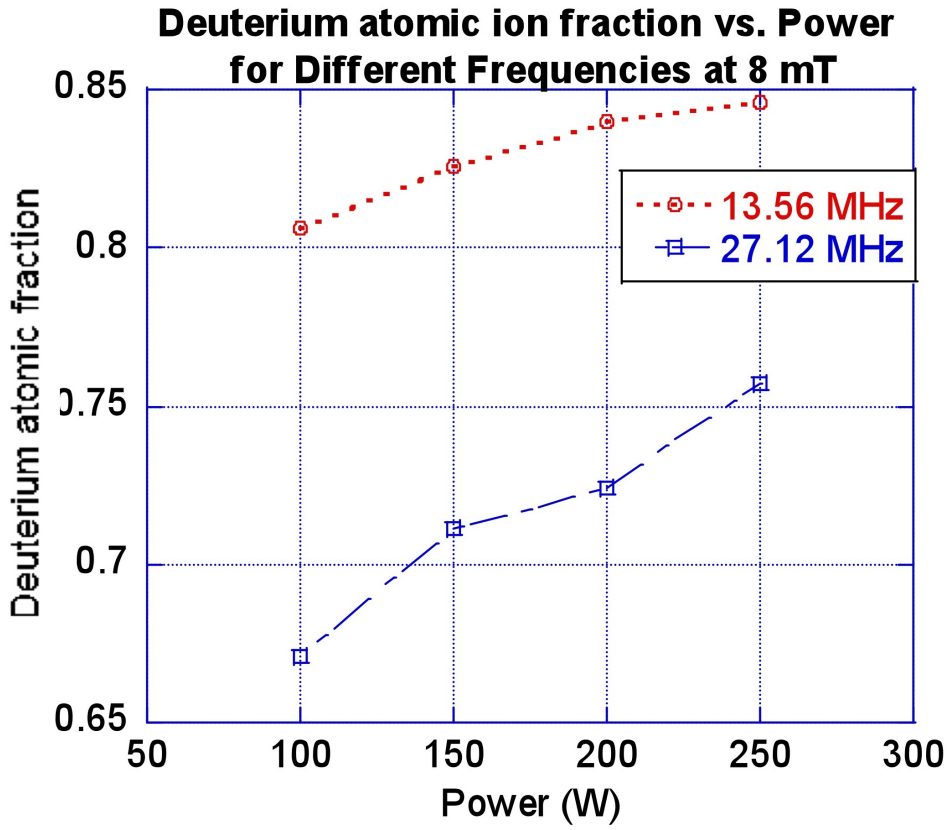

Figure 2.32: A plot of the atomic deuterium ion fraction in the plasma (including impurities) for 13.56 and 27.12 MHz RF as a function of power. It can be seen that as power is increased, the 27.12 MHz ion source increases its atomic ion fraction at a greater rate than the 13.56 MHz source, but due to its poor performance at lower powers, 13.56 MHz was chosen as the operating frequency.

provide an upgrade in source efficiency at both 13.56 and 27.12 MHz over the Penning source by producing over 85% atomic ions at a current density of 3 mA/cm^2 and thus allowing the neutron yield to increase and the beam spot to decrease without overheating the target. The preferred frequency is 13.56 MHz because it provided higher atomic ion fraction at lower powers. The RF power required was only 100 watts at a deuterium gas pressure of 8.5 mTorr. Experiments with deuterium and hydrogen have shown that atomic ions dominate in a two gas mixture. Therefore, it is expected that using a mixture gas of deuterium and tritium would also result in a high atomic ion fraction and low operating pressures. This source will greatly improve the efficiency of neutron generators for API and will allow RF sources to be compact and operate without water cooling.

Chapter 3

Ion Extraction and Target Design

3.1 Ion Extraction Fundamentals

The extraction of the ion beam from the source is just as important as creating the ions. Three main factors dictate ion beam extraction, namely the density and mobility of the ions and electrons in the plasma, the strength of the electric field between the ion source and the subsequent extracting electrodes, and the space charge of the extracted ion beam. In this chapter the basics of the ion extraction and ion beam optics of the API neutron generator are presented.

In an ion source, the ion beam is typically extracted through a single or a set of circular apertures or slits on a plasma facing electrode. The ions that come out from the aperture are then accelerated and shaped by the electric field produced from the set of beam forming metal electrodes further down from the extraction electrode by biasing each electrode at high voltage. The maximum extractable ion current from a source is governed by the Child-Langmuir law [48].

$$J = \frac{4}{9}\epsilon_0(\frac{2q}{m_i})^{1/2}\frac{V^{3/2}}{d^2} \tag{3.1}$$

where J is the current density of the ion beam in A/m^2, q and m are the charge and the mass of the ions and V [V] and d [m] are the applied voltage and gap distance between the ion source body and the extracting electrode, respectively. The assumptions here are that the plasma source is producing enough ions such that their extraction is limited by their space charge and that the ion emitting surface is planar. For RF ion sources, the first assumption is true, but the second assumption depends on the density of the plasma and the strength of the electric field at the extraction aperture. This law is useful for scaling the extraction voltage up with input RF power; since the current density increases linearly with RF power, the voltage can be scaled up by the same factor to the 2/3 power. For any given ion source,

the maximum current that can be extracted is dictated by the Child-Langmuir law. This means that for a given RF ion source operating at a constant RF power and pressure with a set extraction gap, the maximum extractable current density is dependent on the extraction voltage. At voltages below the Child-Langmuir voltage, the current extracted will be less than the maximum. At voltages above the Child-Langmuir voltage, the extractable current will not increase, but the beam trajectory will change.

Another figure of merit used to describe ion sources is perveance. It is defined as follows:

$$P = \frac{I}{V^{3/2}}\sqrt{\frac{m}{q}} \tag{3.2}$$

where I is the current, V is the voltage difference between the extraction electrode and plasma electrode, m is the atomic mass and q is the ion charge state. The perveance of an ion source is a proportionality constant that is useful in determining different ion source parameters when something else is changed [49].

3.1.1 Plasma Meniscus

The surface of the plasma which ions are emitted from is called the plasma meniscus. This is a boundary layer with a thickness of a few Debye-lengths over which the extracting electric field is attenuated to zero. The electric field in the plasma meniscus pulls and extracts the ions that have diffused into the meniscus layer. The meniscus shape and curvature are affected by the strength of the electric field and the plasma density, which act as two opposite forces on the meniscus. If the plasma density force is greater than the electric field, then the meniscus will bulge outward, giving a convex shape. If the plasma density and electric field are equally matched, then the meniscus is relatively flat. If the electric field is too high, then the meniscus will bend inwards and have a concave shape to it [23]. Fig. 3.1 a), 3.1 b), and 3.1 c) show the three cases.

Ideally, a parallel beam is desired, and to achieve such a beam a slightly concave plasma meniscus is needed. The reason being that the ion beam would over-focus and the beam trajectories would diverge due to the space charge expansion. A slightly concave plasma meniscus would help to balance the space charge effect by having the beam be more focused at the beginning due to the meniscus, and as it travels down away from the extraction the space charge will expand the beam slightly, making the beam trajectory parallel. Hence, in order to extract the desired beam current and shape, the beam trajectory depends on the ion density and electron temperature in the ion source as well as the strength and shape of the extraction electric field. To achieve a desired extraction condition for the beam the plasma density, the extraction voltage and the extraction gap distance and extraction electrode shape all need to be tuned to match each other.

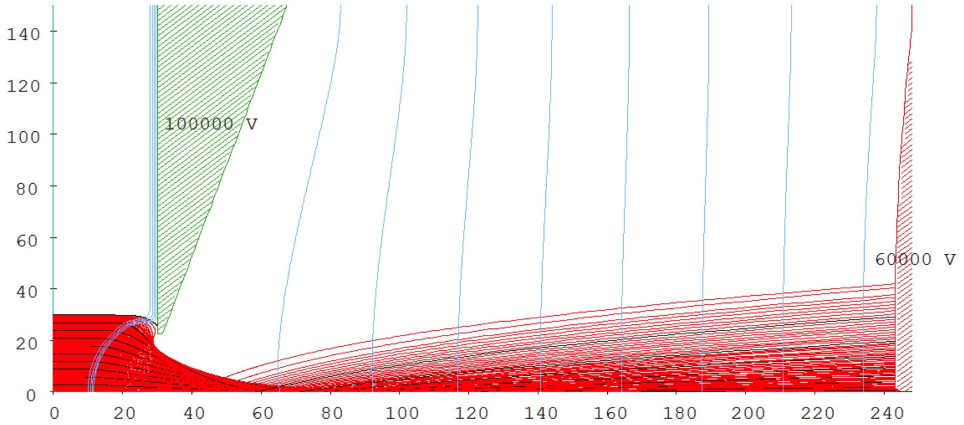

a)

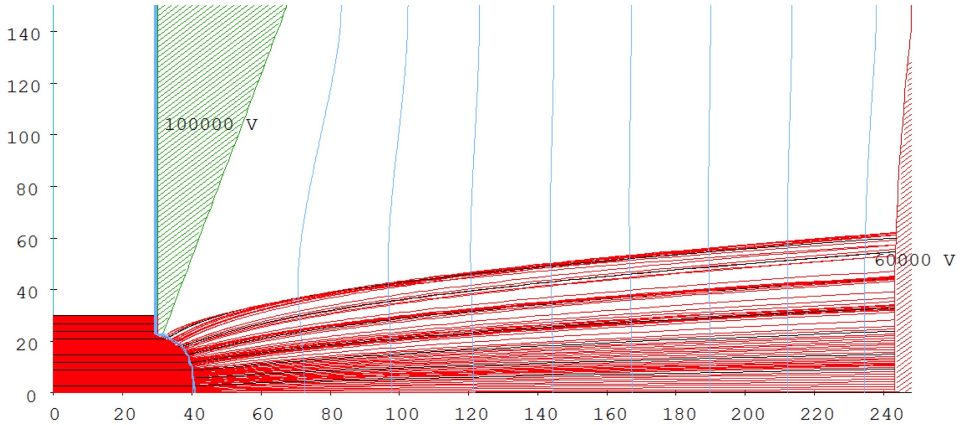

b)

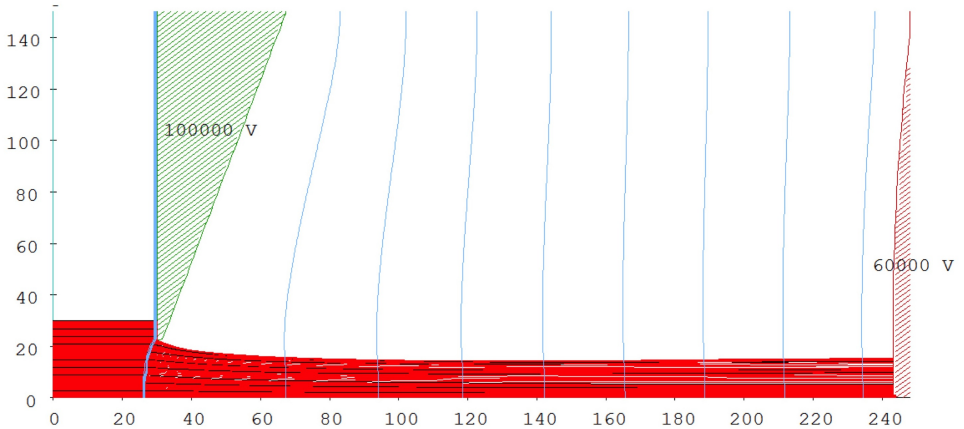

c)

Figure 3.1: a) Example of an under-dense plasma and ion extraction simulation in IGUN, the meniscus can be seen bowed inward. b) Example of an over-dense plasma and ion extraction simulation in IGUN, the meniscus can be seen bowed outward. c) Example of a well matched plasma density and ion extraction simulation in IGUN, the meniscus is fairly flat and the resultant beam is relatively parallel.

3.1.2 Beam Emittance and Brightness

Beam emittance and brightness are two very important beam parameters that largely determine the behavior of the beam as it goes through the transport column. These two parameters are mainly dependent on the properties in the ion source and right at the extraction, namely the geometry of the extraction and the ion temperature of the plasma.

Emittance is perhaps one of the most important figures of merit in describing an ion source. It is the total volume that the ion beam trajectories occupy in a six-dimensional phase space. The emittance can be expressed as (x,x'), (y,y'), and (z,z') where x, y, and z, are the space coordinates of the beam and x', y', and z' the linear momentum coordinates. In most cases the longitudinal emittance (in the z-direction) is ignored and only the transverse emittances (x,x'), and (y,y') are considered [23]. The emittance ellipse, a plot of the transverse emittance which is used to determine whether a beam is converging, diverging, parallel, or focused, is shown in figure 3.2. Emittance is often given in units of mm-mradians, where the effect of the beam velocity is ignored by normalizing the emittance by expressing it as:

$$\epsilon_n = \beta\gamma\epsilon. \tag{3.3}$$

where $\beta = \frac{v_z}{c}$ is the ratio of the beam velocity to the speed of light and $\gamma = (1-\beta^2)^{-1/2}$.

Beam brightness is defined as the ratio of the extracted ion beam current to the product of the transverse emittance values:

$$B = \frac{I}{\epsilon_x \epsilon_y} \tag{3.4}$$

where I is the ion current and ϵ_x and ϵ_y are the transverse emittance values in (x,x) and (y,y) planes [51].

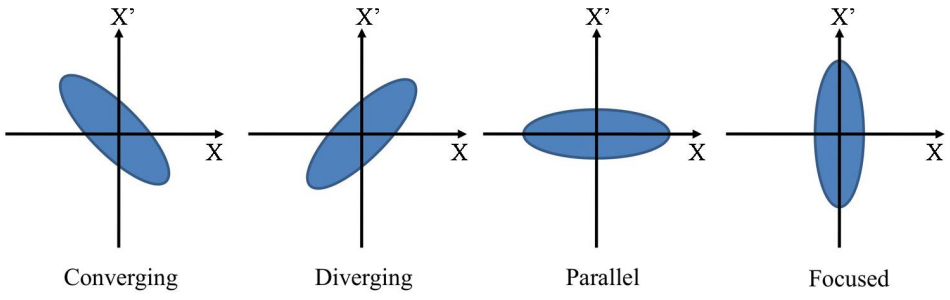

Figure 3.2: The different emittance ellipse orientations for converging, diverging, parallel, and focused ion beams.

3.1.3 Ion Extraction Simulation

As mentioned previously, the transport of the beam is highly dependent on the plasma density, extraction voltage, extraction gap distance, and electrode shape. In chapter 2 the plasma density was found, and from that, we use computer simulations to design and optimize the acceleration column design. The key is to design the extraction system such that the plasma meniscus shape is well matched for parallel beam extraction. If the plasma meniscus is too concave or convex, then the beam will not be well confined, and for the case of API, it is important to keep the beam spot small at the target. In order to get the plasma meniscus right, the electrode shape and geometry, along with the applied voltages, must be properly matched to the plasma density.

The program IGUN is an ion extraction and transport code for simulating positive ion extraction from a plasma. It is a two dimensional code which calculates and plots the ion trajectories, equipotential lines, and plasma meniscus for axi-symmetric and rectangular extraction geometries. The user defines the geometry and voltage of the electrodes and the plasma parameters such as ion and electron temperature, ion mass, charge state, and ion density [50].

The shape of the boundary layer is determined through an iterative process; the electric field strength is compared to the field strength of the sheath. The ions leaving the plasma sheath are first accelerated by the static potential distribution among the electrodes. The following cycles allow beam space charge effects to change the potential distribution until a convergence is found. The beam space charge not only changes the final trajectories of the beam but also the meniscus shape.

3.2 Ion Optics for API Neutron Generator

In order to achieve an acceptable x-y resolution in API imaging, the ion beam spot diameter must be kept small such that the calculated neutron trajectories from the alpha detection are accurate. For the neutron generator discussed in this paper a beam spot diameter of 1-mm is desired, which provides a good balance between imaging resolution and neutron yield. As mentioned previously, the theoretical neutron yield needed from this generator is between 10^7 to 10^8 n/s, and without water cooling, it is imperative to keep the target surface cool at the beam location such that the implanted and adsorbed deuterium and tritium atoms do not diffuse out of a hot surface. IGUN simulations of the first optics design predict that a 1.1-mm spot size on the target can be achieved using a 0.8-mm aperture, a beam energy of 60 keV, and a current density of 7 mA/cm^2. The calculated beam trajectories and beam profile at the target are provided in Fig. 3.3 and Fig. 3.4.

A zoomed-in look at the plasma meniscus can also be seen in Fig. 3.5. Previously it was expected that the current density must be > 20 mA/cm^2 in order to get a good atomic ion fraction, so the fact that we can now operate at such a low current density and still have

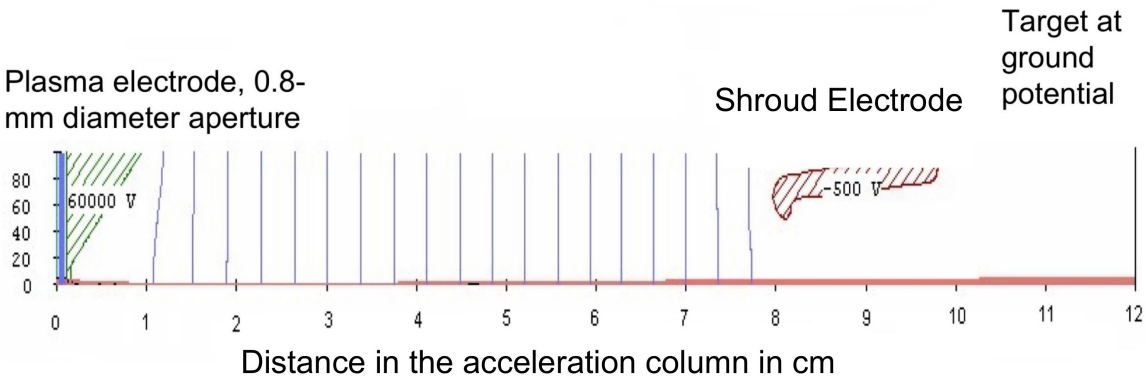

Figure 3.3: IGUN simulation of the hydrogen ion beam trajectories. The simulation was done assuming a 60 kV bias on the plasma electrode, a -500 volt on the shroud/electron suppression electrode, and the target at ground. The extraction aperture opening was 0.8-mm in diameter and the current that reached the target was 36 μA. The target is at a distance 12 cm away from the extraction aperture.

good atomic ion fraction is good news for designing ion optics that can focus a 20 - 40 μA ion beam to a small spot size on the target.

The electron suppression (shroud) electrode is made from stainless steel; it has a total length of 10 inches. The electrode comes through the insulator with a 0.75 inch diameter, and expands to a detachable 3-piece column, with a cylinder 1.8 inches long and 1.2 inches diameter sandwiched between 2 semi-spheres 1.2 inches in diameter, with the beam facing sphere having a 6-mm hole drilled into the center for the ion beam to pass through. The cylinder body also has a slot cut in it to expose the target so that the associated alpha particles from the neutron producing reactions can pass through; the slot is 0.625 inches long and 0.25 inches wide. A photograph of it from the side and front can be seen in Fig. 3.6 and Fig. 3.7, respectively.

3.2.1 Target Biasing

The reason a negative biased target was chosen over a grounded target is that a grounded target would require the source to be at high voltage. This would require a large isolation transformer in the matching box to isolate the high voltage from the RF power supply which is at ground. The transformer would add more bulk and weight to the matching network, making it less appealing for portable field operations. With the target biased at negative high voltage, only one power supply would be needed to provide the negative high voltage on the target and the shroud, or electron suppression electrode which surrounds the target and has a slot cut out facing the target for the associated particles to pass through to the detector.

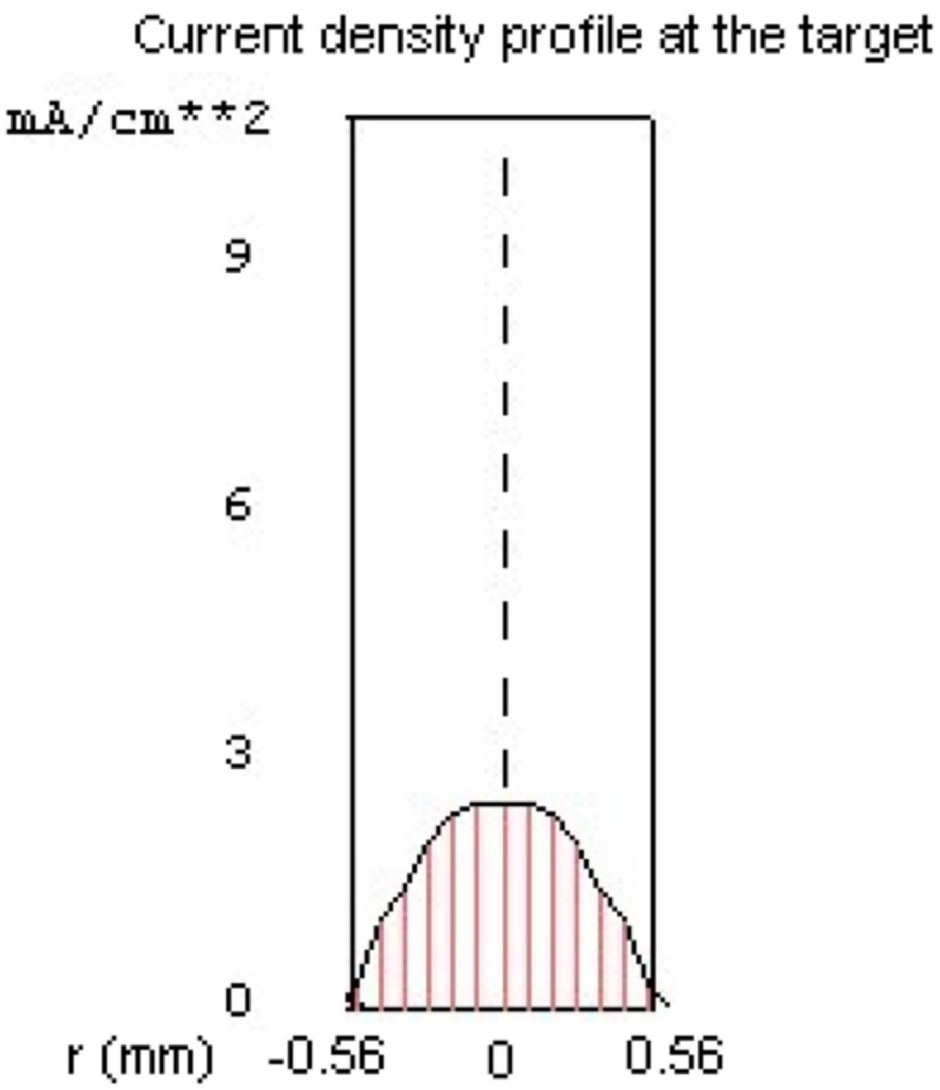

Figure 3.4: IGUN simulation of the beam profile at the Ti target 12-cm away from the extraction aperture. The profile was obtained with the same conditions in the ion beam trajectory simulation. The overall ion beam diameter at the target is around 1.2-mm.

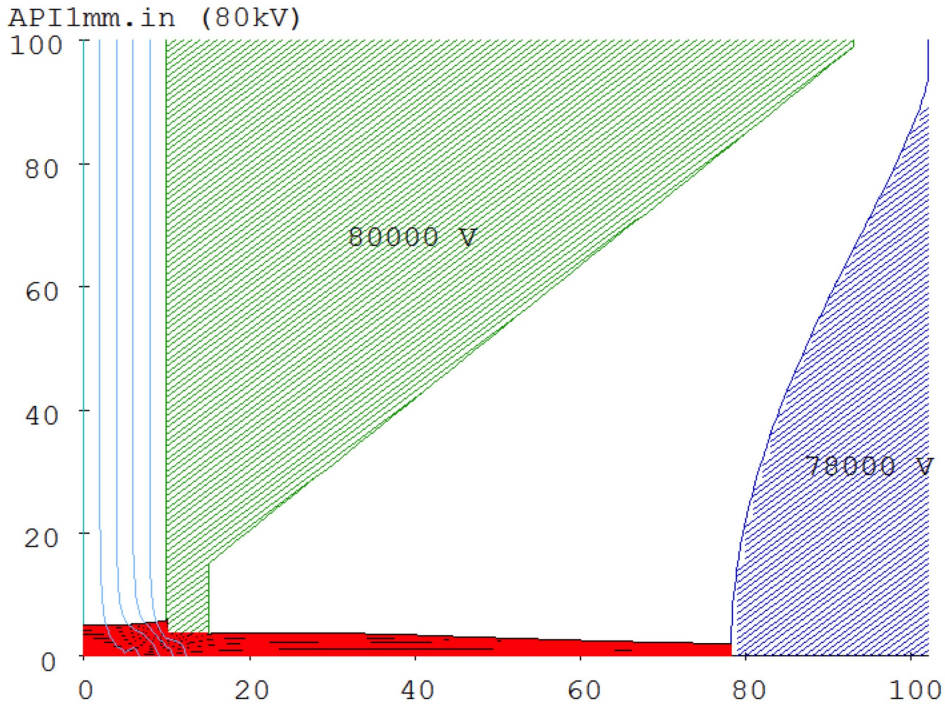

Figure 3.5: An enhanced look at the plasma meniscus for the API neutron generator shows that the meniscus is flat near the extraction aperture. This also shows the beam being focused as it travels down towards the target.

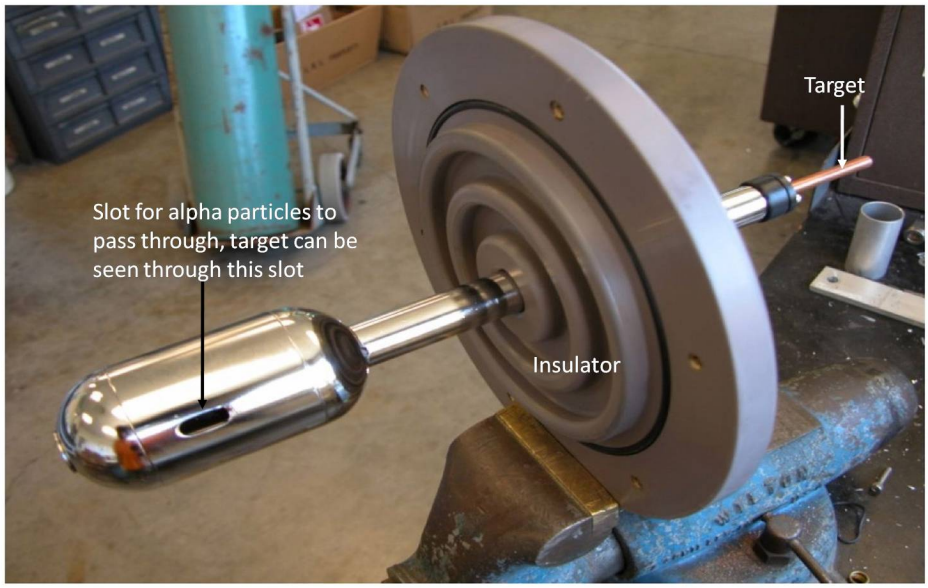

Figure 3.6: Up close photograph of the electron suppression electrode and target outside of the neutron generator chamber body. The end of the target can be seen sticking out, the beam facing side is inside the electron suppression electrode. The insulator is an inch thick PVC with grooves machined in.

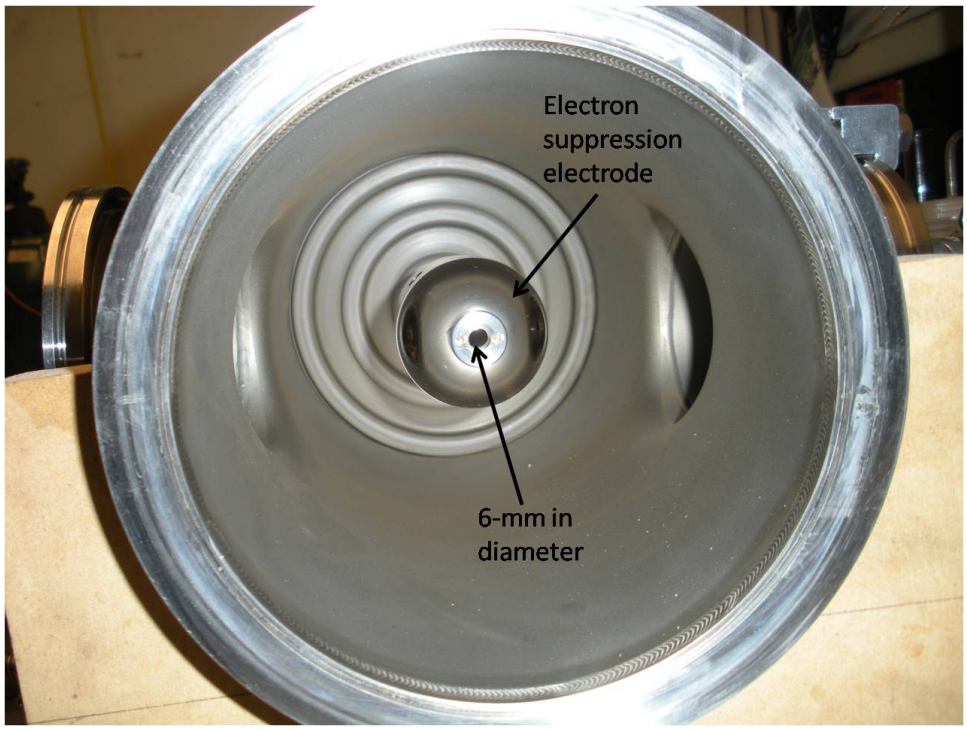

Figure 3.7: A photograph of the electron suppression electron as it sits in the neutron generator body. The view of the electrode is from the front flange opening where the ion source is attached.

The biased shroud-electrode is used to prevent the secondary electrons from back-streaming from the target. The biasing is achieved using a set of 7 Microsemi IN3015RB Zener diodes in series to bias the target 1400 volts more positive compared to the shroud electrode. Each Zener diode has a Zener voltage of 200 volts and is reverse biased from the anode to stud. When the high voltage is turned on, the Zener diodes conduct when the voltage reaches the diode's reverse breakdown voltage. Each diode acts like a voltage regulator and provides a constant voltage drop between the shroud electrode and target provided that the current flowing through the diode is enough to keep it in reverse breakdown. A 200 MΩ tiger tail high power resistor is used to connect the target to ground so that there is always a small current (up to 0.4 mA at 80 kV) flowing through the circuit and the voltage drop is always at the Zener voltage. This ensures that the backstreaming electrons see a more negative potential when they travel towards the source and get repelled back to the target. A picture of the Zener diodes can be seen in Fig. 3.8, and a circuit schematic of the biasing of the target and shroud electrode can be seen in figure 3.9. The ion current on the target is measured through the current meter on the HV power supply and subtracted by the current calculated from the applied voltage divided by 200 MΩ, which is always present when the high voltage is on whether or not the beam is on.

3.3 Beam Spot Measurement

The beam spot was also measured optically using a Nikon digital camera. The set up can be seen in Fig. 3.10. The camera was focused on the target, and the resultant photographs of the beam spot on the target at different target biases can be seen in Fig. 3.11. The ion source was held at a constant power of 125 W and a pressure of 12.5 mTorr.

The program ImageJ was used to analyze the photographs taken, and based on the brightness intensity of the photographs, a 3-D profile of the beam spot can be reconstructed. A 3-D profile of the beam at 60 kV can be seen in Fig. 3.12. The profile can also be transcribed into a text file which shows the brightness number at each position in space. From this, a 2-D profile of the beam spot showing the FWHM can be plotted, and it is shown in Fig. 3.13.

Using ImageJ, the reconstructed profiles show a good match to the beam spot size measured from the photographs. This experiment was repeated at different extraction voltages using the same ion source conditions of 125 W and 12.5 mTorr, and the measured beam spot size is shown in Fig. 3.14. This again reinforces the concept of matching the plasma meniscus as at lower voltages the beam is un-focused and as the meniscus becomes more matched to the extraction electric field the beam spot gets smaller and smaller.

As seen from the photographs, the beam spot size decreases with increasing bias voltage on the target. The reason is that the electric field strength is better matched to the plasma meniscus at higher voltages. At lower voltages the plasma is over-dense and the meniscus is

Figure 3.8: Photograph of the Zener diodes. Each diode is capable of providing 200 volts and can dissipate 10 W of power. A 200 MΩ resistor is connected to ground to ensure there is always current flowing through the diodes.

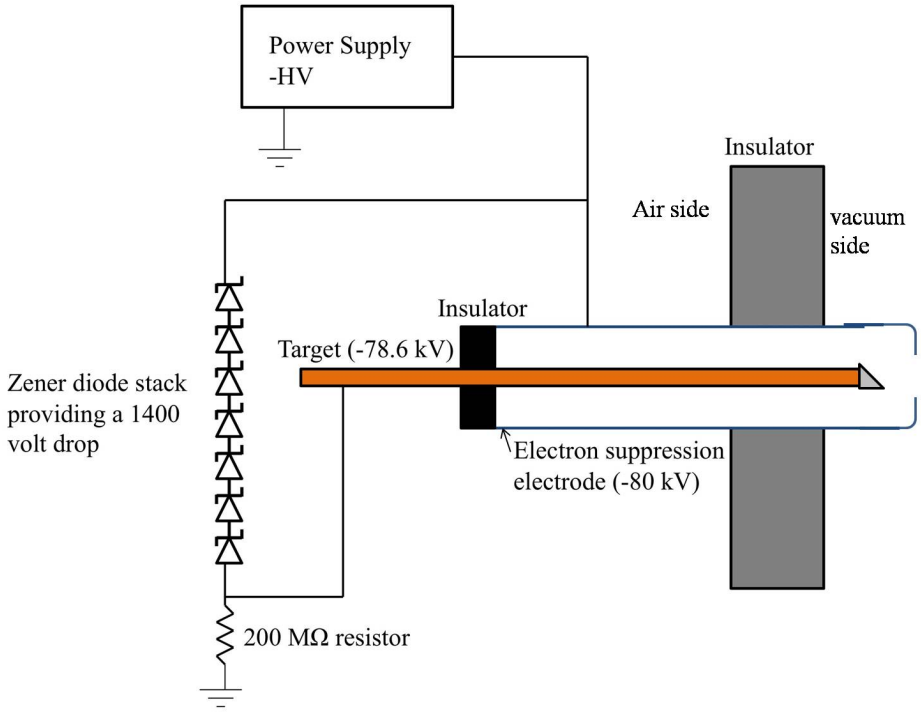

Figure 3.9: Circuit diagram of the biasing of the shroud electrode and target. The Zener diodes provides a 1400 volt drop between the shroud and the target. The 200 MΩ resistor ensures that there is always some current flowing whether or not there is an ion beam hitting the target.

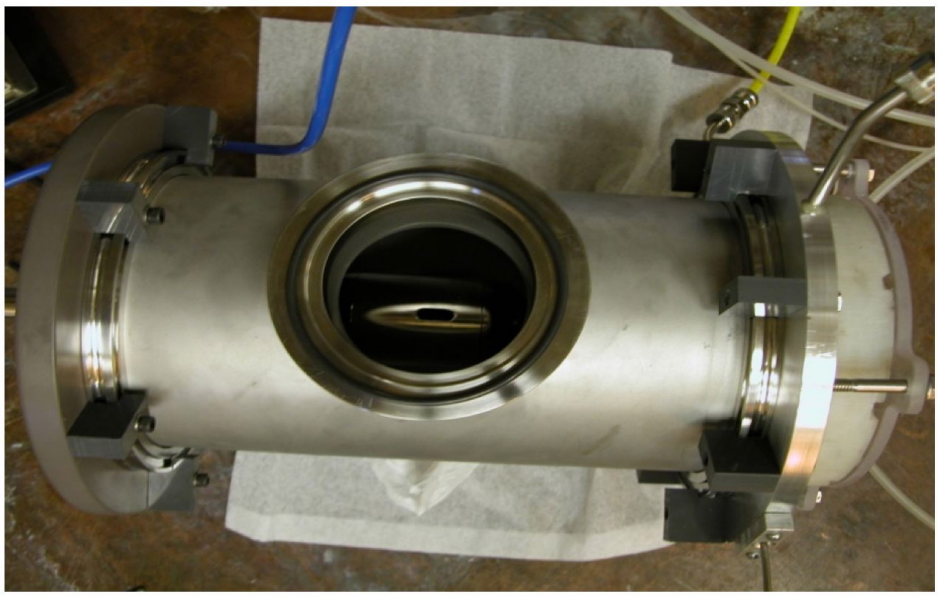

Figure 3.10: Photograph of the electron suppression electrode with the slit cut out to expose the target. A camera was placed just outside the vacuum window to take photographs of the beam spot on the target. A charged particle detector was placed on that same flange in subsequent experiments to measure the associated particles from the D-D reaction.

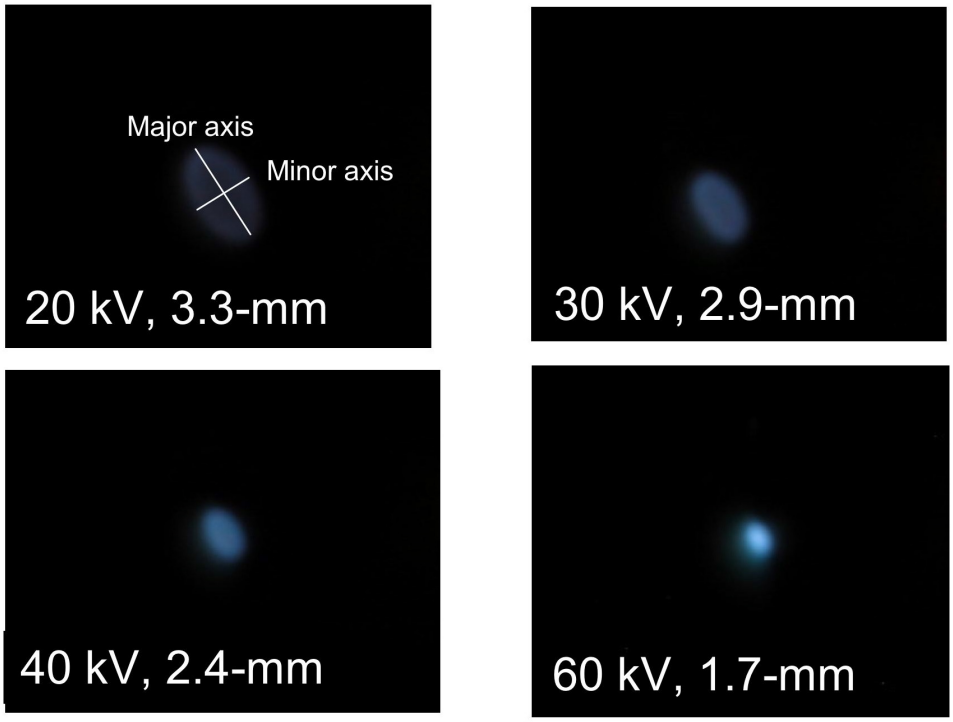

Figure 3.11: Photographs of the the beam spot size decreasing as the acceleration voltage is increased. As the voltage increases the beam spot becomes smaller due to better matching of the electric field to the plasma meniscus and the beam becomes more parallel.

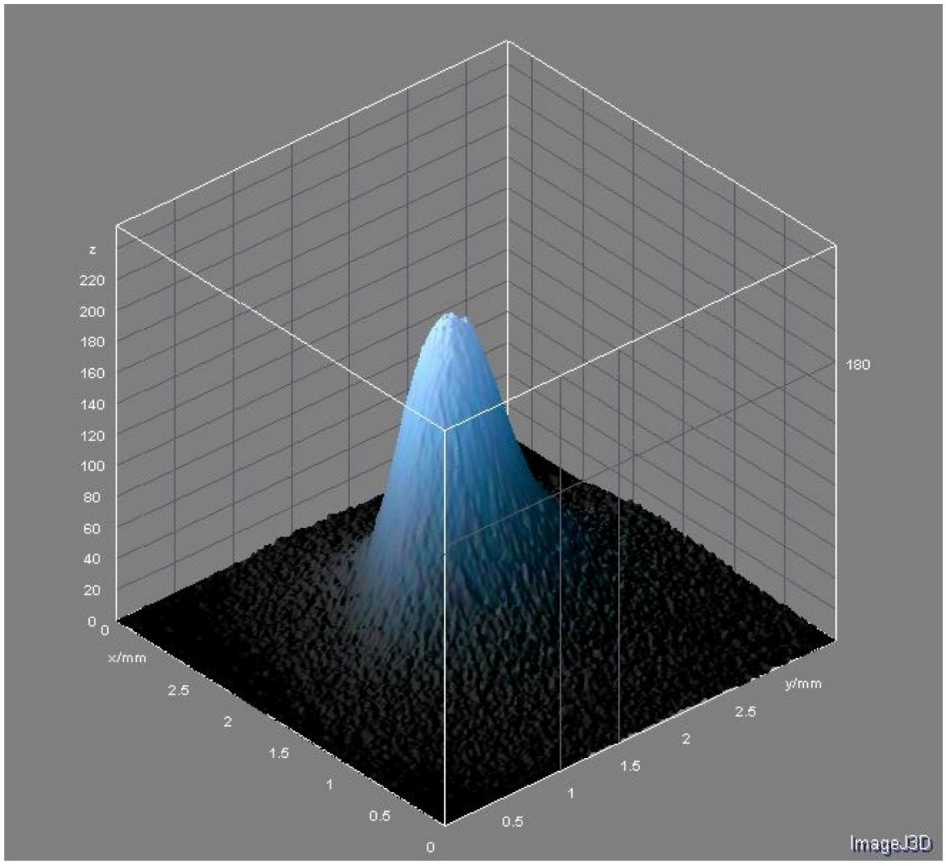

Figure 3.12: A 3-D reconstruction of the beam profile from the photograph of the beam spot taken using the extraction electrode with no ion collimation channel at 60 kV and 120 W of RF power.

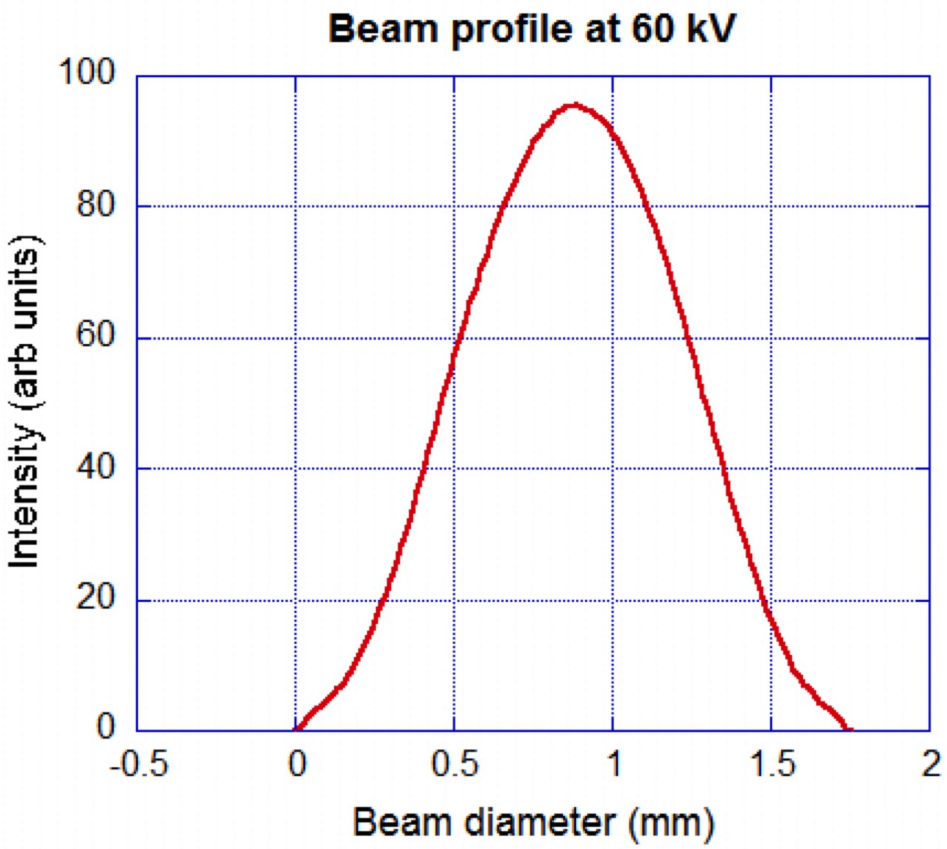

Figure 3.13: The reconstructed 2-D profile of the beam spot at 60 kV using an extraction electrode with an 1-mm diameter extraction aperture with a very small thickness.

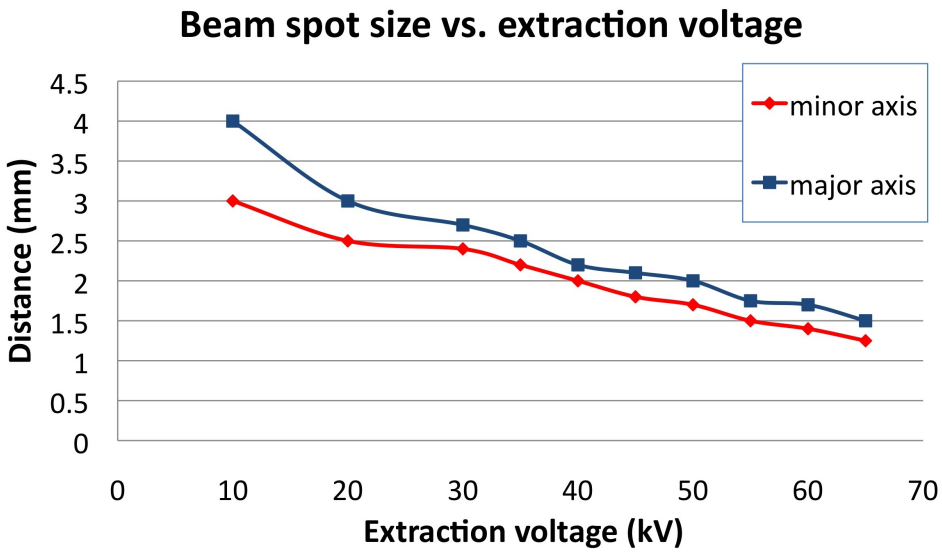

Figure 3.14: A plot of the experimental ion spot size as a function of extraction voltage for a constant source pressure of 12 mTorr of hydrogen and a RF power of 120 W. The major and minor axis are shown because the beam spot is elliptical in shape due to the target being at 45 degrees with respect to the ion beam.

convex shaped, thus increasing the size of the beam spot.

3.3.1 Plasma Electrode Aperture Shape

The shaping of the plasma electrode plays an important part in the beam diameter. Ideally, if the ion trajectories was perfectly parallel, the beam spot and aperture size would both be 1-mm in diameter. However, due to initial ion energy spread, the ions do not come out perfectly parallel. There are separated beams which originate from the perimeter of the aperture. One way to reduce the number of stray ions is to increase the thickness of the extraction aperture, resulting in an ion collimation channel. Instead of having the aperture machined with a very small thickness, as shown by the first example of Fig. 3.15, the aperture can be made thicker. The aspect ratio of the aperture is the thickness of the aperture the beam passes through to the diameter of the aperture itself.

Fig. 3.16 shows the dimensions of the extraction aperture, where a is the extraction aperture diameter and d is the extraction channel length. For the experiments performed, aspect ratios of 1:1, 2:1, 4:1, and 8:1 were used. Fig. 3.15 shows a schematic of the different extraction apertures used. The idea behind using a thicker aperture is two fold. One, as the aperture thickness increases, only the ions with straight trajectories will make it out of the aperture, as the off-axis ions will be lost to the walls of the aperture. Secondly, the total beam current on the target will be reduced, due to the loss of ions as it travels through the aperture. This may seem to be a problem at first since a lower target current means a lower neutron yield. However, since the beam spot on the target needs to be $<$ 1-mm in diameter, a lower current can actually help since the power density will be lower and help keep the titanium target cool. If the low current leads to lower neutron yields, the RF power can be increased to raise the current density as well as improving the atomic ion fraction.

3.3.2 Measuring the beam spot via sputtering

In order to verify the beam spot size and profile taken from the digital photographs, an undoped silicon wafer was cut into small 1-cm by 1-cm squares and affixed to the target via double sided copper tape. The silicon die was then sputtered by a hydrogen ion beam from the ion source at an energy of 60 kV for one hour with the four different extraction aperture aspect ratios. The ion source pressure and power were held constant for all cases at 10 mT and 125 watts. After the silicon has been exposed and sputtered by the hydrogen beam, it is taken out and taken to the UC Berkeley Microfabrication Lab where an ASIQ profilometer is used to measure the surface profile of the silicon die.

A photograph of the sputtered silicon dies can be see in Fig. 3.17. Depending on the depth of the extraction channel, the amount sputtered away on the silicon is changed. A measurement of a 4-mm deep channel aperture shows a beam spot depth of 0.175 μm with a width of 0.6 mm. A measurement of the normal aperture (with a very thin extraction

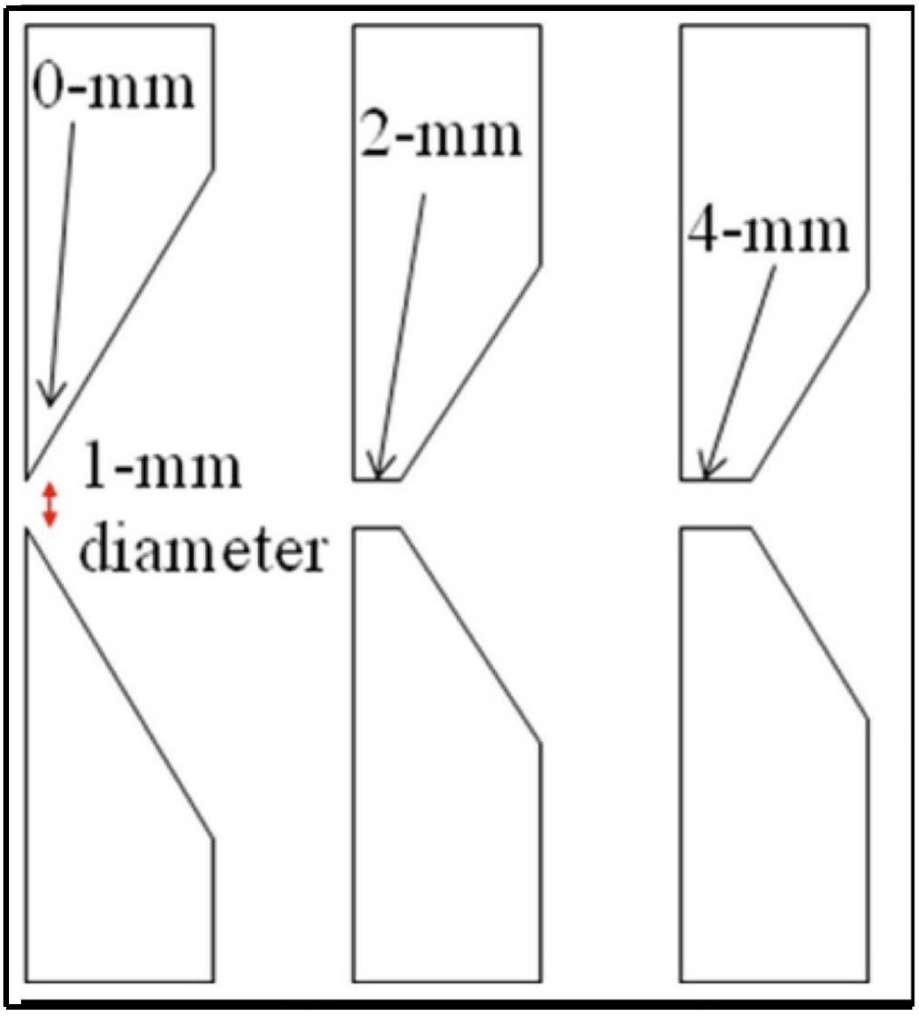

Figure 3.15: Examples of the different extraction electrodes that were machined and tested with varying channel depths. The extraction diameter remained constant at 1-mm for all cases, while the channel depth varied between 0 to 8 mm (8-mm channel not shown in figure).

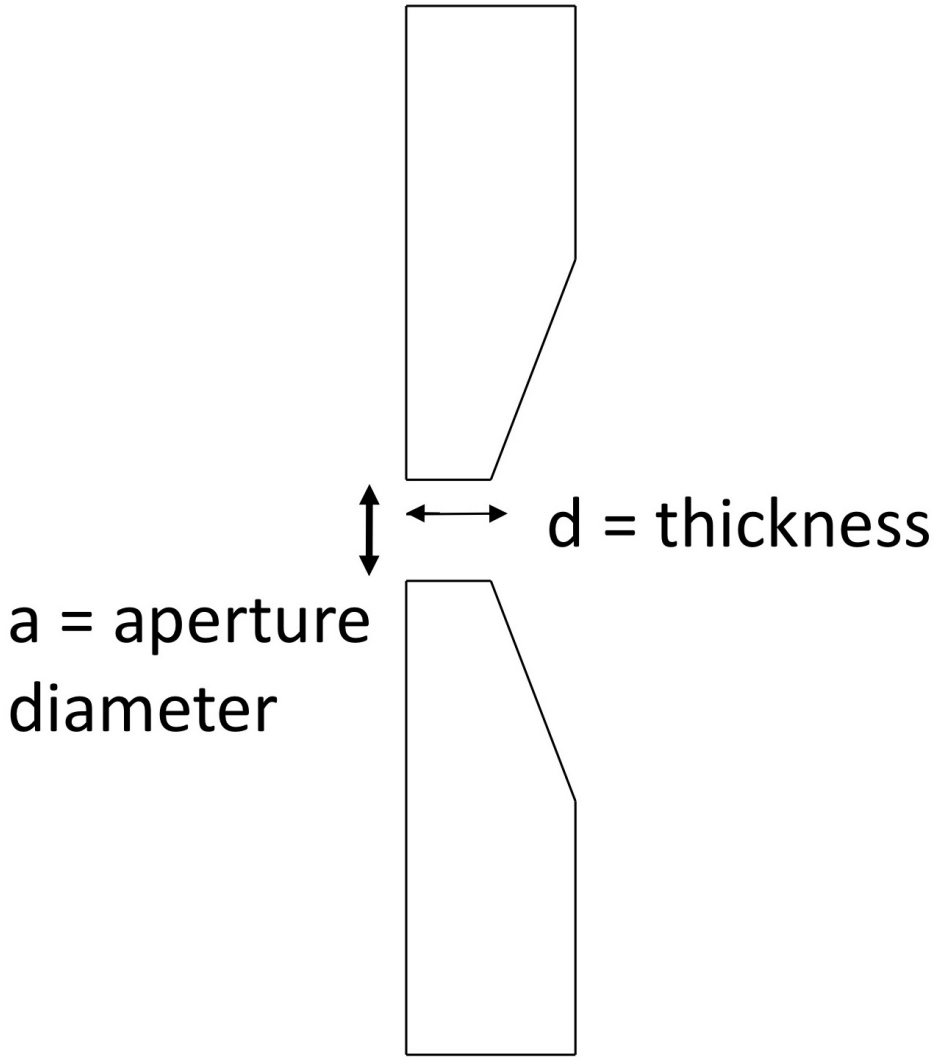

Figure 3.16: Diagram of the extraction electrode shape. The electrode is made from aluminum, and the plasma facing side is flat and smooth with a 1-mm hole drilled through, this diameter is labeled as a. The ion collimation/extraction channel length d can be varied, but the angle of the extraction opening remains constant at 67.5 degrees, the Pierce angle .

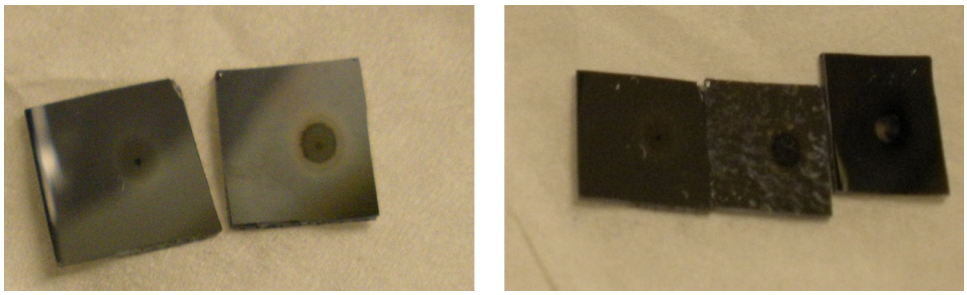

Figure 3.17: The photographs of the silicon dies after they have been sputtered by the hydrogen beam, a small spot can be seen where the beam was incident on the silicon.

channel) shows a beam spot depth of 2 μm and a width of 2 mm. These profiles can be seen in Fig. 3.18 and Fig. 3.19. The actual profiles measured from the profilometer are inverted in the Y-direction; by inverting the profile, it can also be seen as the beam intensity profile, as the sputtering yield is directly related to the beam intensity.

As was expected, the beam current and the beam spot size both decreased when the ion extraction channel on the plasma electrode was increased, as can be seen in Fig. 3.20. The reason for this is that the longer extraction channel will eliminate those ions with higher transverse energies that have a higher angular spread. By extending the ion extraction channel, those ions will be lost to the inner wall of the channel, and thus the total current extracted will be reduced. The beam spot size will also be reduced since the total transverse energy and angular spread of the ions exiting the extraction channel will be smaller as well. The optimal channel length is around 1 to 2 mm in length, where the beam spot diameter is close to 1 mm and the total current on target is above 20 μA, which is the minimum current needed to reach a neutron yield of 10^7 n/s.

3.4 Conclusion

The ion beam spot size and ion current at the target have been measured for varying ion extraction aperture thicknesses, both optically and physically. The aperture thickness was varied between 0 and 8 mm to examine its effects on ion current and ion beam spot size on the target. A thicker aperture will help to collimate the beam and reduce the beam spot size as well as reducing the beam current on target. To counter the loss in beam current, the RF power can be increased. Increasing the RF power will also increase the atomic ion fraction in the plasma.

The ion beam spot size was measured by taking optical images of the beam spot on target using a 18x optical zoom digital camera through a slit in the electron suppression electrode, at the location of the photomultiplier tube and scintillator. Measurements for

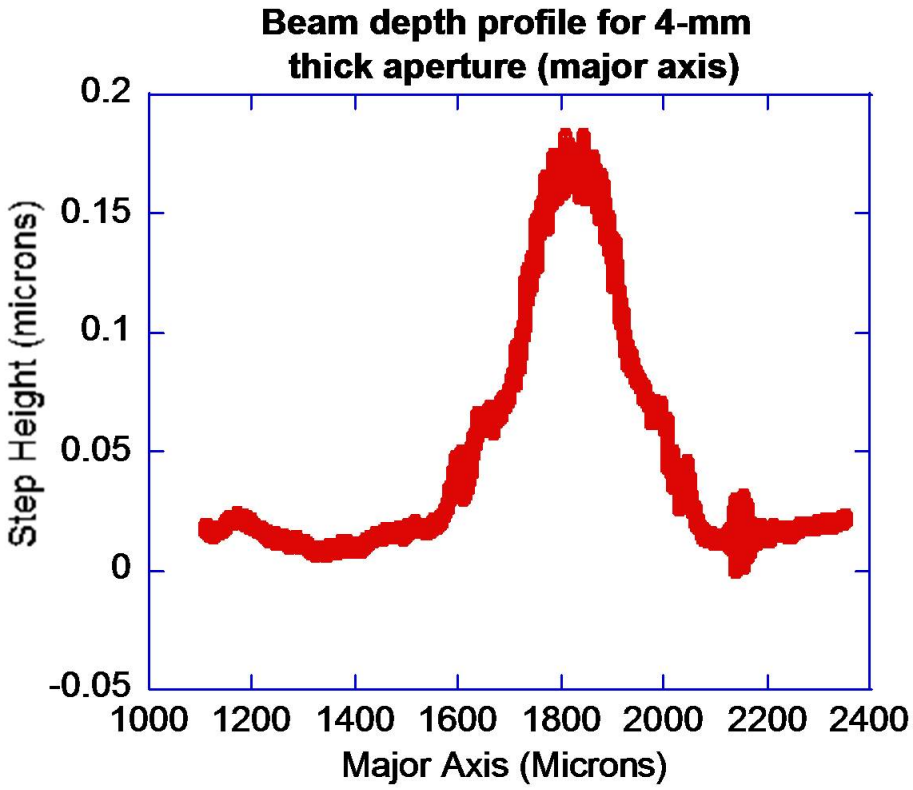

Figure 3.18: The inverted profile from the ASIQ profilometer scan of the silicon die sputtered using the 4-mm deep channel extraction aperture. The profile is roughly 0.5 mm in diameter.

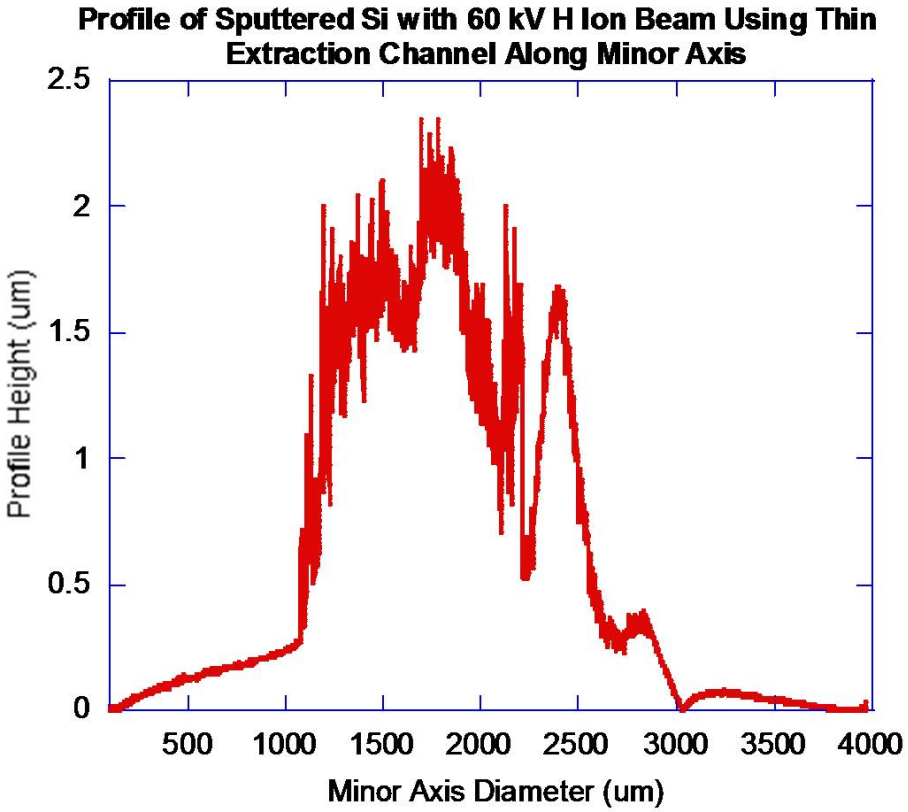

Figure 3.19: The inverted profile from the ASIQ profilometer scan of the silicon die sputtered using the very thin "0-mm" thick channel extraction aperture. The profile is roughly 2 mm in diameter.

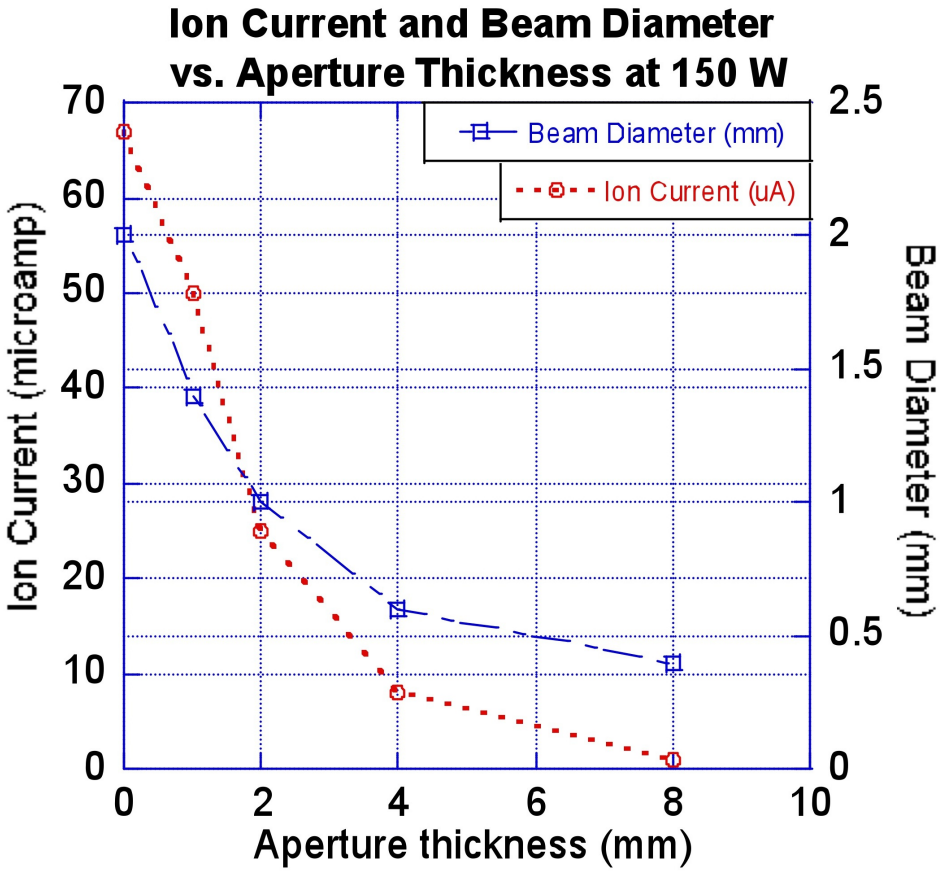

Figure 3.20: The photographs of the silicon dies after they have been sputtered by the hydrogen beam, a small spot can be seen where the beam was incident on the silicon.

an aperture thickness of 0-mm showed a near Gaussian beam profile with a FWHM and a beam diameter of 1.5 mm. To confirm the optical measurements, silicon squares (1-cm x 1-cm) were affixed to the target and bombarded with a H^+ ion beam at 60 kV for varying apertures and constant pressure and power. The intensity profile was measured using an ASIQ profilometer (with 5 $\mathring{A}$ resolution) that calibrated the sputtered profile on the silicon chips. The measured Gaussian profiles were in agreement with the optical images. Also, for a 2 mm thick aperture, the beam spot size and FWHM was 1-mm. The ion beam current was measured simultaneously using a current meter connected to the HV supply.

Chapter 4

Sealed Neutron Generator Design and Results

4.1 Prototype Sealed Neutron Generator for API

*A prototype neutron generator was designed and built for sealed operation based on the RF ion source and acceleration column testing results described in the previous chapters. The requirements of this neutron generator are to produce 10^7 n/s to 10^8 n/s via the deuterium-tritium fusion reaction, require no external water cooling, and can operate without constant pumping. These features are advantageous for active neutron interrogation where mobility and size are major issues. The operating parameters for this neutron generator are as follows: RF power = 150 Watts, acceleration voltage = 75 kV, acceleration column pressure = 4.5 mTorr. The initial results presented were performed using deuterium as the feed gas, since the safety requirements for testing with tritium are much more stringent. The expected cross-section for the D-D fusion reaction is more than 100 times lower than that of the D-T reaction [53]. The D-T neutron yield can be estimated by scaling up from the D-D neutron yield. The neutron yield under several conditions will be discussed, as well as the results from a charged particle detector of the associated particles from the D-D reaction.

4.1.1 Design Parameters of the Prototype Neutron Generator

This work will focus on the requirements and development of compact neutron generators to be used for the method of API. The first generator requirement for this method is a neutron yield in the range of 10^7 to 10^8 n/s with D-T, (10^5 to 10^6 n/s with D-D) which is important for high signal-to-noise ratios and the accurate detection of small amounts of

*Reprinted with permission from Y. Wu, *et. al*, Rev. Sci. Instrum., Proceedings of the International Conference on Ion Sources (ICIS 09). Copyright 2010, American Institute of Physics.

sensitive materials. To obtain these neutron yields, the ion current required is between 20 to 80 μA at an acceleration voltage of 80 kV with an atomic ion fraction of at least 80%, and an ion source extraction aperture of 1-mm in diameter is needed. This plasma current density of 3 to 9 mA/cm^2 requires an RF power of 100 to 150 Watts. Previous chapters on the ion source work have shown that a high atomic deuterium ion fraction can be achieved with only 100 W of input RF power with both 13.56 and 27.12 MHz frequencies. Additionally, the pressure in the acceleration column must be kept low to prevent voltage break down at ion acceleration voltages of 80 kV, which requires a low operating pressure at the source. An engineering drawing of a concept API neutron generator with a negatively biased target is shown in Fig. 4.1 [54].

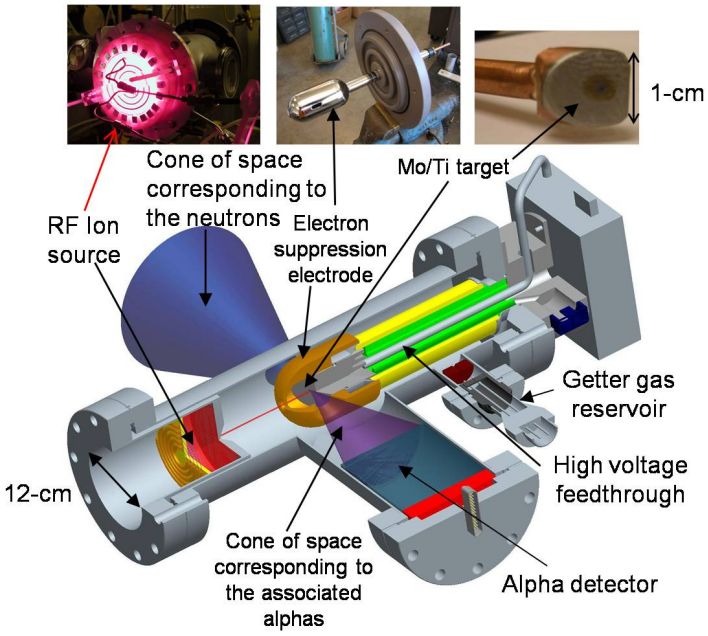

Figure 4.1: Engineering drawing of the API neutron generator. The plasma is produced by a planar RF-driven antenna at 13.56 MHz and the ion beam is extracted from the plasma electrode at ground potential and accelerated through the shroud electrode biased at -80 kV and to a titanium target biased at -78 kV. There is a hole on the side of the shroud electrode for the alpha particles to pass through and reach the alpha detector, and the blue cone opposite the alpha detector is the region of space which can be used for neutron scanning and imaging.

4.2 Neutron Generator Set-up

The RF-driven ion source consists of a half closed quartz cylinder (12 cm in diameter and 3.5 cm in depth) sealed to an aluminum electrode with a spiral copper antenna (3.5 turns) attached to the back. Surrounding the quartz in the radial direction are 20 multi-cusp magnets, used to improve the plasma density and operating pressure by confining the electrons and reducing losses to the walls. Compressed air is passed through the matching network and antenna for cooling, and a fan provides air-cooling for the source body and electrode. RF power is inductively coupled from the antenna to the plasma, creating an intense ion source. The ions are extracted through a 1-mm diameter aperture and accelerated on to the generator target at energies of up to 80 keV. The body of the neutron generator is a stainless steel vacuum cross bought from MDC with the diameters of the large flanges at 7 inches in diameter, and the smaller flanges 4.25 inches in diameter. The cross is 10.5 inches in length in both directions. One opening is attached to the plasma electrode and ion source, and opposite that end the high voltage insulator and target/electron suppression electrode is attached. On the other two flanges a charged particle detector and a valve which allows the unit to be pumped by the turbo and mechanical pumps are attached. The high voltage insulator is a 5/8 inch thick chlorinated PVC 12 inches in diameter. Fig. 4.2 and Fig. 4.3 shows a schematic and a photograph, respectively, of the prototype API neutron generator.

The generator target consists of a 1-mm thick titanium layer explosively bonded to a 5-mm thick, 1-cm^2 copper layer that is brazed to a copper rod 1/4 inch in diameter with 1/8 inch hole in the center for cooling (by air). Titanium was chosen as the target material because it has been widely used in the neutron generator industry, mainly because it absorbs hydrogen and its isotope atoms at a Ti:H ratio of 1:2 [55]. The target is enclosed inside an electron suppression electrode. The electron suppression electrode dimensions are described in the previous chapter and the electrode is biased at -75 kV, and is connected to a set of reverse biased Zener diodes which provide a potential drop of 1.4 kV to the target. The target is situated at an angle of 45 degrees with respect to the ion beam such that the target is exposed through a 0.625 inch by 0.25 inch slit in the electron suppression electrode. The slit cut into the shroud electrode enables a view of the target by the charged particle detector (under vacuum) for detection of the associated alpha particles. All experiments performed utilized deuterium gas. A photograph of the target after being loaded with a 75 kV deuterium beam for several hours is shown in Fig. 4.4. The spot size on the target is easily seen, and is around 1-mm in diameter. The extraction channel used had a length of 2-mm in diameter.

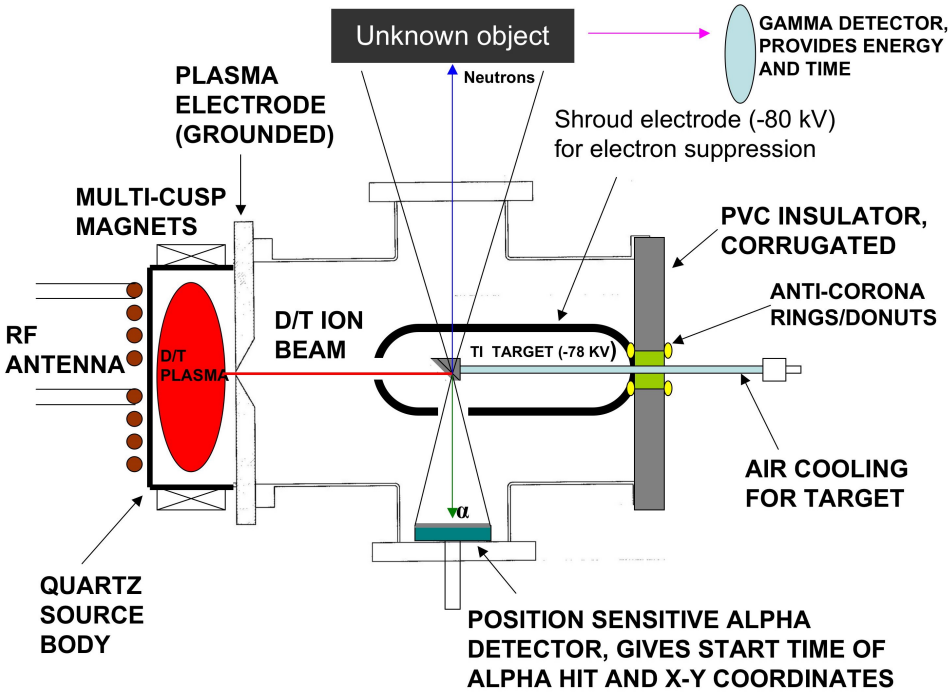

Figure 4.2: Schematic of the prototype neutron generator. The generator is attached to a pumping unit and vacuum chamber. For sealed mode operation, a valve is used to block the vacuum and the needle valve turned down to stop the gas inlet.

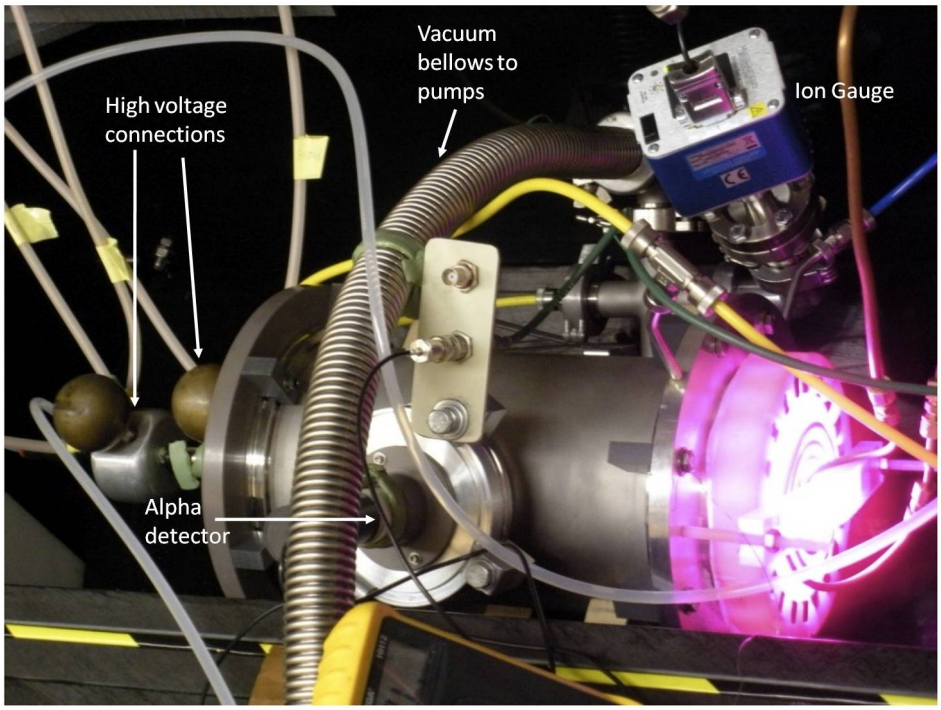

Figure 4.3: Photograph of the prototype neutron generator with the ion source running. The high voltage is attached at the via a couple of anti-corona donuts and spheres. The alpha detector and ion gauge can also be seen in the picture.

Figure 4.4: A photograph of the target up close, the beam spot is the white colored spot on the target in the photograph, some darkened circles can be seen around it from the heat being dissipated on the target.

4.3 Associated Particle Measurements

The D-D fusion reaction branches seen in Eqns. 4.1 and 4.2 show three different detectable charged particles from the reaction. The first is the associated 0.8 MeV He-3 particle from the neutron production reaction, and the others are the 1 MeV tritium particle and the 3 MeV proton from the other reaction branch. The D-T reaction is seen in Eqn. 4.3, where only the associated alpha particle is produced along with the neutron.

$$^2D + {}^2D \rightarrow {}^1n + {}^3He \ (E_n = 2.45MeV, E_{^3He} = 0.82MeV) \tag{4.1}$$

$$^2D + {}^2D \rightarrow T + p \ (E_T = 1.011MeV, E_p = 3.022MeV) \tag{4.2}$$

$$^2D + {}^3T \rightarrow {}^1n + {}^4He \ (E_n = 14MeV, E_{^4He} = 3.5MeV) \tag{4.3}$$

Since API works by measuring the associated alpha particle from the D-T reaction, one can demonstrate that the prototype device is suitable for associated particle detection using the D-D reaction and therefore avoid the use of tritium. The main issue at hand is whether or not having a negatively biased target and shroud would affect the charged particle detector performance since there could be high energy electrons produced from the ion beam interactions with the target, shroud, and background gas that would be accelerated by the electric field towards the detector which is at ground.

Previously at LBNL, experiments using small cylindrical sources were operated at low powers and pressures greater than 40 mTorr inside the chamber [56, 57]. This operating pressure is too high for beam acceleration voltages of 60 kV or greater in a compact neutron generator, due to sparking in the acceleration column that produces high electron current and can damage the scintillator. The pressure must be kept low enough to prevent this discharge or dark current from being produced in the target chamber. This is one of the main challenges for the neutron generator discussed in this dissertation. If the target was grounded, the source would be at high potential and an additional transformer would be required to isolate the RF power supply and matching network, adding more size and weight to the generator system. Thus, the preferred way is to bias the target at negative high voltage. The amount of dark current produced in the acceleration column was measured using two concentric cylinders, 8-cm apart. The center cylinder was biased up to 80 kV for various pressures while the electron current was measured on the outer cylinder as a function of voltage for different pressures (see Fig. 4.5). It can be seen that if the pressure is maintained at or below 10 mTorr, the amount of electron current produced is negligible [31].

A scintillator and photomultiplier tube (PMT) were used to determine the amount of stray photons and electrons generated under the same conditions. The scintillator was a Saint-Gobain BC-408 plastic scintillator, 1-inch in diameter, and 1/4 inch thick. Two scintillators were used, one coated with a 300 nm layer of gold, and one coated with a 500

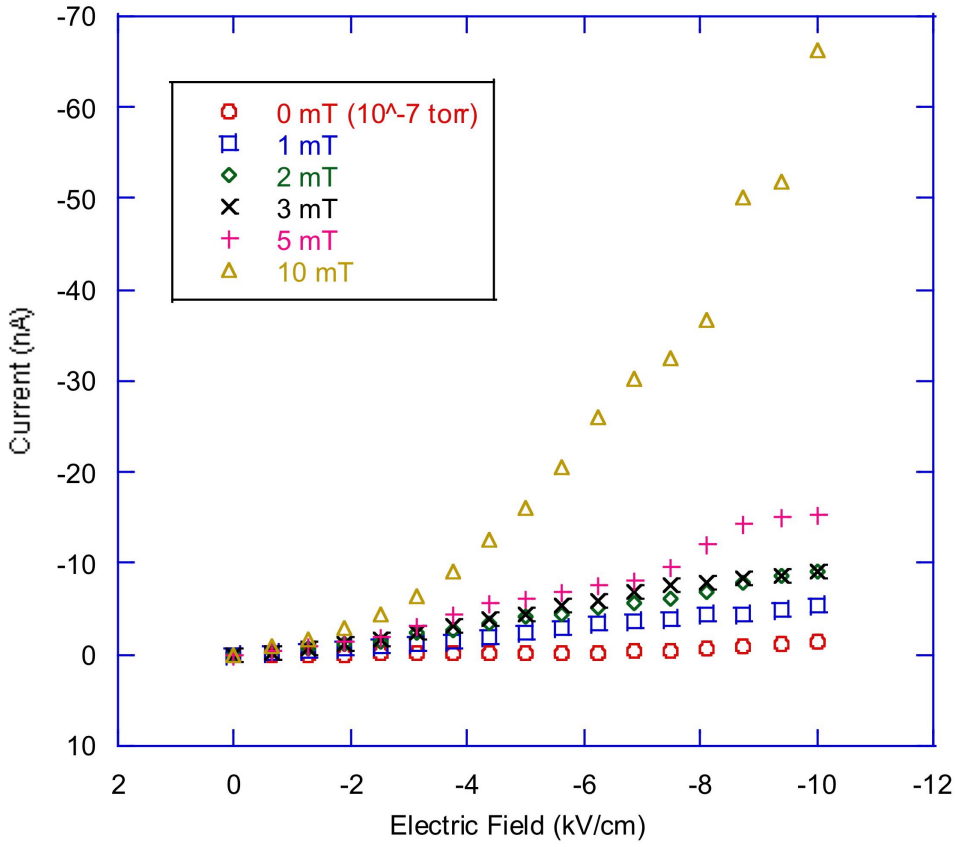

Figure 4.5: Electron current measured as a function of electric field between the shroud electrode and chamber wall, the distance between the two concentric cylinders is 8 cm and the applied voltage on the shroud is adjusted between 0 to 80 kV.

nm layer of aluminum to block any background light from reaching the photomultiplier tube. The photomultiplier tube used was a Hamamatsu R6094, 1-1/8 inch in diameter, biased at -1000 volts. It was discovered that the PMT signal did not change whether or not the scintillator was in place. When a thin opaque plastic cover was placed in front of the PMT, no signal could be seen. This result indicates that most of the signal from the PMT was due to stray light which can be blocked with a thin Al layer on the scintillator. However, since there was still a measurable electron current on the cylinder, the PMT signal must still be tested in the prototype neutron generator.

The scintillator and PMT was attached to one of the side flanges of the body, and the scintillator was placed inside the neutron generator under vacuum. It was affixed to a 1/8 inch thick quartz window with optical cement, and the PMT was placed on the air side, affixed to the quartz window with optical grease. The quartz, scintillator, and PMT are all

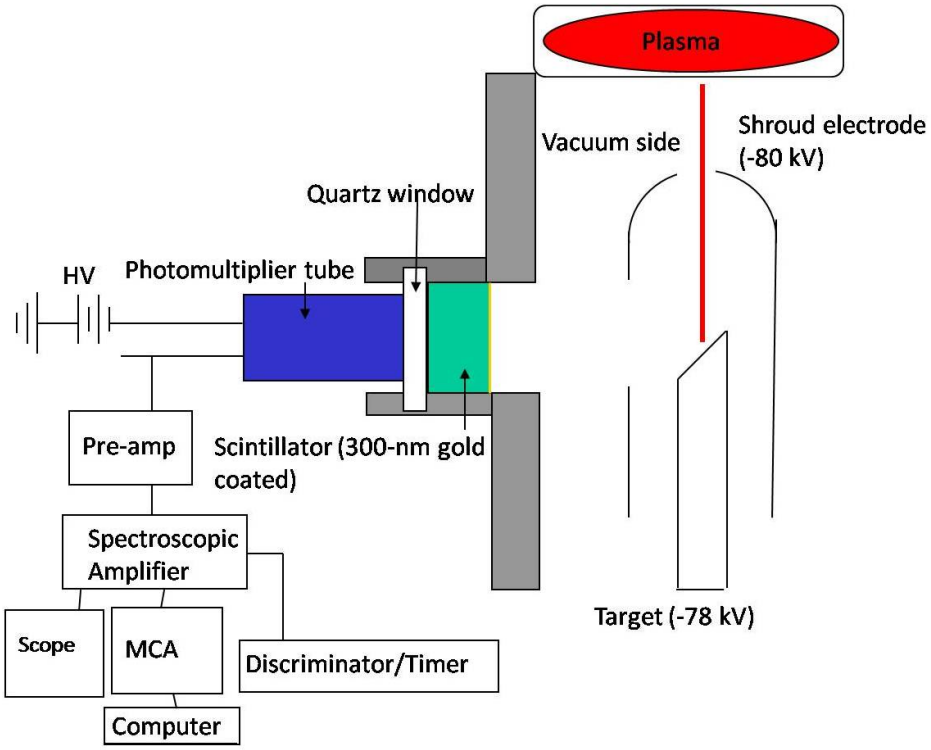

Figure 4.6: Schematic of the scintillator and photo-multiplier tube set up in the neutron generator.

enclosed within an aluminum casing inserted into the cross. A schematic of the set-up can be seen in Fig. 4.6. This setup was used to look for the associated particle signal from the D-D reaction, namely, the 0.8 MeV He-3 particle which is produced along side the 2.45 MeV neutron, and the 3 MeV proton and 1 MeV triton particle in the other reaction branch.

The neutron generator was operated in sealed mode where a valve closed off the neutron generator from pumping. The plasma was first started under differential pumping conditions with the valve open since the ion source needs about 50 mTorr to ignite the plasma. After the plasma has been ignited, the needle valve used to regulate the gas flow and the vacuum valve are closed slowly at the same time so as to maintain constant pressure inside the source. After the pressure has reached an equilibrium between the ion source and the acceleration column, the high voltage is turned on and increased slowly to the electron suppression electrode and target. The RF power to the ion source was 150 W, and the pressure inside the acceleration column was 6 mTorr [52].

When the voltage was increased to 70 kV, the current meter on the high voltage power supply would begin flickering, indicating an electrical breakdown inside the neutron genera-

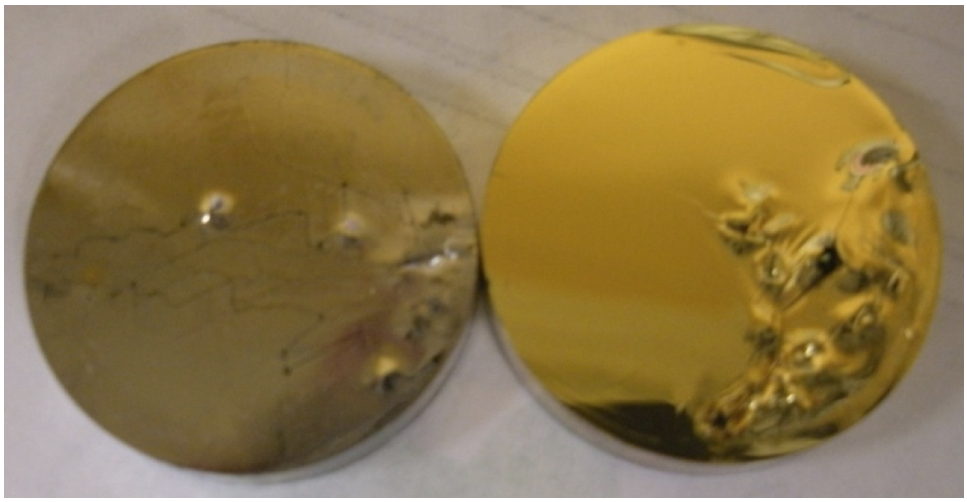

Figure 4.7: Photograph of the gold and aluminum coated scintillators used for alpha particle detection after a spark in the main chamber during sealed operation.

tor. After a few minutes, the pressure inside the acceleration column began to rise, and the current reading on the high voltage power supply increased greatly and the power supply became current limited. This was observed for pressures in the acceleration column above 5 mTorr; at pressures of 4.5 mTorr and below, the neutron generator could operate at 70 kV with no electrical breakdown. However, in order to operate at 4.5 mTorr or lower, the RF power must be increased to 170 W. Unfortunately, due to the electrical breakdown in the acceleration column, the scintillator was damaged before any spectra were measured.

A photograph of the damaged scintillators can be seen in Figs. 4.7 and 4.8. The gold and aluminum coating show cracking and bubble formation. The rise in pressure can be attributed to the sparking causing out-gassing from the scintillator. The color of the scintillators also darkened significantly. The scintillators started off as clear plastic; after they were damaged by the electrical breakdown, the color turned dark brown, and almost black at certain spots.

The gold coated scintillator was used first, and was replaced by an aluminum coated scintillator after it was found that the gold layer had been damaged from the sparks. The aluminum coated scintillator was damaged in the same manner and can also be seen in the above figure. Previous work has shown that a negatively biased target would not cause breakdown under 10 mTorr operating pressure with no beam. However, at pressures above 5 mTorr in the acceleration column, the system became unstable and voltage breakdown occurred in the discharge region. The film coating on the coated scintillator was damaged by the electrons from the break-down, and caused considerable discoloration of the plastic scintillator. The source can be operated with a deuterium gas fill at pressures as low as 4

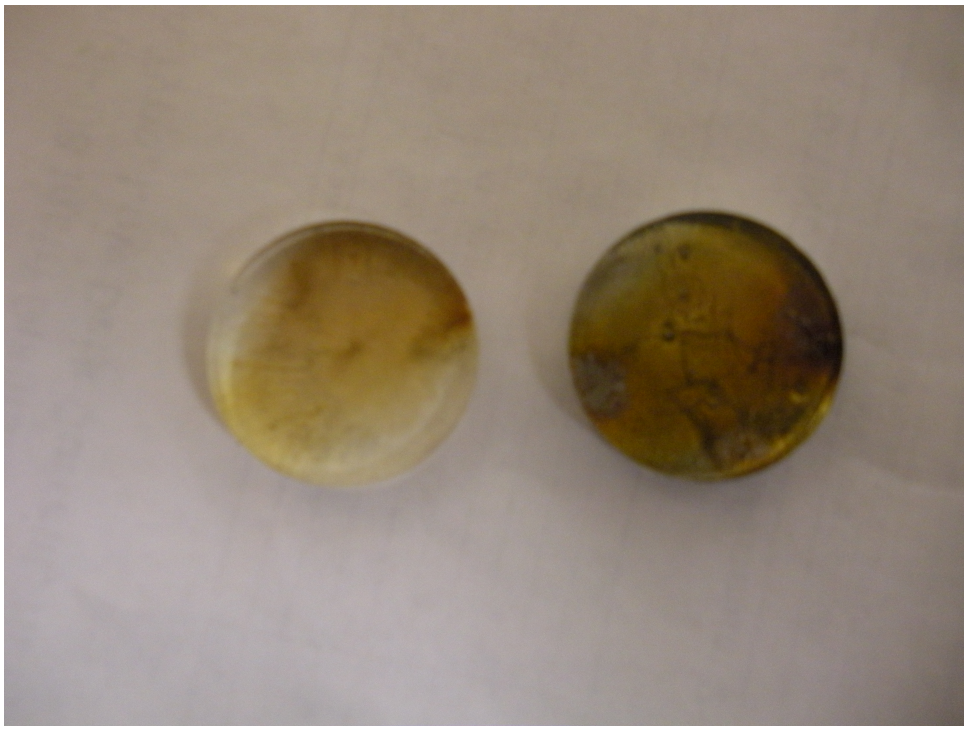

Figure 4.8: Photograph of the backside of the aluminum coated scintillator and a non-metal coated scintillator showing the discoloration of the plastic due to the electrical breakdown.

mTorr and powers of 150 Watts, but instabilities and breakdown may occur. To ensure a stable plasma, the system would require about 200 Watts to operate at pressures of 4 mTorr or below. By increasing the RF frequency to 27.12 MHz it is expected that a lower operating pressure could be used [57]. However, as discussed in chapter 2, using a higher frequency resulted in the plasma being capacitively coupled at lower powers, leading to a lower current density and lower atomic ion fraction in the plasma.

A spectrum of energies was also observed using the scintillator detector at voltages of 70 kV. The D-D neutron reactions shown by Eqns. 4.1 and 4.2 result in the production of three charged particles with varying energies. These three charged particles together with electrons and scattered deuteron ions are all detectable using a scintillator and are expected to result in unique MCA features. However, due to the fact that the spectra were taken after the scintillators had already suffered damage from electrical breakdown, it was difficult to reproduce the results. Even when the conditions were the same, the MCA spectra were different. Therefore a different detector was used. Since the scintillators were damaged during the sealed mode operation, a more rugged detector was necessary to look at the charged particles from the D-D reaction. An Ortec ULTRA ion-implanted silicon charged-particle detector model U-012-025-100 was used in the place of the scintillator and PMT system. It has an active area of 25 mm^2. It was biased at 25 volts, and used with an AMPTEK 8000A Pocket MCA and Canberra 2020 amplifier and Canberra 2020 pre-amp. Fig. 4.9 shows a photograph of the detector sitting in its holder. The detector was first calibrated with an Am-241 source in vacuum using the 5 MeV alpha particle emission, and then used to observe the D-D reaction at 70 kV.

In order to eliminate the background counts, hydrogen was used in place of deuterium and the spectrum from the resulting H-H reaction was subtracted from the spectrum of the D-D reaction. However, the spectra showed a large amount of noise due to electrons coming from the negatively biased electrode and target, and the dead time was over 90%. To confirm the presence of electrons, two different thicknesses of aluminum foil were placed in front of the detector, 12.5 μm thick and 50 μm thick. According to Casino (Monte Carlo simulation of electron trajectory in solid) simulations, the maximum range of 70 keV electrons in aluminum is 33 μm, and for 50 keV electrons the maximum range is 16 μm. This means that at lower energies, the signal from the electrons should be completely blocked by the aluminum foil. Figs. 4.10 and 4.11 show the simulation results for 50 keV and 70 keV electrons in aluminum. Experimental results showed that the aluminum foil was successful in blocking the electrons in both cases, where a spectrum was not seen until the voltage was up to 50 kV for the 12.5 μm thick foil and 65 kV for the 50 μm thick foil.

This proved useful to stopping electrons, but this also hindered the collection of ions. SRIM (Stopping and Range of Ions in Matter) simulations were performed for 1 MeV tritium ions, 3 MeV protons, and 0.8 MeV He-3 ions in aluminum. The results showed that all but the 3 MeV protons would be stopped with a 10 μm thick layer of aluminum. A 3 MeV proton has a range of up to 80 μm in aluminum, which meant that it would be the only

Figure 4.9: A photograph of the charged particle detector.

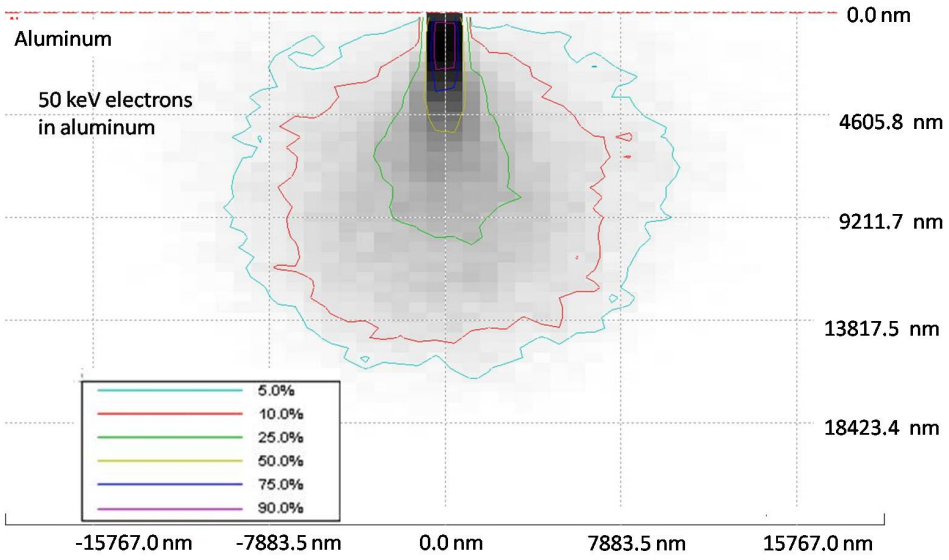

Figure 4.10: CASINO simulation of 50 keV electron distribution in aluminum, the different colors lines reflect the percent of electrons that are outside the lines.

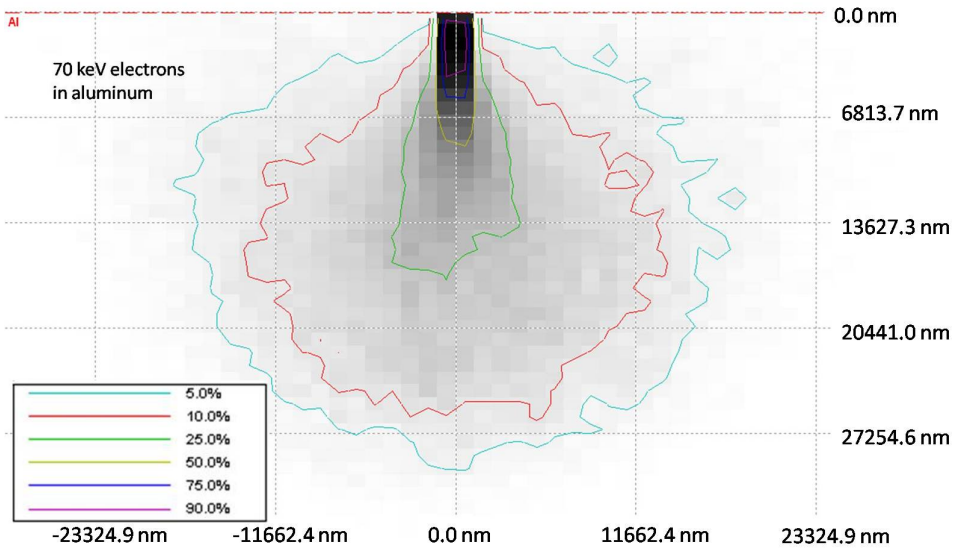

Figure 4.11: CASINO simulation of 70 keV electron distribution in aluminum, the different colors lines reflect the percent of electrons that are outside the lines

particle detectable when a foil is used. Fig. 4.12 shows the charged particle detector with an aluminum foil in front of it.

Figure 4.12: A photograph of the charged particle detector with a thin foil in front of it.

Three different sets of data were collected by the detector, and the MCA spectra were analyzed. The RF power used in the ion source was 150 W for all cases, and the acceleration voltage was 70 kV. The first set is the data from the detector with no foil in front of it, after the H-H plasma spectrum had been subtracted from the D-D spectrum. The second set is the same experiment repeated with a 12.5 μm thick aluminum foil in front of the detector, and the third set the spectra collected with a 50 μm thick aluminum foil in front of the detector. The resultant spectra and the Am-241 spectrum can be seen on Fig. 4.13

From looking at the spectra, one can see that for the spectrum taken with no foil, there is a peak near both the 1 and 3 MeV range, indicating it could be the tritium and proton peak. The thin foil covered detector spectrum shows a peak near 2 MeV. According to SRIM, transmitted 3 MeV protons through 12.5 μm thick of aluminum should have energies in the range of 1.91 to 2.58 MeV, matching that of the spectrum. The spectrum from the thick 50 μm aluminum foil covered detector shows one peak at around 600 keV, which matches the SRIM simulation which shows the transmitted proton energy to be in the range of 3 keV to 700 keV, with an average energy of 497 keV. This shows that the associated particles

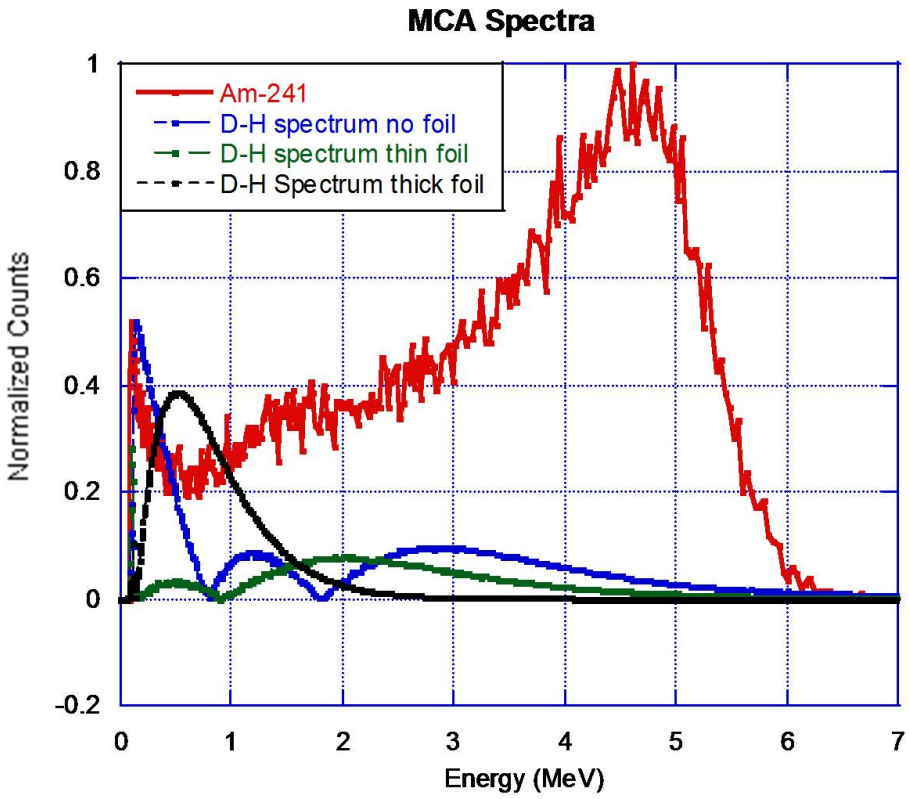

Figure 4.13: A plot of the spectrum collected on the multi-channel analyzer from the charged particle detector.

can be detected. However, the detector set-up needs to be optimized for He-3 detection, which means that no aluminum foil should be used, and a more rugged detector with a thin (< 1 μm) barrier layer should be used. A better way to fix the problem would be to use a positively biased source and grounded target. This way, the source body and the target/shroud electrode would be at the same potential, thus eliminating the high field which is present when the target is biased at negative high voltage.

4.4 Neutron yield measurements

The D-D neutron yield was measured using activation of a circular gold foil, 5 cm in diameter, located inside a polyethylene block shield 9 inches from the neutron generator. The gold foil was irradiated for 1 hour and transported to a counting facility that provided shielding from background gamma rays. Here, the generator was operated in sealed mode operation by closing the valve that connects the neutron generator to the vacuum chamber and the gas inlet needle valve was closed off.

Measurements of the activation determined a neutron yield of 2 x 10^5 n/s for an RF power of 150 Watts, an acceleration voltage of 75 kV, a beam current of $\sim$25 μA using a 2-mm long extraction channel, and an acceleration column pressure of 4.5 mTorr with air cooling on the target. The system was calibrated using several other neutron sources with known yields that were absolutely calibrated at the Nuclear Sciences Division at LBNL. The decay rate of the activated foil has also been taken into account for delayed detection after the end of the exposure. Also taken into account was the solid angle of the irradiated foil. Scattering through target generator materials was negligible, with the foil placed above the neutron generator and no polyethylene shielding in the path of the neutrons. The neutron generator was also run with water cooling on the target at the same conditions, and the neutron yield from foil activation was measured to be 3 x 10^5 n/s. As mentioned in chapter 3, since the beam spot size is small, the local power density at the beam spot will be high. If the temperature is above 210 degrees Celsius, the implanted deuterium will diffuse out of the surface, thus lowering the neutron yield. The neutron yield was lower when air cooling was used, but due to the thick titanium layer and the low thermal conductivity of titanium, the gain in neutron yield from using water cooling is not significant. The predicted D-D neutron yield at 75 kV was 9 x10^5 using Eqn. 4.4

$$Y = \int_0^E N\sigma(E)\frac{I}{q}\left(\frac{dE(E)}{dx}\right)^{-1} dE \tag{4.4}$$

Where Y is the neutron yield in n/s, N is the number of target nuclei per cm^3, σ(E) the D-D fusion cross section dependent on the incident deuterium ion energy, I is the ion current, q the charge of an electron, $\frac{dE(E)}{dx}$ the stopping power of deuterium in titanium, and E is the energy of the ions [55]. The assumption made here is the ions are all monatomic. With

a table of the cross section and stopping power, the integral can be evaluated by summing up at each energy up to the beam energy. A plot of the cross sections for D-T and D-D reactions can be see in Fig. 4.14 [58].

The total neutron yield as a function of beam energy is shown in Fig. 4.15, for a 25 μA beam and a fully loaded target of 1.35 x 10^{24} atoms/cm^3. The discrepancy in the neutron yield is from the assumption that the ion beam is 100% monatomic and the target is fully loaded, which is not the case for a self-loading target.

4.4.1 Shielding for the API neutron generator

Due to the radiation produced by the API neutron generator, polyethylene and lead shielding were used to stop the neutrons and x-rays produced by the device. Besides the shielding, a He-3 neutron detector and a NaI gamma detector were placed around the shielding to allow for constant radiation dose monitoring through the LBNL telemetry system. The shielding was comprised of 1/4 inch lead shielding and six 1-inch thick polyethylene blocks on all sides except for the top. Fig. 4.16 shows the engineering drawing of the shielding. The shielding was sufficiently thick enough that no noticeable neutron or x-ray dose was observed outside of the high voltage cage during neutron experiments.

4.4.2 Target Loading with Deuterium

The load time of the titanium target was also investigated. Since the target is not pre-loaded, it takes time for the deuterium to load up in the target and the neutron yield to reach its plateau. A previously built neutron generator with a high current ion source was used to test how long it would take for the neutron yield to reach a maximum and remain steady. The reason a different neutron generator was used was that the current prototype API neutron generator does not put out a large enough neutron yield which can be observed on the telemetry system, which was used to monitor the neutron dose in real time. When the observed neutron dose begins to stop increasing with time and remains constant, then the target can be said to be fully loaded. The ion source of the neutron generator that was used for target loading operated with a beam current of 1 mA at 90 kV. Both titanium and molybdenum were used as the target material. Molybdenum was chosen because it has a much higher heat conductivity and thus would not have a problem with deuterium diffusing out of the target. However, it cannot form a hydride with deuterium as easily, thus lowering the total deuterium density in the target. The neutron dose observed for both the titanium and molybdenum target reached an equilibrium level after about 3 hours of operation. The observed neutron dose with the molybdenum target was about 40% of that of the titanium target. After the target had been loaded, subsequent experiments performed 24 hours later required only a loading time of 1 hour to load the target, and only 15 minutes to reach a

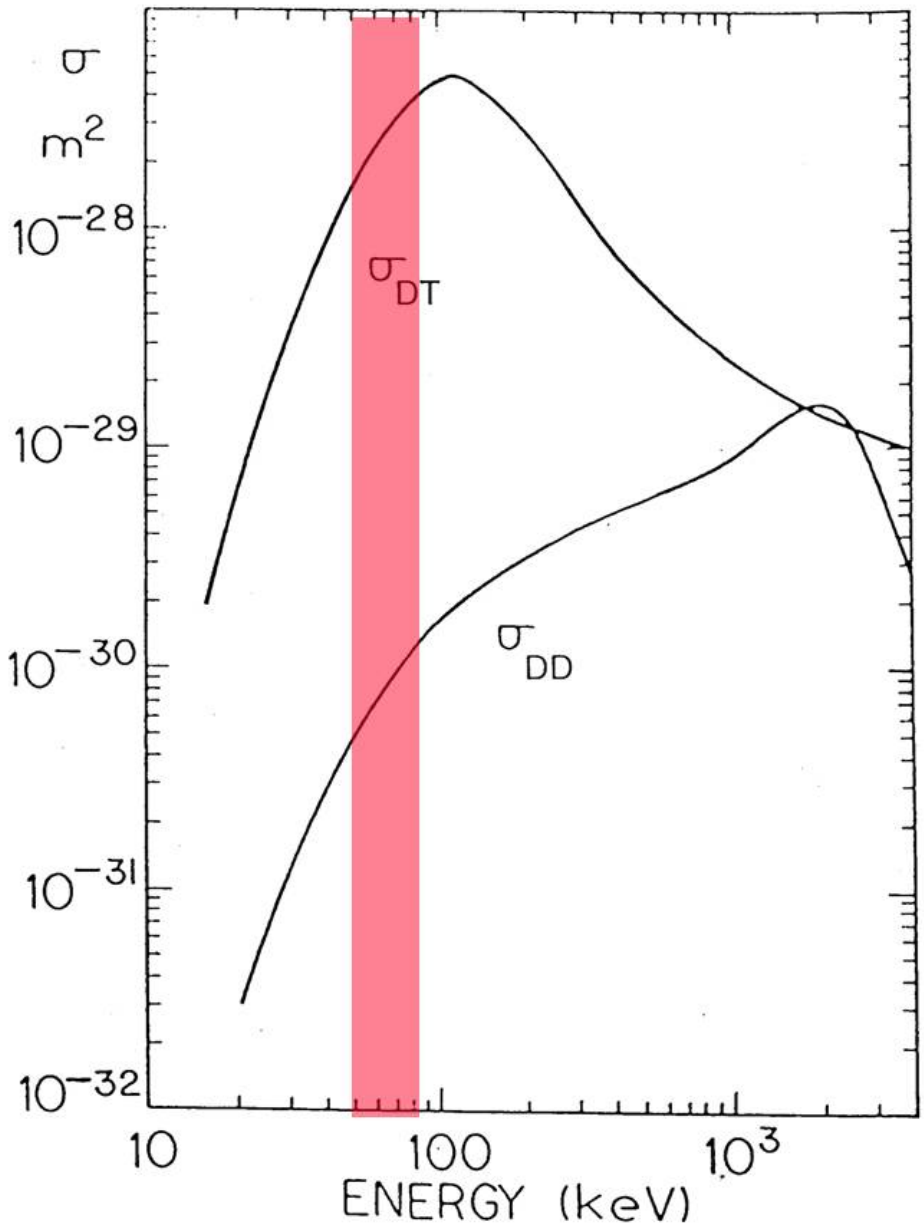

Figure 4.14: The fusion cross sections of D-T, and D-D reactions as a function of energy on a log-log plot. The energies of interest is highlighted on the plot [58].

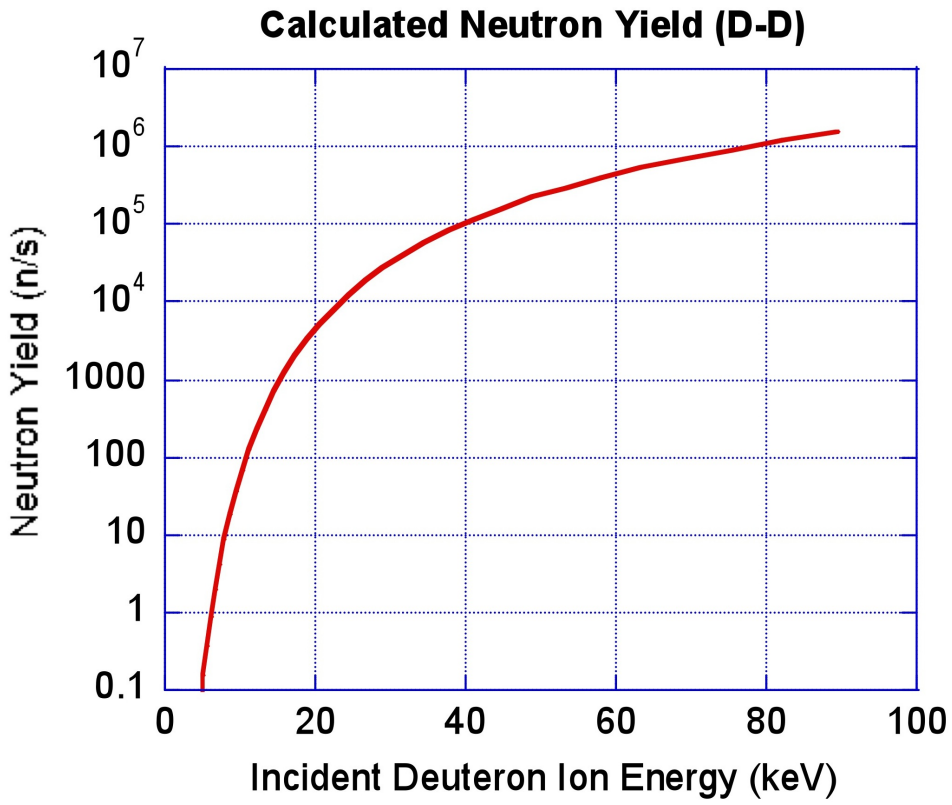

Figure 4.15: The predicted D-D neutron yield curve as a function of ion energy for an ion current of 25 μA, this also assumes that the target is loaded at a hydrogen to titanium ratio of 2:1 and that all of the ions are atomic.

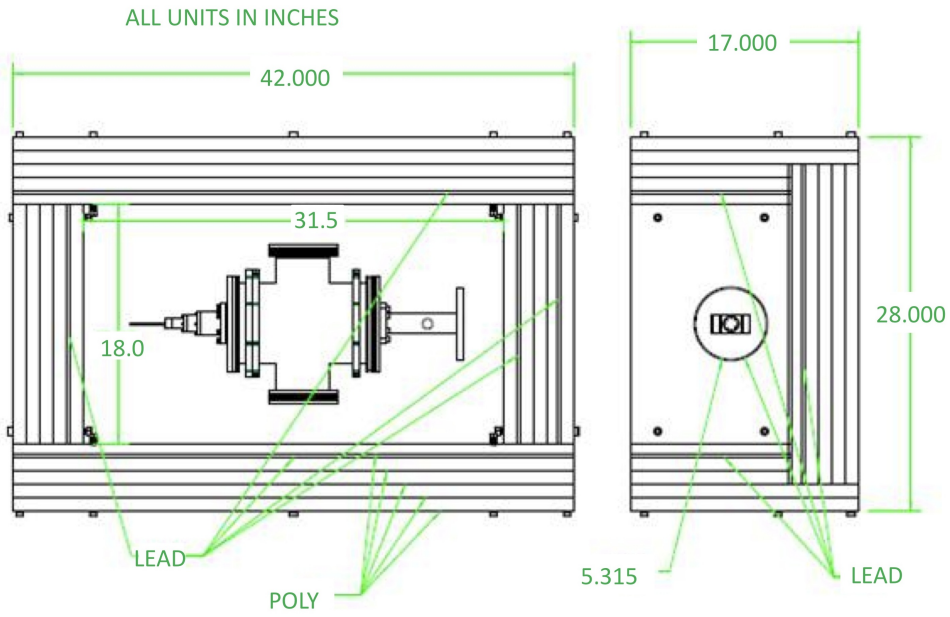

Figure 4.16: The drawing of the neutron and x-ray shielding for the API neutron generator. A gamma detector was mounted outside the high voltage cage to monitor the x-ray dose and a He-3 neutron detector embedded in a sphere of polyethylene was used to monitor the neutron dose [59].

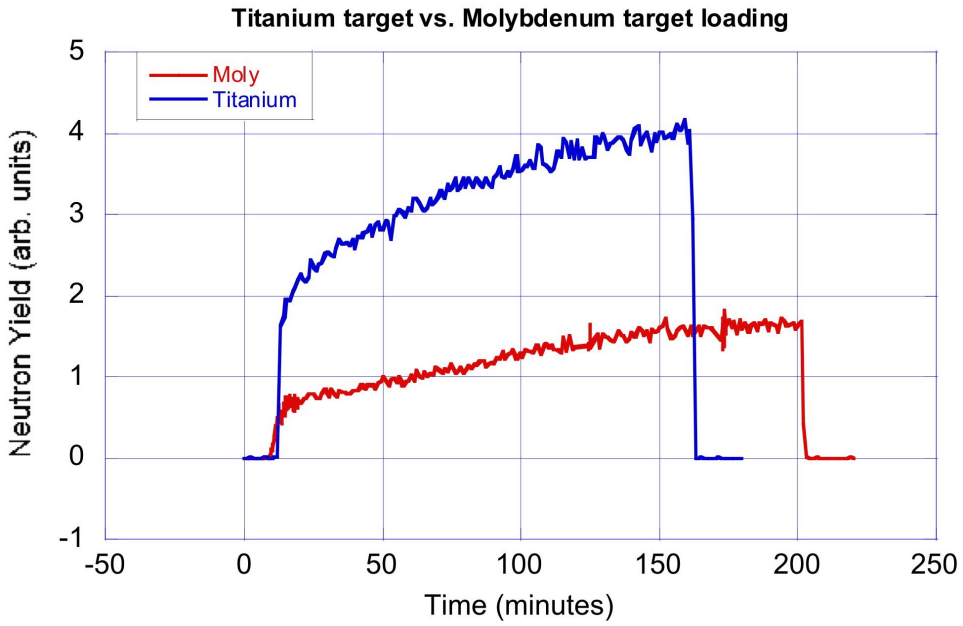

Figure 4.17: A comparison of the relative neutron yield between titanium and molybdenum targets. It takes about 3 to 4 hours to fully load the target, and the molybdenum target can reach about 45% of the neutron yield of the titanium target.

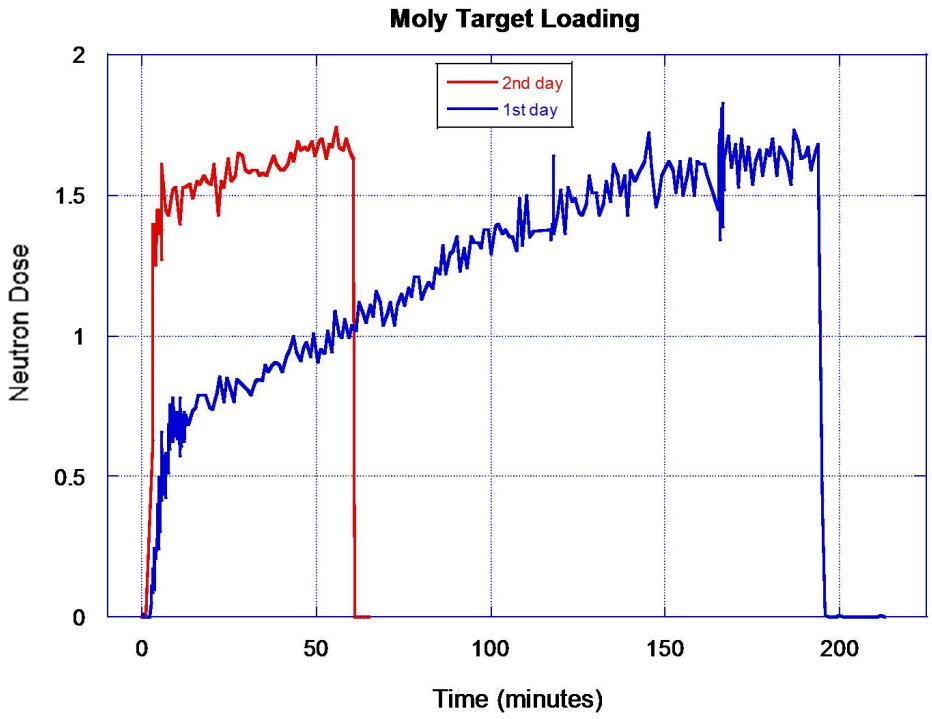

Figure 4.18: The target loading times for molybdenum after waiting 24 hours after the targets has been loaded. It takes about 15 minutes to reach 85% of the neutron yield of the previous day, and about an hour to be fully loaded. The same trend was also observed for titanium.

Theoretical D-D Neutron Yield for the API Neutron Generator at 75 kV, 0.02 mA of beam current, air cooled	**1 x 10^6 n/s**
Measured D-D Neutron Yield for the API Neutron Generator at 75 kV, 0.02 mA of beam current, air cooled	**2 x 10^5 n/s**
Theoretical D-T Neutron Yield for the API Neutron Generator at 80 kV, 0.02 mA of beam current, air cooled	**2 x 10^8 n/s**
*Predicted D-T Neutron Yield for the API Neutron Generator at 80 kV, 0.02 mA of beam current, air cooled	**8 x 10^7 n/s**

***Predicted yield is calculated by taking the measured D-D neutron yield at 75 kV, and multiplied by the quotient of the D-T divided by the D-D fusion cross section at 75 kV, then multiplied by the quotient of the D-T fusion cross section at 80 kV divided by the cross section at 75 kV.**

Figure 4.19: The theoretical and measured neutron yield of the API neutron generator for D-D operation and the theoretical and predicted neutron yield of the API neutron generator for D-T operation.

load of 85% of the maximum. Figs. 4.17 and 4.18 show the initial and subsequent loading times for the titanium and molybdenum targets.

4.5 Conclusion

A prototype neutron generator has been built and tested under sealed conditions, using deuterium gas. The ion beam spot has been measured to be less than 1-mm with a 2-mm thick aperture and an ion current of 25 μA. The neutron yield was measured by using gold foil activation analysis. It is measured to be 2 x 10^5 n/s for an RF power of 150 W and $\sim$25 μA of beam current at 75 kV using air cooling on the target. A chart showing the neutron yields (both measured and theoretical D-D neutron yields and the theoretical and predicted D-T neutron yields for the API neutron generator) is shown in Fig. 4.19.

Scaling the voltage up to 80 kV and using D-T operation should meet the design requirements of 5 x 10^7 n/s set for the API neutron generator. It was discovered that under sealed conditions, a negatively biased target routinely sparks to the scintillator at pressures over 5 mTorr. A silicon implanted charged particle detector was used to look at the associated particles from the D-D nuclear reaction. Due to the presence of the high electric field and electrons in the acceleration column, the noise level in the detector was very high. Different thicknesses of aluminum foils were used to reduce the noise from electrons, and the associated particles were observed.

Chapter 5

Conclusion

5.1 Conclusions and Suggestions for Future Work

The threat of suicide and car bombings in war-torn countries will continue to be a major issue. As of November 26, 2009, there have been over 1700 suicide bombings in Iraq since U.S. troops entered Iraq in 2003. This does not include bombings which have occurred in Afghanistan, India, Bali, and other countries around the world. The use of devices and systems which can detect explosives such as a car bomb and provide accurate imaging and location of the hidden explosives will be a great asset in saving lives of innocent civilians and the men and women of the American military. Active neutron interrogation systems like API were developed to meet the needs in explosive and land mine detection. A prototype neutron generator was developed which utilized an RF-driven ion source for API. The ion source was an improvement over the Penning ion source in terms of atomic ion fraction, beam spot size, and life-time.

The development of ion sources is crucial for improving neutron generator technology. The challenges for neutron generators used for API are that they must have a small beam spot $\leq$ 1-mm in diameter, be able to operate continuously without any water cooling or pumping, and maintain a minimum D-T neutron yield of 10^7 n/s. The prototype neutron generator was able to meet these demands by using a RF-driven ion source built using a quartz chamber and external planar antenna with side multi-cusp magnets. The quartz source helped to lower the recombination rate of deuterium or tritium atoms to their molecules on the surface, and operating the RF plasma in the inductively coupled mode allowed the atomic ion fraction to exceed 80% with only 100 watts of input RF power at 13.56 MHz. The current density in the source was 3 mA/cm^2. The operating pressure at 100 watts was 8.5 mTorr, and can be decreased to 5 mTorr by increasing the RF power to 150 W.

The beam spot requirement was met by using an extraction aperture with a 1-mm diameter, 1-mm deep ion extraction channel. The channel helps to reduce the beam spread and reduce the beam current on target. The beam current measured with 150 W of input RF

power and 5 mTorr of deuterium gas at 75 keV was 40 μA. The beam spot was measured both optically and physically via sputtering and profiling to have a Gaussian profile with a FWHM of 1-mm. The beam spot can be further reduced by using a longer extraction channel, but the ion source will need to run at a higher power to make up for the loss in beam current.

The neutron generator was sealed from the pumping system with a hand valve, and the pressure in the acceleration column and the ion source can be brought to an equilibrium. Sealed testing of the prototype neutron generator revealed a flaw in the design. Due to the highly negative biased target and electron suppression electrode, there is a high electric field between the target and the alpha detector. Plastic scintillators which were coated with a thin metal film were used in the prototype neutron generator, but were damaged by electrical breakdowns during sealed-tube operation of the neutron generator. Because of this, the neutron generator had to be operated at around 175 W so that the pressure inside the source and target chamber can be decreased to below 5 mTorr. A silicon implanted detector was used to look at the charged particles produced from the D-D reaction, and the resulting spectra showed presence of 3 MeV protons with aluminum foil covering the detector to reduce the noise from electrons. The neutron yield was measured using gold foil activation inside a polyethylene cylinder and the neutron yield measured was 2 x 10^5 n/s using air cooling on the titanium target. The loading time for a new titanium and molybdenum target is about 3 hours for the neutron yield to reach its maximum. After the target has been loaded, subsequent loading times of only 15 minutes are required to reach 85% of the maximum neutron yield.

Improvements in the neutron generator can be made by changing the biasing on the neutron generator electrodes. If the plasma electrode was biased at positive high voltage, and the target was biased at ground potential, there would not be a high electric field in the acceleration column. Thus, the electron noise in the detector would be eliminated. In the case of a D-T generator, the charged-particle detector cannot have a metal layer thick enough to stop electrons as it would also stop the 3.5 MeV alpha particles. Another area of improvement is the operation and ignition pressure. In order to operate the system in a total sealed environment, the gas must be stored in metal getters, which release and absorb gas when they are heated and cooled. The ignition pressure for 13.56 MHz is over 50 mTorr for deuterium, which is very high. If the RF generator and matching box were designed for a range of frequencies, the plasma could be started at pressures as low as 8 mTorr at 27.12 MHz, and the frequency can then be dropped to put the plasma in an inductively coupled mode. Being able to vary the frequency would also allow the ion source to operate at higher frequencies and lower pressures without the plasma going to capacitively coupled mode. Finally, using a scandium target may increase the neutron yield as it has a better hydrogen retention rate at higher temperatures than titanium, and it does not get brittle from ion bombardment like molybdenum.

Bibliography

[1] Wright, Robin "Since 2001, a Dramatic Increase in Suicide Bombings," Washington Post, April 18, 2008.

[2] J.P. Hurley, R.P. Keegan, J.R. Tinsley, and R. Trainham, Proc. SPIE 7324, 73240X, 2009.

[3] T.B. Cochran and M.G. McKinzie, "Detecting Nuclear Smuggling," Scientific America, pp. 98-104, 2008.

[4] VACIS Systems Nonintrusive Inspection of Cargo and Vehicles, An Information Guide for Customers, June 2005.

[5] A.K. Novakoff, "FAA bulk technology overview for explosives detection," Applications of Signal and Image Processing in Explosives Detection Systems, Boston, MA, USA, pp. 2-12, 1993.

[6] A. Buffler, "Contraband detection with fast neutrons, Radiation Physics and Chemistry," **71** pp. 853-861, 2004.

[7] T. Gozani, "Novel applications of fast neutron interrogation methods," Nucl. Instrum. Methods A, **353**, pp. 635640, 1994.

[8] D.R. Brown, A. Coates, S.N. Kuo, R. Loveman, E. Pentaleri, R.C. Rynes, "Cargo inspection based on pulsed fast neutron analysis," Proc. Int. Soc. Opt. Eng. **2396**, pp. 8594, 1997.

[9] J.C. Overley, "Element-sensitive computed tomographywith fast neutrons," Nucl. Instrum. Methods B, 24/25, pp. 10581062, 1987.

[10] A. Beyerle, J.P. Hurley, L. Tunnell, "Design of an associated particle imaging system," Nucl. Instr. and Meth. A, **299**, pp. 458, 1990.

[11] A. Beyerle, R. Durkee, G. Headley, J.P. Hurley, L. Tunnell, "Associated particle imaging," Nuclear Science Symposium and Medical Imaging Conference, 1991., Conference Record of the 1991 IEEE , **2**, pp. 1298-1304, 2-9 Nov 1991.

[12] L.E. Ussery and C.L. Hollas, "Design and Development of the Associated-Particle Three-Dimensional Imaging Technique," Rep. LA-12847-MS (UC-706 and UC-700), Los Alamos National Laboratory, Los Alamos, NM.

[13] D.L. Chichester, M. Lemchak, J.D. Simpson, "The API 120: A portable neutron generator for the associated particle technique," Nuclear Instruments and Methods in Physics Research Section B: Beam Interactions with Materials and Atoms, **241**, Issues 1-4, pp. 753-758, Dec. 2005.

[14] J.C. Cooper, D.S. Koltick, J.T. Mihalczo, J.S. Neal, "Evaluation of ZnO(Ga) coatings as alpha particle transducers within a neutron generator," Nuclear Instruments and Methods in Physics Research Section A: Accelerators, Spectrometers, Detectors and Associated Equipment, **505**, Issues 1-2, Proceedings of the tenth Symposium on Radiation Measurements and Applications, pp. 498-501, 2003.

[15] J.P. Hurley, "Personal Communication," 2009.

[16] J. Reijonen, N. Andresen, F. Gicquel, et al., "Development of advanced neutron/gamma generators for imaging and active interrogation applications," Optics and Photonics in Global Homeland Security III, Orlando, FL, USA, 2007.

[17] J. Reijonen, F. Gicquel, S.K. Hahto, M. King, T.P. Lou, K.N. Leung, "D-D neutron generator development at LBNL," Appl. Radiat. Isotopes **63**, Issues 5-6, 8th International Conference on Applications of Nuclear Techniques, pp. 757-763, 2005.

[18] J.M. Verbeke, et al. "Neutron tube design study for boron neutron capture therapy application," Lawrence Berkeley National Laboratory, 1999.

[19] F. Gicquel, "Engineering Drawings of a Compact Neutron Generator," Lawrence Berkeley National Laboratory, 2003.

[20] J.T. Tate and P.T. Smith, "The Efficiencies of Ionization and Ionization Potentials of Various Gases Under Electron Impact," Physical Review, **39**, pp. 270, 1932.

[21] Encyclopedia Britannica, "Argon: first ionization energies," 2007.

[22] Y.K. Kim and M.E. Rudd, Phys. Rev. A **50**, pp. 3954, 1994.

[23] I.G. Brown, The Physics and Technology of Ion Sources: Wiley-VCH, 2004.

[24] T. Schenkel et al., "Plasma ignition schemes for the spallation neutron source radio-frequency driven H- source," Review of Scientific Instruments, **73**, pp. 1017-1019, Feb. 2002.

[25] M.A. Lieberman and A.J. Lichtenberg, Principles of Plasma Discharges and Materials Processing 2nd Ed. Wiley, New York, 2005.

[26] Thermo Scientific, Neutron Generator Overview, Thermo Fisher Scientific Inc., www.thermo.com, 2009.

[27] M.J. King, G.T. Miller, J. Reijonen, Q. Ji, N. Andresen, F. Gicquel, T. Kalvas, K.N. Leung, J.W. Kwan, "Initial Evaluation of a Pulsed White Spectrum Neutron Generator for Explosive Detection," IEEE Transactions on Nuclear Science, **56**,No. 3, pp. 1283 1287, June 2009.

[28] J. Reijonen et al. "First PGAA and NAA experimental results from a compact high intensity D-D neutron generator," Nuclear Instruments and Methods in Physics Research Section A: Accelerators, Spectrometers, Detectors and Associated Equipment, **522**, Issue 3, pp. 598-602, 2004.

[29] B.A. Ludewigt et al., Nucl. Instru. and Meth. in Phys. Res. B, **261**, No. 1-2, pp. 830-834, Apr. 2007.

[30] D.L. Chichester, J.D. Simpson, M. Lemchak, "Advanced compact accelerator neutron generator technology for active neutron interrogation field work," Journal of Radioanalytical and Nuclear Chemistry, **271**, No. 3, pp. 629-637, 2007.

[31] Y. Wu, J.P. Hurley, Q. Ji, J. Kwan, K.N. Leung, "Development of a RF-Driven Neutron Generator for Associated Particle Imaging," IEEE Transactions on Nuclear Science, Vol. **56**, No. 3, pp. 1306-1311, June 2009.

[32] J. Reijonen, K.N. Leung, G. Jones, "RF ion source development for neutron generation and for material modification," Rev. Sci. Instrum. **73**, pp. 934, 2002.

[33] K.N. Leung, "Radio frequency driven multicusp sources," Rev. Sci. Instrum. **69**, pp. 998, 1998.

[34] J. Reijonen, T.P. Lou, B. Tolmachoff, and K.N. Leung, Proc. SPIE Int. Soc. Opt. Eng. 4510, 80, 2001.

[35] J.M. Verbeke, K.N. Leung, J. Vujic, "Development of a sealed-accelerator-tube neutron generator," Appl. Radiat. Isot. **53**, pp. 801-809, 2000.

[36] K.T.A.L. Burm, "Calculation of the Townsend Discharge Coefficients and the Paschen Curve Coefficients," Contrib. Plasma Phys. **47**, No. 3, pp. 177-182, 2007.

[37] J. Hopwood et al., J. Vac. Sci. Technol. **A11**, pp. 152, 1993.

[38] U. Kortshagen, N.D. Gibson, J.E. Lawler, "On the E-H mode transition in RF inductive discharges," J. Phys. D: Appl. Phys. **29**, pp. 1224-1236, 1996.

[39] S.K. Hahto, S.T. Hahto, Q. Ji, K.N. Leung, S. Wilde, E.L. Foley, L.R. Grisham, and F.M. Levinton, Rev. Sci. Instrum. **75**, 355, 2004).

[40] K.N. Leung, T.K. Samec, and A. Lamm, Phys. Lett. **51A**, 490, 1975.

[41] K.N. Leung, G.R. Taylor, J.M. Barrick, S.L. Paul, and R.E. Kribel Phys. Lett. **57A**, 145, 1976.

[42] T. Takagi, I. Yamada, J. Ishikawa, F. Sano, and N. Kusano, Proceedings of the Second Symposium on Ion Sources and Formation of Ion Beams, Berkeley, CA, pp. III.2.1-III.2.6, 22 October 1974.

[43] M.M. Turner and M.A. Lieberman, "Hysteresis and the E-H transition in radiofrequency inductive discharge," Plasma Sources Sci. Technol., **8**, pp. 312-324, 1999.

[44] C.F. Chan, C.F. Burnell, W.S. Cooper, "Model of positive ion sources for neutral beam injection," J. Appl. Phys,. **54**, pp. 6119, 1983.

[45] J. Vainionpaa, T. Kalvas, S.K. Hahto, J. Reijonen, "Experiments with planar inductive ion source meant for creation of H+ beams," Rev. Sci. Instrum., **78**, 063583, 2007.

[46] Y. Wu, J.P. Hurley, Q. Ji, J. Kwan, K.N. Leung, "Characteristics of a RF-Driven Ion Source for a Neutron Generator Used for Associated Particle Imaging," AIP Conf. Proc., **1099**, pp. 614, 2009.

[47] O. Fukumasa, J. Phys. D: Appl. Phys. **18**, pp. 2433, 1985.

[48] I. Langmuir and K.T. Compton, "Electrical discharges in gases Part II. Fundamental phenomena in electrical discharges," Reviews of Modern Physics, **3**, pp. 191-257, Apr 1931.

[49] M. Reiser, Theory and Design of Charged Particle Beams, Wiley, 2008.

[50] R. Becker and W.B. Herrmannsfeldt, "IGUN - A program for the simulation of positive ion extraction including magnetic fields," Proceedings of the fourth International Conference on Ion Sources, Bensheim (Germany), pp.2756-2758, 1992.

[51] Q. Ji et al., J. Vac. Sci. Technol. B, **20**, 6, pp. 2717, 2002.

[52] Y.Wu, J.P. Hurley, Q. Ji, J. Kwan, K.N. Leung, Rev. Sci. Instrum., "Sealed operation of a rf driven ion source for a compact neutron generator to be used for associated particle imaging," Proceedings of the International Conference on Ion Sources (ICIS 09), 2010, To be published.

[53] K.N. Leung, Rev. Sci. Instrum. **71**, pp. 1064, 2000.

[54] F. Gicquel, "Engineering Drawings of a Compact Neutron Generator for Associated Particle Imaging," Lawrence Berkeley National Laboratory, 2005.

[55] J. Csikai, Handbook of Fast Neutron Generators, Vol. I, 1987.

[56] X. Jiang, Q. Ji, A. Chang, and K.N. Leung, Rev. Sci. Instrum. **74**, pp. 2288, 2003.

[57] X. Jiang, Y. Chen, L. Ji, Q. Ji, and K.N. Leung, Rev. Sci. Instrum. **76**, pp. 103302, 2005.

[58] T.J. Dolan, Fusion Research - Principles, Experiments and Technology: Pergamon Press, 1962.

[59] M. Dickinson, "Engineering Drawings of the Lead and Poly Shielding in Test Stand 5," Lawrence Berkeley National Laboratory, 2009.